

UNIVERSITY of CALIFORNIA  
Santa Barbara

**Deformation and Localization in Earthquake Ruptures  
and Stick-Slip Instabilities**

A dissertation submitted in partial satisfaction of the  
requirements for the degree of

Doctor of Philosophy

in

Physics

by

Eric G. Daub

Committee in charge:

Professor Jean Carlson, Chair  
Professor Jacob Israelachvili  
Professor James S. Langer  
Professor Ralph J. Archuleta

September 2009

**Deformation and Localization in Earthquake Ruptures  
and Stick-Slip Instabilities**

Copyright 2009

by

Eric G. Daub

## Acknowledgements

Thank you to my committee members, whose diverse areas of expertise have given me a great perspective on the various disciplines that play a part in my research. Jim Langer made sure that I didn't lose my identity as a physicist, Jacob Israelachvili gave me hope that experimentalists could measure what my models predict, and I value Ralph Archuleta's perspective on what we know and don't know about earthquakes. Other valuable scientific discussions were provided by Chen Ji, Gregor Hillers, Daniel Lavalley, Shuo Ma, Susana Custodio, and Dan Lowrey. Thanks also to Eric Dunham for providing the dynamic rupture code that I used in my simulations.

My family and friends have also been great assets. My parents have provided love and support throughout the years. After five years of living on my own, I realize that they made me into the "responsible adult" (their words) that I am now. My dad continues to provide a complementary scientific perspective to my own as a chemist, and I'm sure my mom doesn't realize how much the summers I spent working in her office helped me decide to be a scientist. I'd also like to thank Jimmy O'Dea for our weekly runs, which help clear my head and take my mind off of science for a while, and Aidan Finley for the absurd number of emails that he sends me.

To my fellow graduate students past and present, thanks to all of you for scientific and social support. Thanks to all the GS270 folks, and the students in Jean's group. Jan Schmedes always had good questions and ideas regarding earthquake rupture. Morgan Page provided a valued perspective on earthquakes due to the wide range of problems that she has studied. Sean Stromberg and Ann Hermunstad have been top notch office mates, always willing to share a humorous video or tell a good story, in addition to providing good suggestions on points scientific. And thank you to Lisa Manning, who has been a wonderful collaborator whenever we have been able to find time to stop talking about sports. Lisa constantly questioned me, and her insistence that we look to at small scale physics to motivate our models was a valuable complement to my insistence that our models capture the correct large scale dynamics.

And most of all, this dissertation never could have happened without my advisor Jean Carlson. Jean let me work independently, yet provided the perfect level of guidance and made many suggestions that honed my ideas and simulations. She has been a model for how to do interdisciplinary science, and her infectious enthusiasm has made my time in Santa Barbara truly rewarding.

# Curriculum Vitæ

## Eric G. Daub

### Education

- 2009            PhD in Physics, University of California, Santa Barbara  
2004            BA in Physics, Williams College

### Publications

- “Rate-dependent shear bands in a shear-transformation-zone model of amorphous solids,” M. L. Manning, E. G. Daub, J. S. Langer, and J. M. Carlson, *Phys. Rev. E*, 2009.
- “A constitutive model for fault gouge deformation in dynamic rupture simulations,” E. G. Daub and J. M. Carlson, *J. Geophys. Res.*, 2008.
- “Shear strain localization in elastodynamic rupture simulations,” E. G. Daub, M. L. Manning, and J. M. Carlson, *Geophys. Res. Lett.*, 2008.
- “Quantifying Optimal Accuracy of Local Primary Sequence Bioinformatics Methods,” D. P. Aalberts, E. G. Daub, and J. W. Dill, *Bioinformatics*, 2005.

### Honors and Awards

- 2009            Postdoctoral Fellowship, Los Alamos National Laboratory  
2008            Outstanding Student Presentation Award, AGU Fall Meeting  
2008            Outstanding Student Presentation Award, SSA Annual Meeting  
2006-2009     Southern California Earthquake Center Grant (PI: Jean M. Carlson)  
2006, 2007    Physics Circus Award, UCSB Physics Department  
2004            Elected to Sigma Xi, Williams College

## Abstract

### Deformation and Localization in Earthquake Ruptures and Stick-Slip Instabilities

by

Eric G. Daub

The dynamic earthquake problem spans a broad range of length scales, from microscopic grain contacts through faults that are hundreds of kilometers long. A major goal of dynamic earthquake modeling is to develop friction laws that capture the small scale physics and that can also be used to model fault scale rupture. However, friction laws used in studying earthquake rupture are often simply fits to data, and give little physical insight into the rupture process. The goal of this work is to develop a model for the deformation of amorphous materials such as granular fault gouge, and to investigate the dynamics of instabilities at larger scales. The model is based on Shear Transformation Zone (STZ) Theory, a microscopic physical model for plastic deformation in dense amorphous materials such as fault gouge, granular materials, glasses, foams, and colloids. STZ Theory captures fracture and deformation features that are observed in numerical simulations, and remains tractable for modeling friction at larger scales. STZ Theory ties fault weakening to the evolution of an effective temperature, which quantifies the configurational disorder in the gouge and serves as the dynamic state variable in STZ Theory.

STZ Theory predicts logarithmic rate dependence and that the length scale for frictional evolution increases with increasing average strain rate, which are observed in laboratory experiments. Additionally, STZ Theory captures the spontaneous formation and growth of narrow shear bands in the fault gouge. Shear bands within a layer of gouge are observed in many studies of faulting, which indicates that resolving the dynamics of shear banding is important for capturing the small scale physics during earthquake slip.

At the scale of frictional interfaces, we investigate the role of strain localization for stick-slip instabilities in an elastic block slider system. We perform a linear stability analysis to predict the critical value of the spring stiffness when steady sliding becomes unstable, and verify our results through numerical integration. We find that when a shear band forms, steady sliding becomes unstable at a larger spring stiffness.

We also investigate the implications of STZ Theory and strain localization in dynamic earthquake simulations. We compare STZ Theory without strain localization, Dieterich-Ruina (DR) friction, and linear slip-weakening (SW). The dynamic rupture governed by STZ Theory accelerates more rapidly to the limiting wave speed, exhibits a decreased peak slip rate, and transitions to supershear rupture at a lower initial shear stress than equivalent ruptures with DR or SW friction.

For dynamic ruptures where a shear band does form, strain localization alters fault behavior because localization is a mechanism for dynamic weakening. The dynamic weakening of strain localization increases the slip rate during rupture, and also increases the stress drop. We also show that strain localization occurs below seismogenic depths where constitutive properties are rate strengthening due to slip propagating down dip from the seismogenic zone. Our results indicate that the small scale physics occurring within the gouge can have a large scale impact on the dynamics of friction and the propagation of slip on earthquake faults.

# Contents

|  |            |
|--|------------|
| <b>Contents</b>  | <b>vii</b> |
| <b>1 Introduction</b>                                      | <b>1</b>   |
| 1.1 Multi-Scale Nature of the Earthquake Problem . . . . . | 2          |
| 1.2 Constitutive Laws . . . . .                            | 4          |
| 1.2.1 Static/Dynamic Friction . . . . .                    | 4          |
| 1.2.2 Slip-Weakening Friction . . . . .                    | 6          |
| 1.2.3 Velocity-Dependent Friction . . . . .                | 6          |
| 1.2.4 Dieterich-Ruina Friction . . . . .                   | 7          |
| 1.3 Plastic Deformation in Amorphous Materials . . . . .   | 10         |
| 1.4 Strain Localization . . . . .                          | 14         |
| 1.5 Dynamic Earthquake Rupture . . . . .                   | 18         |
| 1.5.1 Heterogeneities . . . . .                            | 18         |
| 1.5.2 Rupture Speed . . . . .                              | 22         |
| 1.5.3 Rupture Types . . . . .                              | 25         |
| 1.6 Dissertation Outline . . . . .                         | 26         |
| <b>2 STZ Friction Law</b>                                  | <b>28</b>  |
| 2.1 Basic Assumptions . . . . .                            | 28         |
| 2.2 STZ Equations . . . . .                                | 30         |
| 2.3 Effective Temperature Evolution . . . . .              | 32         |
| 2.4 The Free Volume Law . . . . .                          | 35         |
| 2.5 Friction Dynamics . . . . .                            | 37         |
| <b>3 Stick-Slip Instabilities</b>                          | <b>44</b>  |
| 3.1 Stick-Slip Instabilities . . . . .                     | 44         |
| 3.2 Model Equations . . . . .                              | 46         |

|          |  |            |
|----------|--|------------|
| 3.2.1    | Block Slider Equations . . . . .                                       | 46         |
| 3.2.2    | Time Scales . . . . .  | 48         |
| 3.2.3    | Non-Dimensional Equations . . . . .                                    | 49         |
| 3.2.4    | Small Scale Effects on Friction in STZ Theory . . . . .                | 50         |
| 3.3      | Stick-Slip Dynamics . . . . .  | 50         |
| 3.3.1    | Analytical Results . . . . .   | 54         |
| 3.3.2    | Numerical Results . . . . .  | 60         |
| 3.4      | Discussion . . . . .   | 69         |
| <b>4</b> | <b>Comparing Friction Laws in Dynamic Rupture</b>                      | <b>72</b>  |
| 4.1      | Constitutive Laws in Dynamic Rupture . . . . .                         | 72         |
| 4.2      | Comparing the DR and FV Models . . . . .                               | 74         |
| 4.3      | Dynamic Ruptures . . . . .   | 79         |
| 4.4      | Rapid Weakening . . . . .  | 89         |
| 4.5      | Discussion . . . . .   | 99         |
| <b>5</b> | <b>Strain Localization in Dynamic Rupture</b>                          | <b>102</b> |
| 5.1      | Earthquake Rupture and Strain Localization . . . . .                   | 102        |
| 5.2      | Modeling Dynamic Ruptures with<br>Localization . . . . .               | 103        |
| 5.3      | Comparing Localized and Homogeneous<br>Ruptures . . . . .              | 108        |
| 5.4      | Dynamics of Localization . . . . .                                     | 110        |
| 5.5      | Fault Scale Rupture Propagation . . . . .                              | 114        |
| 5.6      | Discussion . . . . .   | 118        |
| <b>6</b> | <b>Localization in Rate Strengthening Materials</b>                    | <b>123</b> |
| 6.1      | Rate Strengthening Friction . . . . .                                  | 123        |
| 6.2      | Deformation of Glassy Materials . . . . .                              | 124        |
| 6.3      | Localization in Coseismic Slip Below the<br>Seismogenic Zone . . . . . | 132        |
| 6.4      | Discussion . . . . .   | 144        |
| <b>7</b> | <b>Conclusions</b>   | <b>146</b> |
| 7.1      | Synopsis . . . . .   | 146        |
| 7.2      | Future Directions . . . . .  | 148        |
|          | <b>Bibliography</b>  | <b>150</b> |

# Chapter 1

## Introduction

Scientists do not have a complete understanding of the physics governing earthquake rupture. Earthquakes occur deep in the earth's crust and cannot be observed directly, and seismologists can only study the seismic waves that reach the surface. Additionally, earthquakes occur at extreme physical conditions, including high pressures and temperatures, with high pore fluid pressures, and large amounts of slip and high slip rates. The physical conditions occurring at the earthquake source are therefore difficult to replicate in the laboratory. All current experimental data for earthquake slip compromises on at least one of aspect of the physics of the source.

However, even if all of the physics of the earthquake problem were completely understood, scientists still face the problem that earthquake faults are extremely complex, and involve a huge range of length and time scales. This ranges from microscopic contacts between grains up to networks of faults that are hundreds of kilometers long. The challenge in modeling earthquake rupture is to determine the essential physics at a given scale, and devise a method to efficiently propagate the information to larger scales. Time scales in the earthquake problem range from long periods of slow loading on faults during the many years of the interseismic period to rapid slip occurring over seconds during an earthquake. Earthquake source models must account for processes occurring over many different time scales during the seismic cycle.

Because there is uncertainty regarding the physics at each scale, it is difficult to determine the expected ground motion and hazard in future earthquakes. Physics-based models of the earthquake source are important because hazard estimates are based on limited historical data, which do not represent the full range of possible earthquakes. Models that are based on small-scale physics can bound uncertainties at the largest scales, and improve our estimates of hazard.

In this dissertation, we tackle the multi-scale earthquake problem by incorporating small scale physics into fault scale rupture models. Our goal is to use constraints on the small scale physics to address the range of behavior at the fault scale. This is a challenging problem that draws upon many scientific disciplines, including physics, geology, materials science, and engineering. We combine techniques and observations from these disciplines to create a dynamic rupture model that resolves the physics at the grain scale yet is tractable for investigating earthquake slip at the fault scale.

## 1.1 Multi-Scale Nature of the Earthquake Problem

Earthquakes occur due to an instability in the deformation of rocks in the earth's crust. A basic illustration of an earthquake fault is shown in Figure 1.1. The two sides of the fault are driven in opposite directions, resulting in a strike-slip fault. Rocks deep in the earth, shown in blue in the illustration, deform like a highly viscous fluid due to large temperatures and pressures. The flow of the rocks deep in the earth cause the motion of tectonic plates in the earth's crust. The frictional properties of rocks are different at shallower depths (0-15 km), which is colored red in Figure 1.1. The rocks at these depths, also referred to as the seismogenic zone, resist plate motion, and remain locked as the fault creeps at depth at rates on the order of centimeters/year. Eventually, the force on the rocks in the seismogenic zone becomes large enough that the material fails, and the fault slips rapidly on the order of meters/second in an earthquake.

However, faults are more complex than simply a planar surface where rocks slide past each other. The fault interface is filled with microscopic crushed pieces of rock called fault gouge, and the basic contact interactions between the particles dictate how the gouge deforms in response to large tectonic stresses. The deformation of the gouge determines the frictional properties of the interface, which controls rupture propagation along the fault that is many kilometers long. Finally, this fault is part of a network of faults that interact with each other and determine the global seismicity on earth. These scales are illustrated in Figure 1.2(a). At each progressively larger length scale, the time scales also get larger, and so both length and time can be collapsed onto a single axis that illustrates the range of scales in the problem.

Even at a given scale, seismologists do not completely understand the underlying physics because seismic slip occurs deep in the seismogenic zone. This means that the multi-scale earthquake problem has both “horizontal” and “vertical”

CHAPTER 1. INTRODUCTION

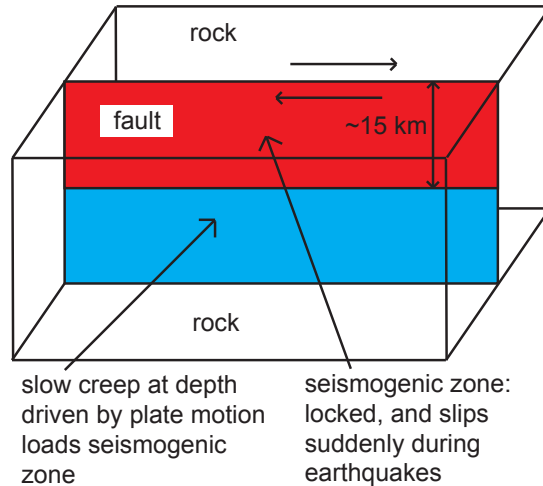


Figure 1.1: A basic illustration of an earthquake fault. At depth, high temperatures and pressures result in steady creep of fault rocks, while in the seismogenic zone above 15 km depth the rocks resist plate motion. Slip in the seismogenic zone occurs in periodic earthquakes.

challenges, illustrated in Figure 1.2(b). The “horizontal” challenge refers to the fact that seismologists do not completely understand what physical mechanisms are important at a given scale. The “vertical” challenge indicates that scientists need to develop robust connections between scales to determine how the physics at the small scales controls large scale behavior.

In this dissertation, we develop a multi-scale model for earthquake rupture that spans from grains up through faults. Our work is the first example of an earthquake model where each scale incorporates physical mechanisms, and we seek to understand the implications at the faults scale. Because the small scale physics in earthquakes is poorly constrained, we utilize a model for material deformation that is applicable to a wide range of systems and captures features from both experiments and numerical studies. We implement this grain-scale model into fault scale numerical simulations of dynamic earthquake rupture to place physical constraints on fault scale slip and ground motion.

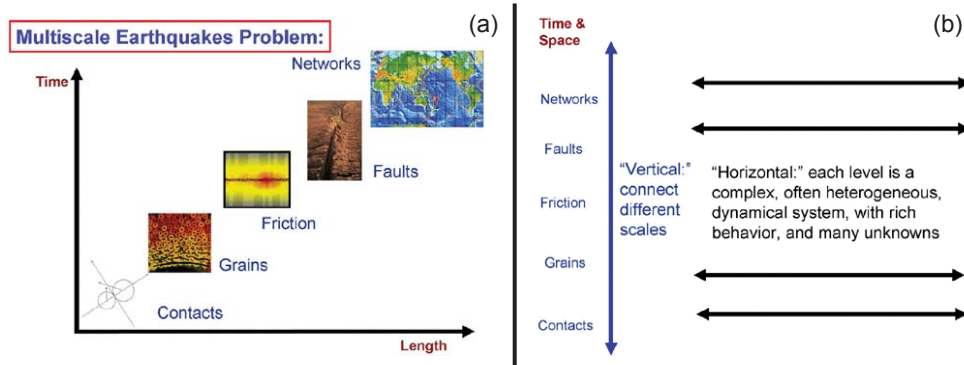


Figure 1.2: Multi-scale nature of the earthquake problem. (a) Length and time scales range from contacts up through fault networks. The important time scales also get progressively larger as the length scale increases, so these two scales can be collapsed onto a single axis. (b) The multi-scale earthquake problem is both a “horizontal” and “vertical” challenge. The “horizontal” challenge indicates that each individual scale is a complex problem that is poorly constrained, and the “vertical” challenge refers to the fact that models need to make robust connections between scales.

## 1.2 Constitutive Laws

Modeling dynamic earthquake rupture at multiple scales requires combining many ingredients representing the physics at each scale. At the fault scale, this includes the elastic response of the rock and the varying elastic properties in the velocity structure. Other effects such as plastic yielding and off-fault damage are often included such models.

The challenge is to account for small scale physical processes, while maintaining resolution at the fault scale. Traditionally, this is accomplished using a friction law. These relations, also known as constitutive laws, determine the shear stress on the fault, usually dependent on quantities such as the slip, slip rate, or other dynamic variables quantifying the internal state of the fault. Here, we discuss several different examples of friction laws traditionally used to study earthquakes.

### 1.2.1 Static/Dynamic Friction

The simplest example of a friction law is the static/dynamic friction law from introductory physics. The shear stress is always proportional to the normal stress, and the proportionality constant  $\mu$  (i.e. the coefficient of friction) takes on two

CHAPTER 1. INTRODUCTION

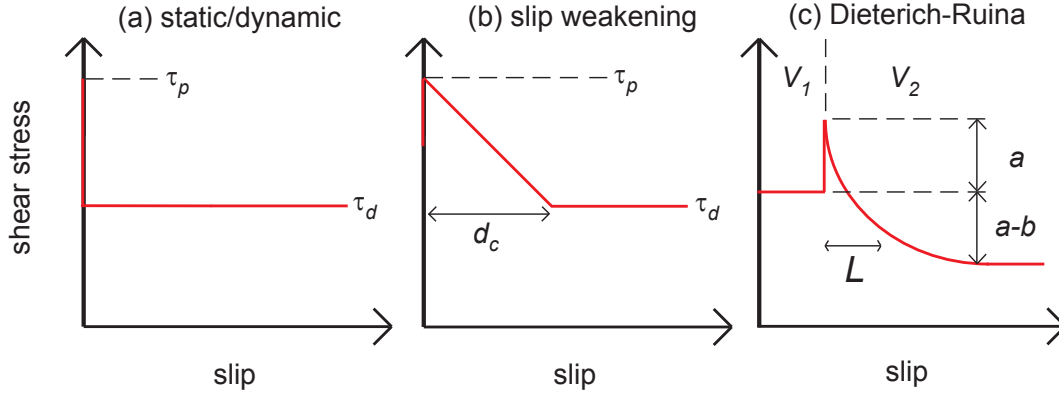


Figure 1.3: Friction laws for earthquake faults. (a) Shear stress as a function of slip for static/dynamic friction. The fault is locked until the shear stress reaches  $\tau_p$ , after which the fault slips and the stress is  $\tau_d$ . The stress changes instantaneously from the peak value to the sliding value, which is unphysical. (b) Prescribed shear stress evolution for the linear SW law. Slip initiates when the shear stress reaches the peak strength  $\tau_p$ . Over a slip distance  $d_c$ , stress weakens linearly to a constant dynamic sliding friction  $\tau_d$ . Because the sliding friction  $\tau_d$  is constant, no dynamic recovery of strength occurs for the SW law. (c) Shear stress evolution as a function of slip for the Dieterich-Ruina friction law. The evolution of shear stress during a velocity step experiment is shown. As the sliding velocity increases from  $V_1$  to  $V_2 > V_1$ , the shear stress evolves. There is an initial transient increase in the stress, quantified by the parameter  $a$ , and an evolution over the length scale  $L$  to the new value, quantified by the relative values of  $a$  and  $b$ .

different values. While the two sides of the fault are in stationary contact, the coefficient of friction is the static coefficient of friction  $\mu = \mu_s$ , and once the surfaces begin to slip the friction drops to the dynamic coefficient of friction  $\mu = \mu_d$ . This behavior is illustrated in Figure 1.2.1(a), as the shear stress is  $\tau_p = \sigma\mu_s$  prior to slip, and  $\tau_d = \sigma\mu_d$  once the fault begins to slip, where  $\sigma$  is the normal stress. However, static/dynamic friction is unphysical due to the shear stress changing discontinuously. Seismologists have proposed many modifications to static/dynamic friction to fix this problem.

## 1.2.2 Slip-Weakening Friction

Linear slip-weakening [1, 2, 3] has been used extensively to study dynamic rupture [2, 3, 4, 5, 6]. Shear stress  $\tau$  is a linearly decreasing function of slip  $u$  up to some slip-weakening distance  $d_c$ , beyond which a constant stress is prescribed:

$$\tau = \begin{cases} \tau_p - (\tau_p - \tau_d) \frac{u}{d_c}, & (u \leq d_c); \\ \tau_d, & (u > d_c). \end{cases} \quad (1.1)$$

The fault is initially locked. Shear stress increases to the peak stress  $\tau_p$  before initiating slip, and then weakens as the fault slips (Fig. 1.2.1(b)). Stress is a fixed function of slip, which sets the amount of energy lost to fracture and frictional dissipation (the area under the curve plotting shear stress as a function of slip). Because the stress  $\tau_d$  is constant, the fault cannot regain strength once it ruptures. The SW law is intentionally simple, and serves as a first approximation for how stress weakens with slip.

Other variations of purely slip-dependent laws exist, including those in work by Ohnaka [7]. Another variant of slip-weakening is what is referred to as a cohesive zone model [8]. In a cohesive zone model, the shear stress weakens to the dynamic friction coefficient over a specified length scale along the spatial extent of the fault. All of these simple models provide a fix to the transition between the constant values of static and dynamic friction. They do not incorporate healing, as once the shear stress reaches the value specified by the dynamic coefficient of friction, the fault cannot heal or restrengthen. The constitutive laws are simple and depend only on a few parameters, but they do not provide much physical insight into the small scale physics that they approximate.

## 1.2.3 Velocity-Dependent Friction

A common practice in engineering applications is to measure the slip rate dependence of friction. These measurements lead to a friction law that is dependent only on the slip rate, called the Stribeck curve [9]. Like slip weakening, this friction law is simple due to its dependence on a single quantity, but does not explain this dependence based on small scale physics. Purely velocity-dependent friction is problematic for a number of reasons. First, dynamic earthquake ruptures governed by it are numerically ill-posed. This is because for an earthquake to propagate, it must release stored elastic energy by relieving stress on the fault – that is, the shear stress before the earthquake must be larger than the shear stress after the earthquake. Since the fault is at rest before and after the earthquake, this means that the shear stress changed, but the slip velocity did not. This is

## CHAPTER 1. INTRODUCTION

not consistent with the friction law, which states that the shear stress is only a function of slip rate. Velocity-dependent friction also has the problem that in a spring slider model, the frictional interface never slides with a steady coefficient of friction if the friction decreases with increasing velocity. Rather, the block moves with successive “stick” and “slip” cycles only. Both stick-slip and steady sliding are observed in laboratory experiments for velocity weakening friction, which a velocity-dependent friction law cannot explain. To work around these problems, yet maintain the observed slip rate dependence of friction, seismologists have constructed more complicated friction laws that depend on other quantities in addition to the slip rate.

### 1.2.4 Dieterich-Ruina Friction

The Dieterich-Ruina (DR) law is a phenomenological friction law, introduced to capture experimental observations of both steady state and transient friction [10, 11]. The DR law assumes dependence on a single dynamic state variable in addition to the slip rate. This state variable captures the entire history dependence of friction through its evolution. The addition of the state variable removes the problems with velocity dependent friction discussed above. Shear stress  $\tau$  is a function of the slip velocity  $V$  and the state variable  $\theta$ . The dependence on both rate and state is logarithmic in the DR law:

$$\tau = \sigma \left[ f_0 + a \log \left( \frac{V}{V_0} \right) + b \log \left( \frac{\theta V_0}{L} \right) \right]. \quad (1.2)$$

Other parameters in the law are normal stress  $\sigma$ , constants  $a$  and  $b$  determining the rate and state dependence, length scale  $L$ , and reference friction coefficient and slip velocity,  $f_0$  and  $V_0$ , respectively.

A dynamic equation for the state variable  $\theta$  is needed to determine how the state variable evolves. A common form for the evolution for for state evolution is the ageing evolution equation [12],

$$\frac{d\theta}{dt} = 1 - \frac{\theta V}{L}. \quad (1.3)$$

The state variable  $\theta$  has dimensions of time and is often interpreted as the lifetime of surface asperity contacts, which is consistent with experiments by Dieterich and Kilgore [13] that imaged the dynamic evolution of contact area between sliding surfaces at various slip rates.

The dynamic equation for the state variable is known as the ageing law, due to the state variable evolving in time even when the surfaces are at rest. Alternative

## CHAPTER 1. INTRODUCTION

forms for the dynamic state evolution equation have been proposed based on other laboratory data. The most common alternative evolution equation is known as the slip law [12], and it has the following form:

$$\frac{d\theta}{dt} = -\frac{\theta V}{L} \log\left(\frac{\theta V}{L}\right). \quad (1.4)$$

For this version of the DR law, the state variable evolves only if the surfaces are sliding. The ageing law fits data better for rock healing, while the slip law fits data better for the frictional response of a velocity step. A composite law was proposed by Kato and Tullis [14] to combine the advantages of the ageing law for healing and the slip law for rapid changes in sliding. The composite law takes the form

$$\frac{d\theta}{dt} = \exp(-V/V_c) - \frac{\theta V}{L} \log\left(\frac{\theta V}{L}\right). \quad (1.5)$$

The composite law introduces a crossover velocity  $V_c$ . For  $V = 0$ , the composite law becomes  $d\theta/dt = 1$ , which matches the ageing law, while if  $V \gg V_c$ , the exponential term is negligible and the evolution equation matches the slip law.

The meaning of the frictional rate parameters are best understood through a velocity step experiment, illustrated in Figure 1.2.1(c). A frictional interface is sheared at a constant slip rate  $V_1$ , and reaches steady state. The slip rate is then suddenly increased to  $V_2 > V_1$ , and the friction evolves to a new value as the interface is sheared. Figure 1.2.1(c) illustrates the evolution of the shear stress with slip. There is a transient increase in the friction coefficient, with a magnitude of  $a$ . The change in the steady state friction is  $(a - b)$ . This shows that  $a$  determines the transient response to a change in slip rate, and the relative values of  $a$  and  $b$  determine how the steady-state value changes with slip rate. The length scale over which the friction evolves is determined by  $L$ .

The relative values of  $a$  and  $b$  determine the rate dependence of friction in the DR law. If  $a > b$ , then the coefficient of friction increases as the slip rate increases. This type of material is known as rate strengthening – as the driving rate increases, so does the shear stress. If  $a < b$ , then the coefficient of friction decreases as the slip rate decreases. This type of material is known as rate weakening. The rate dependence of friction is an important quantity when studying dynamic earthquake rupture, as unstable earthquake rupture only occurs with rate weakening parameters.

Laboratory studies examined the effect of temperature on the rate dependence of friction [15, 16, 17]. Data from one such study is shown in Figure 1.2.4. The friction is rate strengthening at low temperatures, then transitions to rate weakening, and at high temperatures above 300°C friction is rate strengthening again.

## CHAPTER 1. INTRODUCTION

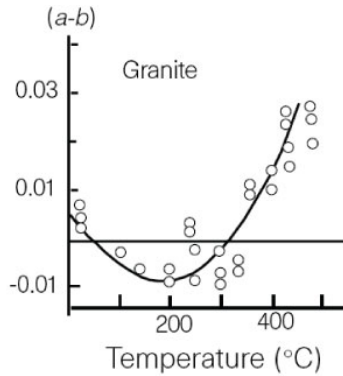


Figure 1.4: Data illustrating the effect of temperature on the frictional rate dependence. At low temperatures, friction is rate strengthening, but at temperatures corresponding to seismogenic depths, friction is rate weakening. At high temperatures, friction returns to rate strengthening, indicating that faults simply creep below the seismogenic zone. Figure taken from Scholz [18] (Reprinted with permission. Copyright 1998 by Macmillan Publishers Ltd.).

The range of temperatures that produce rate weakening correspond to about 2 km to 15 km depth on a vertical strike-slip fault. Earthquake hypocenters occur mostly between those depths, which confirms that rate weakening friction is a crucial quantity for determining if earthquakes can occur on a fault.

The logarithmic rate dependence of the DR law is problematic at  $V = 0$ . To fix this problem, several regularizations have been proposed for using the DR laws in earthquake models. These include adding a small cutoff velocity to the slip rate [19] and changing the logarithm to an inverse hyperbolic sine [20]. The need to regularize the DR laws underscores the fact that like other friction laws discussed above, the law is simply a fit to data and does not have a physical basis.

Another problem with the DR law is that the experiments it is based on differ greatly from the conditions in the earth's crust. Seismic slip rates are on the order of meters/second, while the experiments that led to the development of the DR law range from microns/second to millimeters/second [10]. Recent laboratory experiments at high slip rates show that friction at seismic slip rates is much lower than the values predicted by extrapolation of the logarithmic weakening in DR friction [21, 22]. Low friction at seismic slip rates significantly alters earthquake slip in dynamic rupture models [23]. It is therefore important to develop physical models of fault slip that account for this change in behavior at seismic slip rates.

Note that in the DR law, the state variable is governed by an ordinary dif-

ferential equation. This means that the entire history dependence of friction can be summarized by one quantity in DR friction. However, fault zones are highly complex structures, and it is likely that more degrees of freedom beyond a single dynamic quantity are necessary for determining the frictional properties of an earthquake fault. These additional degrees of freedom are needed to account for physical processes and provide an efficient way to capture the frictional properties of the fault.

### 1.3 Plastic Deformation in Amorphous Materials

Rock mechanics experiments and the phenomenological friction laws that are based on their observations are widely used in seismology. However, friction laws that are simply fits to data provide limited physical insight, and may fail when extrapolated to the extreme conditions in the earth's crust. Therefore, a better approach is to develop a friction law that is based on microscopic physics and utilizes additional degrees of freedom to incorporate observations of how amorphous materials such as fault gouge deform and fail.

Physicists, engineers, and materials scientists are interested in understanding the dynamics of amorphous materials such as granular materials, glasses, colloids, foams, emulsions, and thin films. All these materials are composed of particles (grains, atoms, bubbles, molecules) that are arranged so that their centers of mass are disordered. What is interesting about these materials is that they exhibit both solid-like and fluid-like dynamics. Under certain conditions, amorphous materials behave like solids – deformations are elastic (shear stress is proportional to the shear strain), the material exhibits a yield stress, and the material is “jammed.” Other conditions produce dynamics that are more like a fluid – the shear stress depends on the strain rate instead of the strain, and the material flows like a fluid. An example of this is sand at the beach. Sand supports the static load of a person standing on the beach, but sand also flows through the fingers of a person that scoops up a handful.

When a collection of particles is deformed, the resulting particle displacements can be approximated by two components – affine displacements, where the individual particle displacements are uniform (elastic), and non-affine displacements, where the individual particle motions are heterogeneous (plastic). The uniform displacements produce material behavior that is like an elastic solid, and this component of the motion is well-described by linear elasticity. The non-affine deformation is more complicated, and requires new models to describe the material

## CHAPTER 1. INTRODUCTION

properties.

Molecular dynamics or discrete element simulations are frequently used to study the dynamics of amorphous materials [24, 25, 26, 27, 28]. An example of a simulation of a glass is shown in Figure 1.5 [26]. The material is under tensile strain, but the deformation in the material results in shear deformation (indicated by the arrows). The dark regions show where non-affine deformation occurs in the material. The plastic deformation is localized to a narrow shear band, which is a common mechanism of failure in amorphous materials.

While these simulations do provide insight into how these materials deform, they are not efficient for studying larger scale behavior, as keeping track of the position and momentum of a large number of particles requires extensive computational resources. Instead, physicists would like to develop a continuum model to describe the deformation of amorphous materials, much like continuum mechanics models describe solids and Navier-Stokes equations describe fluids. Engineers generally base models for amorphous materials on empirical laws that fit laboratory data (such as velocity dependent friction), and these laws do not provide much physical insight into the deformation processes.

Molecular Dynamics simulations show that non-affine, or plastic, deformation in amorphous materials occurs when localized regions rearrange from one metastable configuration to another [24, 25]. A picture of one of these regions undergoing rearrangement between the two orientations is shown in Figure 1.6. These zones are known as Shear Transformation Zones (STZs), and STZ theory captures many features of experiments such as a yield stress and fracture. As the particles are sheared, the ellipse drawn through the center of the particles changes its orientation, and plastic deformation occurs (indicated by the dark regions in the image on the right). STZs are created and annihilated as energy is dissipated in the system, which allows the material to accumulate plastic strain. Therefore, instead of simulating every single particle in the system, we can capture the deformation by tracking the number of STZs and how frequently they flip. This approach results in a friction law that is tractable for modeling earthquake slip at the fault scale. However, we still need to determine the number of STZs. This requires finding a quantity that characterizes the internal degrees of freedom in an amorphous material.

Amorphous materials are poorly understood partially because they are systems far from equilibrium. Statistical mechanics provides a good description of equilibrium systems, but when systems of a large number of particles are actively provided with energy, the tools of equilibrium statistical mechanics are not useful. New techniques that describe the dynamics of systems that are driven away from equilibrium must be developed in order to understand amorphous materials.

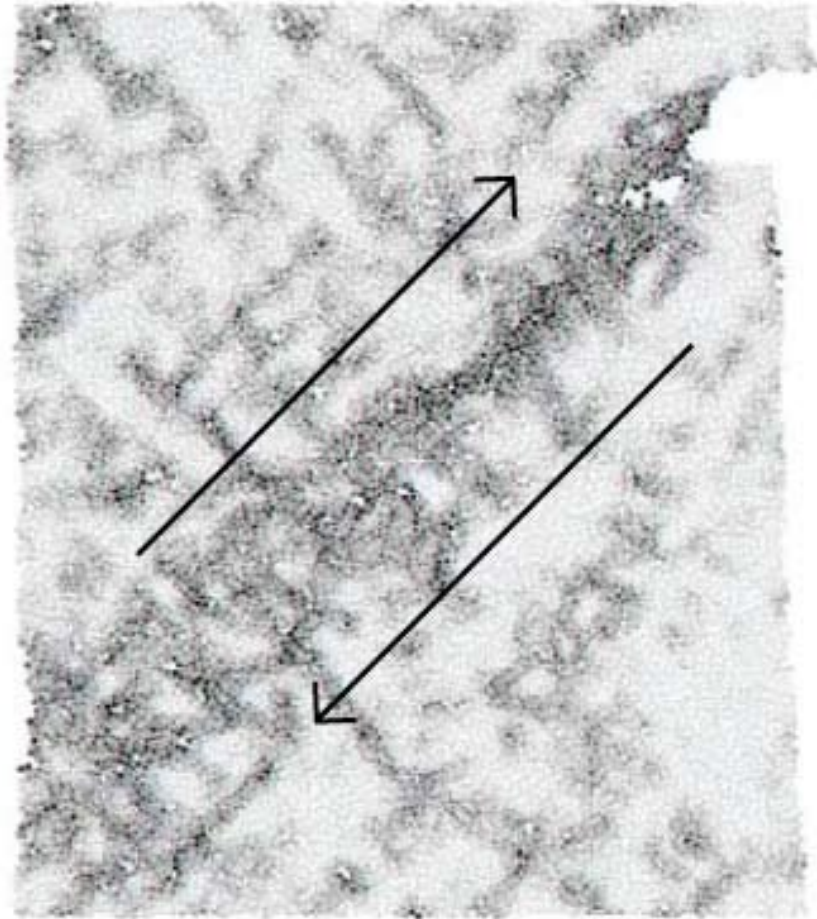


Figure 1.5: Image from a simulation of a glass under tensile strain. The resulting deformation shears the material, indicated by the arrows. The dark regions indicate where non-affine, or plastic, deformation occurs. The deformation localizes to a narrow shear band, which is common in the deformation of amorphous materials. Figure taken from Falk and Shi [26].

CHAPTER 1. INTRODUCTION

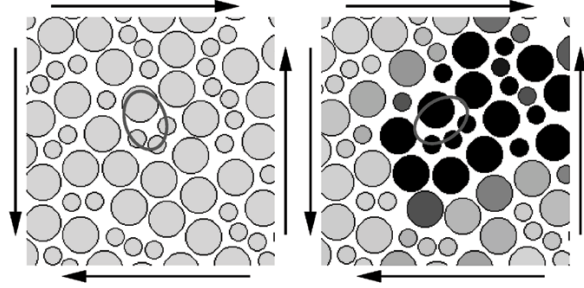


Figure 1.6: Plastic strain in a glass is accommodated in local regions called Shear Transformation Zones that rearrange between two metastable orientations. Initially, the particles are configured so that an ellipse drawn through their centers is oriented in one direction (left). As the material deforms plastically, the ellipse changes its orientation (right), and the dark regions indicate that plastic deformation has occurred. Figure taken from Falk and Langer [24] (Reprinted with permission. Copyright 1998 by the American Physical Society. <http://link.aps.org/abstract/PRE/v57/p7192>).

Sheared amorphous materials are constantly provided with energy, which is dissipated as the material flows. These materials frequently are stuck in a metastable disordered state instead of the lowest energy crystalline state. The thermal temperature does not describe the internal state of the system, and in the case of granular materials and other athermal systems, the thermal temperature can be completely irrelevant. Therefore, the challenge is to develop one or more macroscopic state variables (such as the state variable in DR friction) that quantifies the statistical properties of the internal degrees of freedom of the material.

One idea for such a state variable for amorphous materials is what is known as *effective temperature* [29]. In thermodynamics, temperature  $T$  is defined based on the partial derivative of the entropy  $S$  with respect to the internal energy  $E$ :

$$\frac{1}{T} = \frac{\partial S}{\partial E}. \quad (1.6)$$

The energy in this case is the internal energy of the individual constituents of the system. The effective temperature  $\chi$  is defined by the partial derivative of the entropy  $S$  with respect to the potential energy  $U$  of the packing:

$$\frac{1}{\chi} = \frac{\partial S}{\partial U}. \quad (1.7)$$

## CHAPTER 1. INTRODUCTION

The idea is that there is far more disorder in the packing of the system than there is in the kinetic degrees of freedom, and that the effective temperature better describes the internal state of an amorphous material than the thermal temperature.

Our approach in this thesis is to model deformation in amorphous materials using STZ Theory and effective temperature [29]. STZs are regions that are susceptible to plastic deformation because they are more disordered. An elevated effective temperature means that there are more STZs, and we can determine the number of STZs based on the value of the effective temperature. In addition to providing a physical basis for deformation in materials, the additional degrees of freedom captured by the effective temperature models strain localization, which is an important aspect of the deformation of amorphous materials.

### 1.4 Strain Localization

One aspect of the grain-scale physics that is of particular interest in this thesis is strain localization. Strain localization is the tendency of deformation in an amorphous material such as fault gouge to occur in a narrow band rather than throughout the material. This phenomena is illustrated in Figure 1.7, which plots the flow profile (top) and the strain rate profile (bottom) for homogeneous and localized deformation in simple shear. Figure 1.7(a) shows the profiles for homogeneous deformation. In this case, the strain occurs uniformly throughout the entire layer. This is the expected flow profile for a Newtonian Fluid. Strain localization occurs in Figure 1.7(b). In this situation, flow is confined to a narrow region, and the portions of the material above and below move intact with the boundaries. There is a peak in the strain rate profile when localized strain occurs. Strain localization tends to occur in many different amorphous solids, including fault gouge [30] and bulk metallic glasses [31, 26].

Localized strain within a layer of fault gouge is observed in a wide range of studies of faulting. One example is numerical simulations of a layer of fault gouge [30]. In these numerical studies, a collection of gouge particles with a distribution of particle diameters is sheared. The simulations produce results similar to the glassy material shown in Figure 1.5 [26]. Deformation localizes to a region narrow relative to the entire thickness of the material.

Localization is also observed in rock friction laboratory experiments [32, 33, 34, 35]. In these experiments, a layer of fault gouge is sheared between two larger blocks, and the frictional strength is measured. After the experiment is complete, the microstructures that develop in the gouge are examined, and localized strain

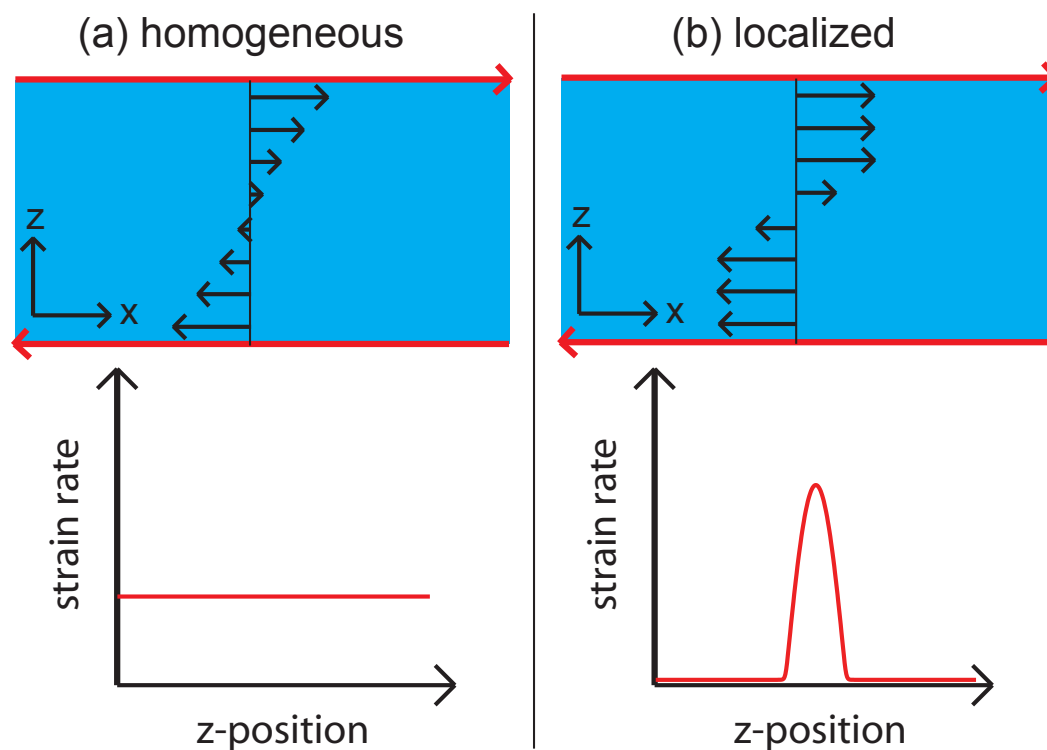


Figure 1.7: Illustration of homogeneous and localized deformation in amorphous materials. The upper picture for each type of deformation shows the flow profile in the material, and the lower picture shows the strain rate as a function of position. (a) Homogeneous deformation occurs throughout the material. The flow transitions from the top boundary to the bottom boundary in a smooth manner, and the strain rate is uniform throughout the layer. (b) Localized deformation results in a sharp transition from flow in one direction to flow in the other. The upper half of the material moves in unison, as does the lower half of the material, with deformation occurring in a narrow region in the middle. There is a peak in the strain rate for localized deformation.

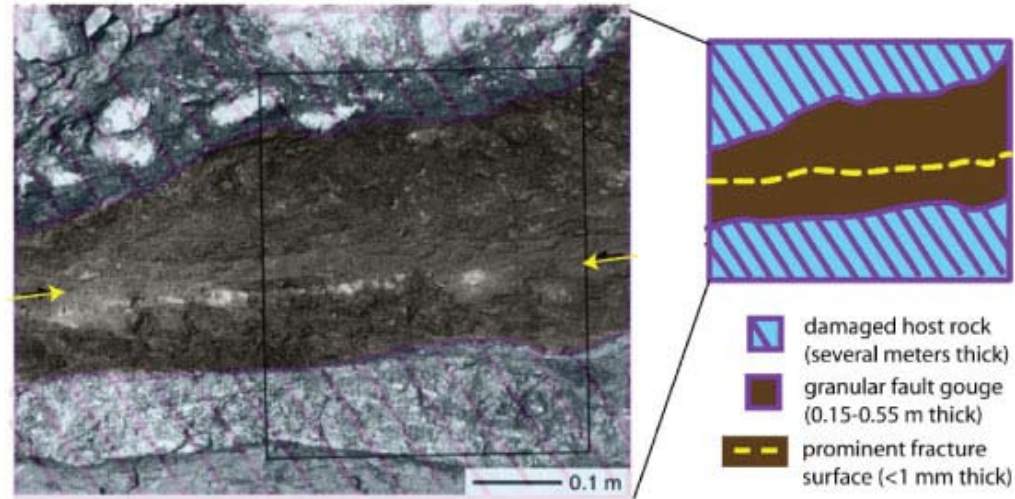


Figure 1.8: Field observations from an exhumed earthquake fault. The fault was formerly at seismogenic depths, where it experienced many earthquake cycles prior to uplift bringing it to the surface. The fault contains a layer of a finely crushed fault gouge (dark material), and the slip in the gouge is localized in a narrow shear band (yellow arrows). Figure adapted from Chester and Chester [37] (Reprinted with permission. Copyright 1998 by Elsevier.).

is observed.

Shear bands in fault gouge are also seen in field observations of exhumed faults [36, 37, 38]. An exhumed fault was formerly at seismogenic depths, where it experienced many earthquake cycles, and through uplift and erosion is now at the surface. Observations of exhumed faults indicate that most of the deformation is localized to a narrow shear band, also known as a prominent fracture surface, within the fault zone. Figure 1.8 illustrates the observed features of the fault core of the Punchbowl Fault in Southern California [37]. Similar observations were made on the Median Tectonic Line in Japan [38].

Strain localization is also observed in rocks that are deformed in a ductile manner below the seismogenic zone [39], illustrated in Figure 1.9. At the high temperatures and pressures deep in the earth's crust, rock friction is rate strengthening [15, 16, 17]. This means that as the material is driven at a larger strain rate, the frictional resistance increases. Earthquakes cannot nucleate in regions with rate strengthening frictional properties, and instead the fault creeps slowly.

## CHAPTER 1. INTRODUCTION

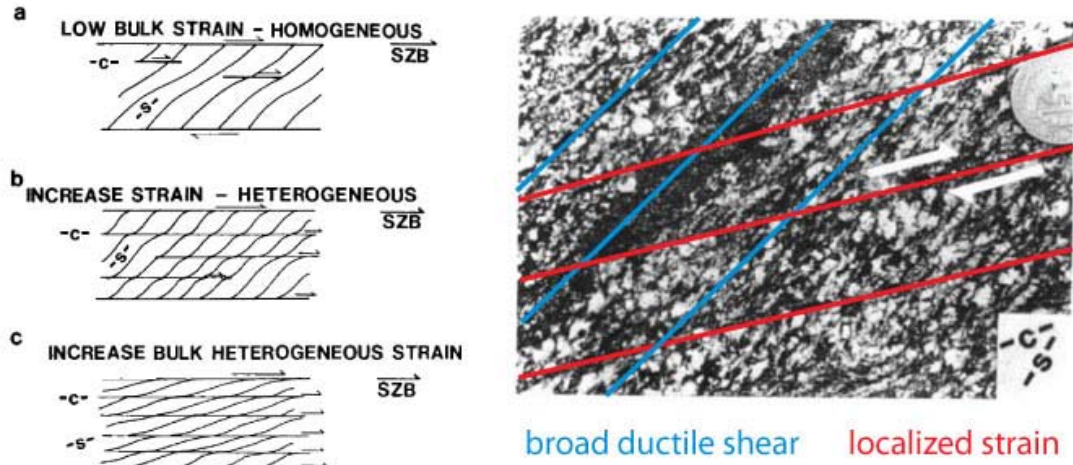


Figure 1.9: Rocks deformed below the seismogenic zone. At the large temperatures and pressures deep in the earth, the rock deforms in a ductile manner. (a) The fabric in the rocks is due to a combination of broad, ductile shear, and localized strain from earthquakes that originate in the seismogenic zone and propagate to depth. The broad shear is indicated by the diagonal lines, and the localized coseismic slip produces the horizontal lines. (b) Field observations of this deformation. The blue lines indicate the ductile shear, and the red lines show the location of localized shear. Figure adapted from Simpson [39].

This results in a broad shear fabric forming in the rocks, shown as the diagonal lines in Figure 1.9(a) and the blue lines in Figure 1.9(b). The localized strain in these rocks occurs instead when earthquakes nucleate in the seismogenic zone and propagate down to the creeping region – the horizontal lines in Figure 1.9(a) and the red lines in Figure 1.9(b). The combination of slow, broad shear during the interseismic period and localized coseismic strain produces a distinct fabric in the rocks.

Localization does not occur in all fault zones, as demonstrated by observations from the San Andreas Fault Observatory at Depth (SAFOD) project [40]. The SAFOD observations involve drilling through the actively creeping portion of the San Andreas Fault near Parkfield, CA. Samples of the fault zone show no fracture surface or other localized deformation within the fault gouge in the San Andreas [41]. Instead, the core samples show that deformation occurs throughout two gouge layers that are each a couple of meters thick.

The variety of observations of localization, both in the field and in other stud-

ies, highlights the need to develop models that explain localization on a physical basis. One of the problems of simple friction laws such as slip weakening or Dieterich-Ruina is that the laws do not explicitly account for localization. Friction experiments exhibit localization, which means that constitutive parameters extracted from these experiments reproduce the frictional strength of localized shear. However, it is preferable that the friction model explicitly captures the strain profile in the fault zone, and dynamically chooses if strain is broad or localized. This allows us to explore how the dynamics of strain localization influence larger scale frictional behavior and the propagation of earthquake ruptures.

## 1.5 Dynamic Earthquake Rupture

At the fault scale, dynamic ruptures propagate in space and time due to instabilities in the nonlinear friction law governing rupture. Ruptures are modeled by solving for the elastodynamic response of two large blocks of rock governed by a friction law at their interface. The fault is loaded with an initial shear stress, and rupture is initiated by increasing the stress on a small patch. The model then solves for the spontaneous propagation of slip along the fault, and the resulting ground motion at the earth's surface.

A simple example of rupture propagation in a dynamic earthquake simulation is shown in Figure 1.10. The simulation shows the evolution of slip rate as a function of space and time. The rupture nucleates at the center and it spontaneously propagates out to the edges of the fault. The rupture front approaches a limiting speed (slightly less than the shear wave speed), and the largest slip rate occurs right behind the rupture front because strain energy is being released rapidly from the elastic bulk.

An important area of research in seismology is to determine the range of expected ground motions in earthquakes. Dynamic rupture modeling has revealed several aspects of rupture that affect fault scale ground motion. Here, we discuss these source properties and how the friction law governing rupture propagation plays a central role in determining the effect on ground motion.

### 1.5.1 Heterogeneities

Heterogeneities in the shear stress and frictional properties contribute to ground motion in a variety of ways. An example of a rupture with heterogeneous initial conditions in the shear stress and frictional properties is shown in Figure 1.11. This type of heterogeneity affects rupture over all of the fault, and consequently

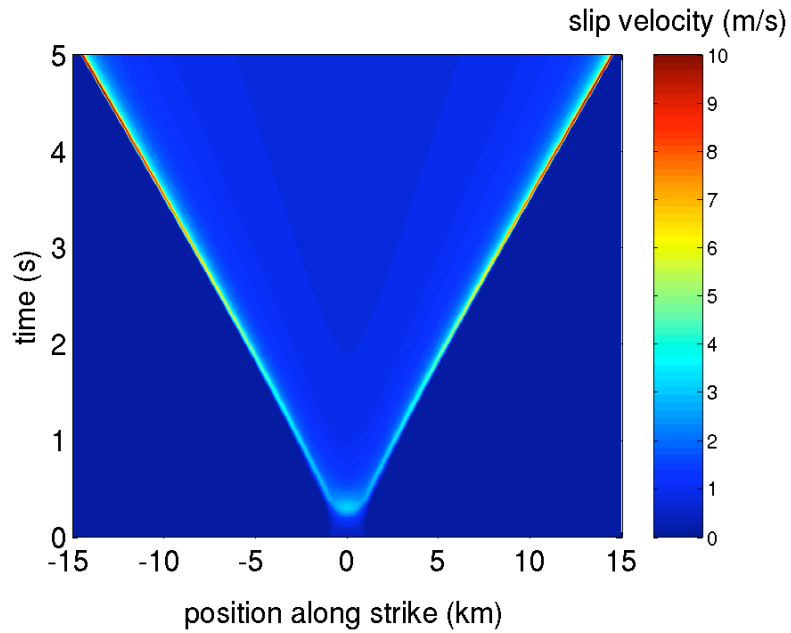


Figure 1.10: Dynamic rupture propagation in space and time on a simple earthquake fault. The plot shows the slip velocity as a function of space and time. Rupture nucleates at the center of the fault, and the rupture spontaneously grows until it encounters the edge of the fault. Slip accelerates quickly up to the limiting wave speed, which is slightly less than the shear wave speed in the rock. The largest slip rates occur right behind the rupture front, as that is where strain energy is being released from the elastic bulk.

## CHAPTER 1. INTRODUCTION

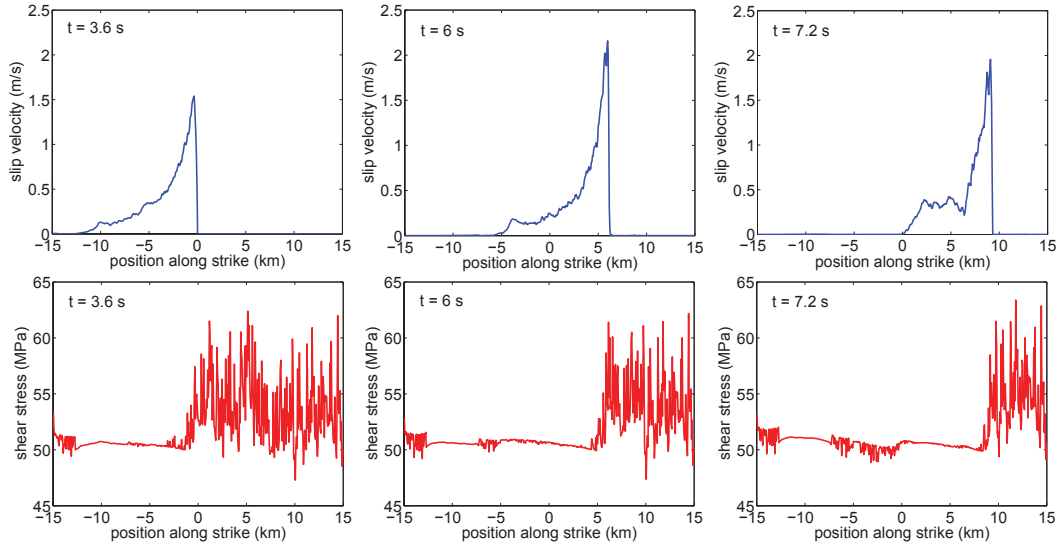


Figure 1.11: Slip rate and shear stress as a function of position for a dynamic rupture with heterogeneous initial stress and friction parameters at several times. The plot shows the slip rate and shear stress at 7.5 km depth. The heterogeneity of the initial stress result in a slip rate that is heterogeneous as a function of position, and the rupture velocity is only 80% of the shear wave speed. Additionally, because the rupture encounters the edge of the fault on the left of the plot, rupture to the left arrests and rupture propagates to the right in a pulse-like manner.

it also impacts the ground motion in the earthquake. Heterogeneities that only affect a small area of the fault are also important for determining the ground motion in an earthquake. These smaller heterogeneities include asperities, which are heterogeneities in the shear stress, and barriers, which are heterogeneities in the frictional properties.

An asperity is a fault region with an elevated pre-stress. A rupture that encounters an asperity ruptures at a larger rupture velocity (either by accelerating to the limiting wave speed, or by nucleating supershear rupture) and radiates additional seismic energy. This is because the increased pre-stress means that there is more elastic strain energy released during fault slip, which is radiated away from the fault. The effect of a small asperity with an elevated prestress on a dynamic rupture is shown at the left in Figure 1.12 [42].

Barriers are strong regions on the fault, with an elevated strength (larger peak shear stress in a slip-weakening model, or larger direct effect  $a$  in the DR law). Ruptures that encounter a barrier slow and can arrest, but the rupture can break

CHAPTER 1. INTRODUCTION

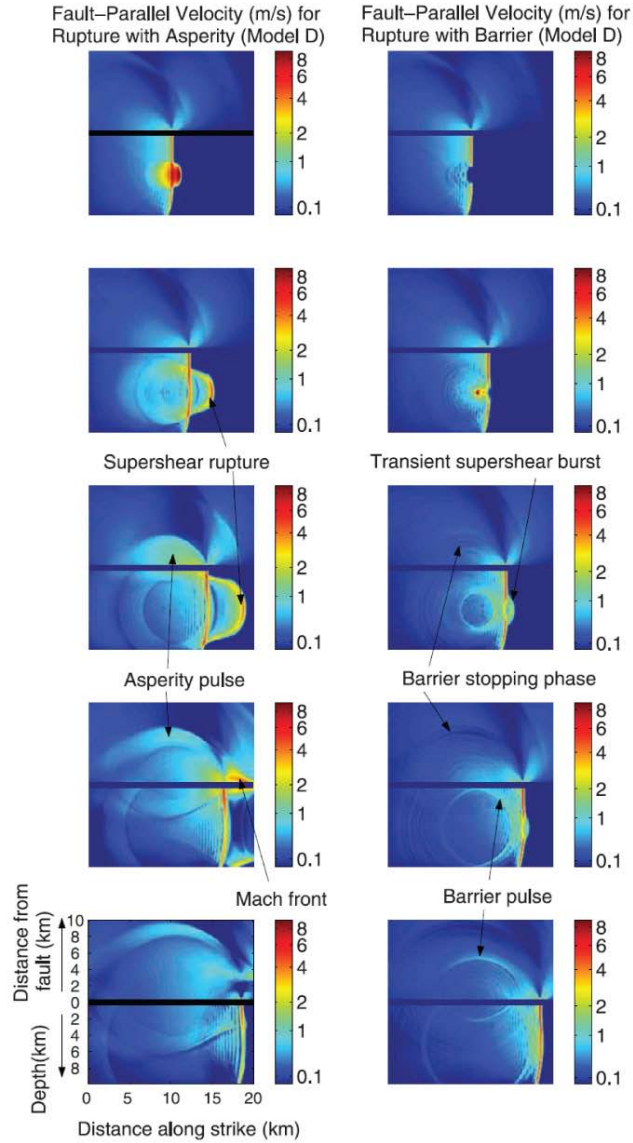


Figure 1.12: Dynamic rupture simulations with a small asperity or barrier on the fault. The left plots show rupture propagation with an asperity with an elevated initial shear stress. The asperity causes the rupture to reach supershear rupture speeds, and there is a pulse in the ground motion away from the fault. The right plots show the rupture dynamics from a strong frictional barrier, which slows the rupture and produces a delayed pulse in the ground motion away from the fault. Figure taken from Page *et al.* [42].

## CHAPTER 1. INTRODUCTION

through the barrier by slipping in areas adjacent to the barrier and focusing its energy in the barrier. If the rupture manages to break the barrier, the ground motion at the surface is changed. This is because the resistance of the barrier stores up elastic strain energy, which is released quickly once the barrier breaks. Because the rupture slows upon encountering the barrier, and then accelerates upon breaking the barrier, the barrier changes the ground motion away from the fault. Rupture propagation and ground motion for a rupture that encounters a barrier is shown at the right in Figure 1.12 [42].

Numerous other studies have investigated the role of heterogeneities in dynamic rupture models [4, 5, 43, 44]. These models show that realistic stress heterogeneities produce dynamic ruptures that take a complex path across the fault [45]. This indicates that heterogeneity is an essential aspect of reproducing the ground motions in real earthquakes. However, an underlying aspect of the friction law may still play an important role in earthquake rupture. Therefore, seismologists still employ simple rupture models to isolate the effect of constitutive laws and gain insight into the effects of friction. In this thesis, we focus on simple ruptures to ensure that our simulations examine the fault scale impact of small scale physics. Friction laws impact other aspects of dynamic rupture even on simple faults. These include the rupture speed and the type of rupture, and we discuss the effect of these aspects on ground motion in the following sections.

### 1.5.2 Rupture Speed

The speed at which the rupture front propagates along the fault plays a significant role in determining the ground motion in an earthquake. The frictional properties of the fault dictate the rupture speed, as an earthquake can rupture through a frictionally weak fault with a large rupture velocity, but a rupture that encounters strong barriers to rupture cannot reach as large a rupture velocity. The friction law also plays a key role in nucleating supershear ruptures that travel faster than the shear wave speed [46].

Rupture speed is important due to the effects of directivity [47]. Directivity is the increase in frequency of ground shaking due to the Doppler effect. Ground motion in the rupture direction has a larger high frequency content. The faster the source is moving along the fault, the larger the Doppler shift, and so fast moving ruptures alter the expected ground motion.

A fault with many frictional barriers leads to lower rupture speeds, as the rupture dissipates additional energy to break through the strong patches on a fault. Lower values of the initial stress also slows down ruptures, as less strain energy is released from the elastic bulk. Less released strain energy also decreases the

## CHAPTER 1. INTRODUCTION

energy that can be radiated as seismic waves, decreasing the intensity of ground shaking. Heterogeneous distributions of friction parameters and the initial stress also influence ground motion. If the strong patches (high frictional resistance or low initial stress) are small and evenly distributed throughout the fault, the earthquake must break through them in order to rupture the entire fault, and a lower rupture velocity occurs. An example of this is shown in Figure 1.11, which includes plots of slip velocity and shear stress as a function of position for several times during a dynamic rupture. The shear stress plots show that the initial stress is extremely heterogeneous, and this leads to a rupture velocity that is only about 80% of the shear wave speed. Less heterogeneous ruptures can reach speeds of 94% of the shear wave speed, or even exceed the shear wave speed in the case of supershear rupture. If the strong patches are grouped together, then the rupture can reach faster rupture speeds by following the large weak patches across the fault [48].

Rupture speed can also impact ground motion by the rupture exceeding the shear wave speed [49]. In these supershear ruptures, the rupture front propagates faster than the shear wave speed. An example of supershear rupture propagation is shown in Figure 1.13(a), which plots slip velocity as a function of position along the fault. A supershear rupture typically starts out as a rupture propagating slower than the shear wave speed, and then supershear rupture nucleates out ahead of the subshear rupture and propagates faster than the shear wave speed. This is shown in Figure 1.13(a), as the largest peak in the slip rate is the rupture traveling at subshear speeds, and the smaller peak closer to the ends of the fault are traveling faster than the shear wave speed. Supershear ruptures only occur for in-plane slip, where the rupture propagation direction and the sense of slip on the fault are identical. In this geometry, ruptures can propagate at speeds below the Rayleigh wave speed (slightly less than the shear wave speed), and above the shear wave speed, but not between the Rayleigh and shear wave speeds. Ruptures cannot propagate at speeds in this “forbidden” region because energy is not dissipated at the crack tip in these solutions, which is unphysical [49]. Supershear earthquakes are important for determining ground motion because supershear rupture speeds produce shear waves that do not attenuate with distance from the fault [49]. This results in large ground motions significantly further from the fault than for sub-Rayleigh ruptures. Transient increases in rupture velocity to supershear speeds, as opposed to sustained supershear rupture, can also occur due to barriers that require rupture fronts to focus their energy on breaking the strong patch [50].

The initial shear stress on the fault and the frictional length scale ( $d_c$  in a slip-weakening law, or  $L$  in a DR law) both determine if a rupture can reach supershear speeds [46]. A high shear stress and a small frictional length scale

## CHAPTER 1. INTRODUCTION

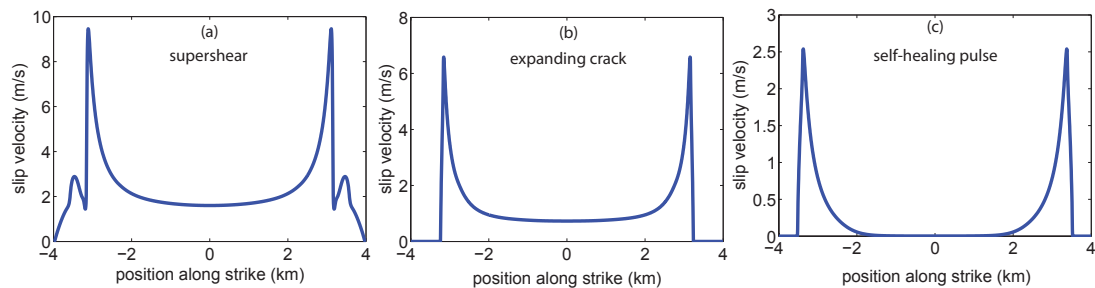


Figure 1.13: Illustration of different ways that earthquakes can rupture a fault. The plots show slip velocity as a function of position along the fault. (a) Supershear rupture occurs at high stresses and small frictional length scales. The rupture begins at a subshear rupture speed (larger inner peaks on the slip rate curve), but rupture that exceeds the shear wave speed nucleates shortly thereafter (smaller outer peaks on the slip rate curve). (b) Crack-like rupture propagation occurs at intermediate values of the shear stress. In a crack-like rupture, the center of the fault continues to slip for the duration of the earthquake. (c) Pulse-like rupture propagation, where a point on the fault slips and then heals shortly thereafter. Pulse-like rupture can occur due to rupture in one direction arresting, or in a self-healing manner. Self-healing pulses occur for low values of the initial shear stress, and only occur for friction laws that exhibit time-dependent healing.

favor supershear rupture propagation. Any heterogeneity in the shear stress or friction law also plays a role, as large patches of high initial stress or small frictional length scale tend to result in supershear rupture [51].

### 1.5.3 Rupture Types

Slip can propagate in space and time on a fault a fault in different ways. Many dynamic rupture simulations produce crack-like rupture [52, 2, 3, 5], which is shown in Figure 1.13(b). In an expanding crack rupture, the earthquake initiates at the hypocenter and propagates bi-laterally until it reaches the fault boundaries or strong patches that it is unable to break. The rupture then arrests, which means that the hypocenter slips for the entire duration of the earthquake. Ruptures with slip-weakening friction usually produce crack-like slip profiles due to the lack of healing in the constitutive model.

Alternatively, the rupture can propagate as a self-healing pulse. Figure 1.13(c) shows the slip rate as a function of position for a self-healing pulse. In the case of a self-healing pulse, a point on the fault slips and then heals shortly afterwards. Every point on the fault slips for much less than the duration of the earthquake, which produces a slip profile that differs from an expanding crack. A pulse-like rupture starts out in a crack-like manner, but soon afterwards the center of the fault heals, and the earthquake remains pulse-like for its duration. Pulse-like rupture requires a time-dependent healing mechanism to arrest slip. Zheng and Rice [19] found that pulse-like rupture also requires low initial shear stress and friction that weakens strongly with slip velocity. These ruptures tend to have larger slip rates than crack-like slip, but a shorter slip duration. The ground motion in earthquakes is sensitive to the slip duration (rise time), which indicates that pulse-like rupture produces ground motion different from a crack-like rupture. Earthquake observations indicate that rupture often occurs in a pulse-like manner [53]

Pulse-like rupture can occur in slip-weakening friction laws when a bi-lateral rupture encounters a barrier to rupture (low shear stress or strong frictional properties) in one direction [54]. These pulse-like ruptures are different from self-healing pulses in that the fault heterogeneity, and not the friction law, are responsible for the arrest of slip. An example of a pulse-like rupture that occurs due to a strong barrier in one direction is shown in Figure 1.11. Heterogeneities can also produce pulse-like rupture [43, 55].

## 1.6 Dissertation Outline

Our goal in this work is to explore the implications of microscopic plastic deformation and strain localization across scales in friction and earthquake rupture problems. This is a “vertical” approach to the multi-scale earthquake problem, and we investigate the larger scale impact of strain localization in earthquake rupture. In general, the dissertation is organized by scale, and we move from smaller to larger scales. The earlier chapters outline how STZ Theory captures grain scale physics and interface scale friction dynamics, and the later chapters focus on fault scale dynamic ruptures. The one exception is in Chapter 6, where we look at both laboratory scale deformation and fault scale rupture with rate strengthening materials.

First, we start at the grain scale and discuss our constitutive model for amorphous materials. We develop the general STZ constitutive equations, as well as some simplifying assumptions and limiting cases. In general, the effective temperature in the STZ model is governed by a partial differential equation, which has many more degrees of freedom than a single state variable governed by an ordinary differential equation (i.e. DR friction). However, if the strain rate is uniform across the width of the material (homogeneous strain in Figure 1.7), then the governing equation for the effective temperature reduces to an ordinary differential equation. This version of the STZ model is known as the Free Volume law.

We show that the STZ equations match the logarithmic rate dependence observed in laboratory experiments. The important differences between the STZ and DR laws relate to the frictional length scale, and the formation of shear bands. The STZ law predicts that the frictional length scale should increase with increasing slip rate, which matches observations from laboratory experiments. The formation of a shear band also has important implications for friction, as a shear band reduces the frictional length scale, and decreases the dynamic sliding friction. Our research explores the large scale implications of these important differences in friction dynamics.

At the interface scale, we explore how strain localization impacts the dynamics of friction. In particular, we examine the effect of shear bands on stick-slip instabilities in sheared amorphous materials. We find that localization has a measurable effect on the parameter ranges that produce stick-slip motion, and we perform a linear stability analysis to predict when motion transitions from steady sliding to stick-slip. Our predictions are confirmed through numerical integration, and we also explore the role of strain localization in irregular stick-slip events.

We explore the impact of STZ theory with and without localization at the

## CHAPTER 1. INTRODUCTION

fault scale. We study rupture propagation on simple 2D faults with uniform stress and frictional properties to focus on the effects of constitutive laws. For the FV law, we make careful comparisons between friction laws to assess the fault scale consequences of a frictional length scale that increases with increasing slip rate. We examine the slip rate on the fault, the manner in which shear stress weakens with slip, and when supershear rupture nucleates on the fault. We also explore how the difference in the frictional length scale effects rupture governed by friction laws with rapid velocity weakening at seismic slip rates. We compare the FV and DR laws to determine when ruptures with rapid weakening transition to supershear, and when rupture propagates as a self-healing pulse. Our results show that changing the microscopic physics has fault scale consequences for dynamic rupture.

In a similar manner, we look at the role of strain localization in fault scale dynamic rupture. We compare FV law ruptures, where the strain rate does not vary across the width of the fault zone, and STZ ruptures where the effective temperature dynamics dictates the strain rate profile in the fault zone. We look at the dynamics of localization during an earthquake rupture, and compare the evolution of shear stress as a function of slip. We also determine when rupture propagates as an expanding crack, supershear crack, and expanding pulse as a function of the shear band width. This demonstrates that the dynamic weakening of strain localization can affect fault scale aspects of dynamic rupture propagation.

The results discussed above explore implications of localization in rate weakening materials. Rate strengthening materials are also extremely important, and include rocks at high temperatures and pressures below the seismogenic zone, and metallic glasses. Chapter 6 discusses the effect of localization in these systems, which exhibit a variety of types of deformation. We briefly look at localization in glassy materials, and discuss the implications of strain localization for deformation in rocks below the seismogenic zone.

Finally, we discuss the importance of these results in Chapter 7, and examine other avenues for further research.

# Chapter 2

## STZ Friction Law

We begin our study of the multi-scale earthquake problem at the smallest scale of grains. We outline the physical basis for the Shear Transformation Zone (STZ) model, which captures the physics occurring at the grain and gouge scale of the earthquake problem. The STZ model is used to incorporate the small scale physics in all of the larger scale studies throughout this dissertation. This ranges from the interface scale in laboratory experiments to the fault scale in earthquakes.

The introduction presents the basic ideas for STZ Theory, and this chapter builds upon these basic assumptions and develops the mathematical equations of the theory. Because all of the larger scale studies rely on the STZ model, the discussion is drawn from several papers. This includes work that discusses the Free Volume version of STZ Theory by Daub and Carlson that is published in the *Journal of Geophysical Research* [56], as well as research that uses the effective temperature version by Daub, Manning, and Carlson that is published in *Geophysical Research Letters* [57].

### 2.1 Basic Assumptions

As discussed in the introduction, we model friction with STZ Theory, a continuum approximation for plastic deformation in dense amorphous solids. STZ Theory has been applied to a wide variety of systems, including fracture of glassy materials [24, 25], boundary lubrication [58], and granular flow [27]. Because the physics at the smallest scales is poorly constrained in the earthquake problem, we use STZ Theory in our simulations because it captures the observed microscopic deformation in many different materials.

The deformation of an amorphous solid can be approximated by two components – affine displacements, where the individual particle displacements are

## CHAPTER 2. STZ FRICTION LAW

uniform (elastic), and non-affine displacements, where the individual particle motions are heterogeneous (plastic). Simulations of sheared amorphous materials indicate that the non-affine displacements tend to occur in small, localized regions, called Shear Transformation Zones (STZs) [24, 25]. The simulations find that these STZs constitute a small collection of particles switching between two metastable orientations under applied shear stress.

STZs switch between two metastable orientations, denoted “positive” and “negative.” When a “positive” orientation changes to a “negative” orientation, the plastic strain increases by a fixed increment, and when a “negative” orientation switches to a “positive” orientation, the plastic strain decreases by a fixed increment. An STZ undergoing a switch from “positive” to “negative” is shown in Figure 1.6. Once an STZ has switched to the “negative” orientation, the material cannot shear further at that location. Therefore, to accumulate shear the material is constantly creating and destroying STZs as energy is dissipated in the system.

The STZ friction model incorporates the microscopic observations of non-affine particle displacements by assuming that all plastic deformation occurs through STZ rearrangements. Each reversal from one orientation to the other accumulates a certain amount of plastic strain, and a threshold shear stress must be applied for the reversal to occur. STZ Theory treats the populations of the two STZ orientations as dynamic state variables. STZs can flip from one orientation to the other, and are created and destroyed as the system is sheared. Creation and annihilation drive the number density of STZs towards a Boltzmann distribution, with an effective temperature  $\chi$ . The effective temperature describes the configurational disorder in the material. Regions that have a higher effective temperature are more disordered, have a higher density of STZs, and accommodate more plastic strain.

Quantitatively, STZ theory determines the plastic strain rate  $\dot{\gamma}$  in the material based on two factors: the effective temperature, which determines the number of STZs, and the shear stress  $\tau$ , which determines how frequently the STZs switch orientation. We summarize these two contributions as follows:

$$\dot{\gamma} = f(\tau) \exp(-1/\chi). \quad (2.1)$$

The function  $f(\tau)$  describes how the STZ reversals depend on the shear stress, and the effective temperature term  $\exp(-1/\chi)$  determines the total number of STZs. This approach is far more efficient than simulating every single particle in the fault – instead, we simply determine the number of STZs by tracking the evolution of the effective temperature, and the shear stress determines how frequently the STZs change orientation.

## CHAPTER 2. STZ FRICTION LAW

In the following sections, we derive Equation 2.1 and the evolution equation for the effective temperature. We also discuss the Free Volume Law, a simplification to the STZ model that assumes that shear strain is homogeneous throughout the material [59]. Finally, we examine the dynamics of friction in the STZ model and show that the small scale physics can affect the larger scale dynamics of earthquake rupture and material deformation.

### 2.2 STZ Equations

STZ Theory calculates the plastic strain rate  $\dot{\gamma}$  based on four quantities: the shear stress  $\tau$ , the number of STZs in each of the two possible orientations  $n_+$  and  $n_-$ , and the effective temperature  $\chi$  [29]. The number of STZs in each orientation and the effective temperature quantify the internal state of the material. In this dissertation we incorporate a typical approximation which assumes the number of STZs in each orientation is equal to its steady state value. This approximation is valid when the STZ time scale is much faster than other dynamical processes in the problem. Here, we present the details of the derivation of the STZ equations and the simplifying assumptions necessary for setting the STZ populations to steady state.

Quantitatively, the basic premise of STZ Theory can be written as follows:

$$\dot{\gamma} = \frac{2\epsilon}{n_\infty t_0} [R(+\tau) n_+ - R(-\tau) n_-]. \quad (2.2)$$

The plastic strain rate  $\dot{\gamma}$  is the net sum of all the STZ reversals in the material. The function  $R(\tau)$  describes the rate at which STZ reversals take place in response to the applied shear stress. The other parameters are the strain increment per STZ reversal  $\epsilon$ , a reference STZ population  $n_\infty$ , and the time scale for STZ reversals  $t_0$ .

Equation (2.2) can be rewritten with the following change of variables:

$$\Lambda = \frac{n_+ + n_-}{n_\infty}, \quad m = \frac{n_- - n_+}{n_+ + n_-}. \quad (2.3)$$

The variable  $\Lambda$  is proportional to the total number of STZs, and  $m$  quantifies the bias. With these variables, the constitutive law becomes

$$\dot{\gamma} = \frac{2\epsilon}{t_0} \mathcal{C}(\tau) \Lambda [\mathcal{T}(\tau) - m]. \quad (2.4)$$

## CHAPTER 2. STZ FRICTION LAW

The rate switching function is rewritten in the combinations  $\mathcal{C}(\tau) = (R(\tau) + R(-\tau))/2$  and  $\mathcal{T}(\tau) = (R(\tau) - R(-\tau))/(R(\tau) + R(-\tau))$  in this version of the constitutive law.

In this dissertation, we assume an exponential form for the rate switching function [60]:

$$R(\tau) = \exp(-f_0 + \tau/\sigma_d). \quad (2.5)$$

The rate switching function depends on an activation stress  $\sigma_d$ , and an activation energy scaled by the thermal energy. The activation stress is known as the direct effect stress in rock mechanics experiments – its magnitude is typically much less than the shear stress ( $\tau/\sigma_d \gg 1$ ). This form for  $R(\tau)$  reproduces the logarithmic rate dependence seen in rock mechanics experiments [56]. Other forms for  $R(\tau)$  have been proposed, including functions with a power law dependence on the stress [61]. The rate switching function combinations are then  $\mathcal{C}(\tau) = \exp(-f_0) \cosh(\tau/\sigma_d)$  and  $\mathcal{T}(\tau) = \tanh(\tau/\sigma_d)$ . Under the approximation that  $\tau/\sigma_d \gg 1$ , we set  $\mathcal{T}(\tau) \approx 1$ .

The STZ populations dynamically evolve as the material is sheared. The STZs can switch between the two orientations, and STZs are created and destroyed. Therefore, the evolution equation for the STZ populations are

$$\frac{dn_{\pm}}{dt} = \frac{1}{t_0} [R(\mp\tau) n_{\mp} - R(\pm\tau) n_{\pm}] + \frac{\dot{\gamma}\tau}{\epsilon(n_+ + n_-)\tau_y} \left[ \frac{n_{\infty}}{2} \exp(-1/\chi) - n_{\pm} \right]. \quad (2.6)$$

The first term accounts for STZs switching from “positive” to “negative” and vice versa, and the second term incorporates STZ creation and annihilation. The overall creation/annihilation rate is proportional to the rate at which work is done on the material. The creation term includes effective temperature dependence, as we assume that energy dissipation in the material drives the STZ population towards a Boltzmann distribution. The stress  $\tau_y$  determines the fraction of dissipated energy that creates STZs, and it also turns out to be the threshold stress that must be applied to switch an STZ.

In the  $\Lambda$  and  $m$  variables, the evolution equations become

$$\frac{d\Lambda}{dt} = \frac{\dot{\gamma}\tau}{n_{\infty}\Lambda\tau_y} [\exp(-1/\chi) - \Lambda]; \quad (2.7)$$

$$\frac{dm}{dt} = \frac{\dot{\gamma}}{\epsilon n_{\infty}\Lambda} \left\{ 1 - \frac{\tau m}{\tau_y} [1 + \exp(-1/\chi) - \Lambda] \right\}. \quad (2.8)$$

We note that the dynamic equations for  $\Lambda$  and  $m$  both have a factor of  $1/(n_{\infty}\Lambda) = 1/(n_+ + n_-)$ . For the equations of STZ Theory to be valid, STZs must be rare,

CHAPTER 2. STZ FRICTION LAW

otherwise the assumption that plastic strain occurs in local, isolated regions is no longer valid. Therefore, the total number of STZs is small, and the STZ populations evolve quickly relative to the stress and effective temperature. With this in mind, we simplify the STZ equations and assume the total number of STZs is always at its steady state value  $\Lambda = \exp(-1/\chi)$ , which is set by the local effective temperature.

If we set the total number of STZs to steady state, then the STZ bias is  $m = \tau_y/\tau$ . However, the STZ bias cannot be larger than  $m = 1$ , which corresponds to all the STZs in the “negative” orientation. When this occurs, the material cannot be sheared further because there are no regions susceptible to deformation. This means that if  $\tau < \tau_y$ , then the material is jammed and  $\dot{\gamma} = 0$ . Otherwise, the material flows. Therefore, the steady state value for the STZ bias is dependent on the stress as follows:

$$m = \begin{cases} 1, & \tau < \tau_y; \\ \tau_y/\tau, & \tau \geq \tau_y. \end{cases} \quad (2.9)$$

The STZ dynamics are important for determining if the material is jammed or flowing, but otherwise the stress and effective temperature have the dominant effect on the friction dynamics.

The friction law that we use in our simulations is therefore

$$\dot{\gamma} = \frac{2\epsilon}{t_0} \exp(-f_0) \cosh[\tau/\sigma_d] \exp(-1/\chi) \left[1 - \frac{\tau_y}{\tau}\right], \quad (2.10)$$

unless  $\tau < \tau_y$ , in which case  $\dot{\gamma} = 0$ . This is the exact version of Equation (2.1). The strain rate depends on the shear stress, and the internal state of the material is described entirely by the effective temperature. We now propose a dynamic equation for the effective temperature, which determines the dynamics of friction in STZ Theory.

## 2.3 Effective Temperature Evolution

In addition to the relation between strain rate, stress, and effective temperature (Equation (2.1)), the model requires a dynamic evolution equation for the effective temperature. Effective temperature is different from the thermal temperature, but it evolves in a similar manner. In this section, we propose a heat equation that governs the evolution of the effective temperature. Unlike state variables in friction laws such as Dieterich-Ruina, which are governed by an ordinary differential equation, effective temperature follows a partial differential equation.

## CHAPTER 2. STZ FRICTION LAW

This results in a model with many more degrees of freedom that captures the spontaneous localization of strain in amorphous materials..

In our heat equation for the effective temperature, we include terms for energy dissipation, diffusion, and time-dependent relaxation:

$$\frac{\partial \chi}{\partial t} = \frac{\dot{\gamma} \tau}{c_0 \tau_y} \left( 1 - \frac{\chi}{\hat{\chi}(\dot{\gamma})} \right) + \frac{\partial}{\partial z} \left( \dot{\gamma} D \frac{\partial \chi}{\partial z} \right) + R_0 \left( 1 - \frac{\chi}{\chi_0} \right) \exp(-\beta/\chi). \quad (2.11)$$

As work is done on the material, the dissipation term drives the effective temperature towards some maximum effective temperature  $\hat{\chi}(\dot{\gamma})$  that depends on the strain rate [61]. Shearing the material stirs up the particles, and the grains in the system can find higher energy configurations. As the strain rate in the material increases, the maximum effective temperature rises.

Our choice of  $\hat{\chi}(\dot{\gamma})$  is based on the observed rate dependence of the steady-state effective temperature in a simulated glass [61]. Figure 2.1 plots simulation data, along with fits. The vertical axis plots the negative logarithm of the non-dimensional strain rate  $q = t_0 \dot{\gamma}$ , and the horizontal axis plots the inverse effective temperature. On these axes, larger strain rates and larger effective temperatures are located at the lower left corner. The different colors indicate varying thermal temperature in the simulations. There are two regimes for this curve: at low strain rates, the effective temperature is independent of the strain rate, and at high strain rates the effective temperature follows a linear plot on these axes. Because earthquake rupture occurs at high strain rates, we assume that the steady-state effective temperature for dynamic fault slip is always in the rate-dependent regime. This indicates a maximum effective temperature of the form

$$\hat{\chi}(\dot{\gamma}) = \frac{\chi_w}{\log\left(\frac{q_0}{t_0 \dot{\gamma}}\right)}. \quad (2.12)$$

The parameter  $q_0$  determines the dimensionless strain rate at which the effective temperature diverges. At strain rates higher than  $q_0/t_0$ , the deformation is no longer accommodated as local STZs and instead as amorphous flow. The value of  $q_0 = 0.08$  that we use is deduced from molecular dynamics simulations [28]. Because the time scale for STZ rearrangement is very fast, our value of  $q_0$  corresponds to a strain rate larger than the strain rate expected during seismic slip. This means that the constitutive equations are valid at the strain rates in our simulations. Low strain rates are important for the deformation of glassy materials, and so we include the part of the curve where the effective temperature is independent of the strain rate when studying these materials in Chapter 6.

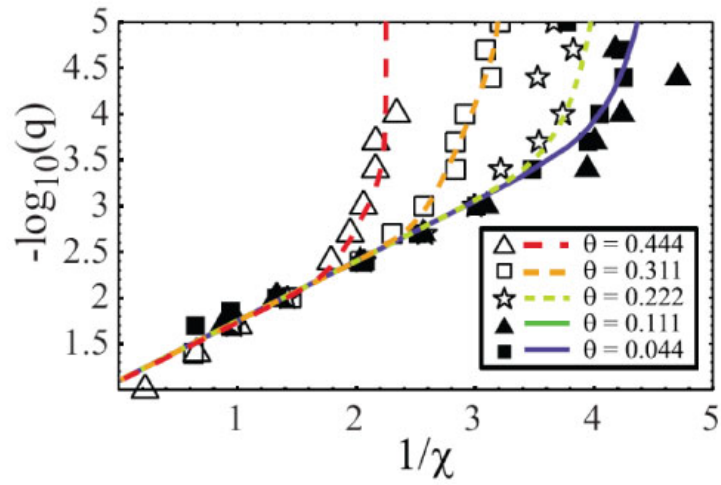


Figure 2.1: Plot of the negative logarithm of the non-dimensional strain rate  $q = t_0\dot{\gamma}$  versus the inverse effective temperature. The different colored curves correspond to varying thermal temperature in the simulation data. There are two important regimes: the linear rate-dependent portion of the curve, which occurs at high strain rates, and the glassy portion of the curve, where the effective temperature is independent of the strain rate. Earthquake rupture occurs at high strain rates, so we assume that  $\hat{\chi}$  is in the linear regime during our dynamic earthquake simulations.

## CHAPTER 2. STZ FRICTION LAW

The parameter  $\chi_w$ , which is the slope of the curve in Figure 2.1, is a very important quantity in the STZ Law. If this quantity is greater than unity, then the steady-state shear stress increases as the strain rate increases. Materials with  $\chi_w > 1$  are rate strengthening. If the slope is instead less than unity, the steady-state shear stress decreases as the strain rate increases. These rate weakening materials exhibit different frictional dynamics from rate strengthening materials. Rate weakening friction is essential for unstable earthquake rupture propagation, and so we dedicate most of this dissertation to studying the STZ model with rate weakening parameters. However, there are many systems that exhibit rate strengthening behavior, and we discuss these materials in Chapter 6.

Diffusion of effective temperature is observed in simulations [62], and only occurs if the material is being deformed. This indicates that the time scale for diffusion is determined by the inverse strain rate. The form of the diffusion term here assumes that the effective temperature flux in the  $z$ -direction at a given point is  $\dot{\gamma}D\partial\chi/\partial z$ . The length scale for diffusion,  $\sqrt{D}$ , is determined by the particles in the material. For a granular material, this length scale is related to the size of the grains. For a glass, this length scale is determined by the interparticle potential. The width of shear bands in amorphous materials is similar to this length scale  $\sqrt{D}$ , but the actual width is set by a balance between dissipation, relaxation, and diffusion and involves additional parameters.

The healing term allows for time-dependent restrengthening on the fault, and relaxes the effective temperature towards the minimum value  $\chi_0$ . The form of this term results in logarithmic strength recovery with time, as observed in laboratory experiments [63]. We include this term because faults heal and restrengthen with time, and including time-dependent healing is important for determining when slip stops during a dynamic rupture.

## 2.4 The Free Volume Law

The STZ model has many more degrees of freedom than Dieterich-Ruina friction, due to the partial differential equation governing the effective temperature. However, in cases when the diffusion length scale is comparable to the total thickness of the material, the strain rate is the same throughout the material. In this case, the effective temperature partial differential equation reduces to an ordinary differential equation.

In this simplified version of the model, the state variable accounting for the history of friction is the free volume instead of the effective temperature [59]. Free volume and effective temperature are related quantities [62], as a less dense

CHAPTER 2. STZ FRICTION LAW

material is usually more disordered than a more tightly packed material. Because the quantities are closely related, we use  $\chi$  to represent both effective temperature and free volume.

The free volume is a dimensionless, intensive quantity that describes the density of the fault gouge. It is related to porosity, which is also dimensionless, intensive, and describes the gouge density. They differ because  $\chi = 0$  corresponds to the gouge arranged to have the smallest possible volume, also known as random close packing [64], which still has some pore space. Free volume is related to porosity  $\phi$  by  $\chi = \phi - \phi_0$ , so that when  $\chi = 0$  the porosity is equal to  $\phi_0$ , the porosity of the random close packing.

Free volume evolves dynamically as the gouge is sheared. We include terms for compaction, which is time-dependent, and dilation, which occurs at a rate proportional to the rate at which frictional energy is dissipated:

$$\frac{d\chi}{dt} = -R_c \exp(-\chi_c/\chi) + \alpha\tau V. \quad (2.13)$$

Note that this equation is very similar to Equation (2.11) with the diffusion term set to zero – the relaxation term is proportional to the same exponential factor, and both equations have a term proportional to the energy dissipation rate. The evolution of the free volume accounts for the history dependence of friction in the FV law. This dynamic equation can be converted to a porosity evolution equation (using  $\chi = \phi - \phi_0$ ), and is an alternative to the porosity evolution proposed in [65].

The free volume law also has a constitutive equation relating the shear stress, slip rate, and free volume that is very similar to Equation (2.10):

$$V = V_* \exp[-f_* - (\chi_s + \chi_h)/\chi] (1 - m_0) \sinh(\tau/\sigma_d). \quad (2.14)$$

The FV law allows for solutions that are jammed ( $V = 0$ ) and slipping ( $V > 0$ ). The two different solutions are incorporated using the variable  $m_0$ . The values that  $m_0$  takes depend on whether the stress is above or below the minimum stress needed to flip an STZ,  $\tau_0 \exp(\chi_h/\chi)$ :

$$m_0 = \begin{cases} 1, & [\tau \leq \tau_0 \exp(\chi_h/\chi)]; \\ \frac{\tau_0}{\tau} \exp(\chi_h/\chi), & [\tau > \tau_0 \exp(\chi_h/\chi)]. \end{cases} \quad (2.15)$$

The parameters in the FV law include the characteristic slip rate  $V_*$ , the STZ activation energy scaled by the thermal energy  $f_*$ , the characteristic free volume for shearing  $\chi_s$ , the characteristic free volume for STZ creation  $\chi_h$ , the STZ activation stress  $\sigma_d$ , the compaction rate  $R_c$ , the characteristic free volume for compaction

## CHAPTER 2. STZ FRICTION LAW

$\chi_c$ , the fraction of frictional dissipation that goes into dilating the fault gouge  $\alpha$ , and the STZ yield stress  $\tau_0$ . The three characteristic free volumes are distinct quantities, as each corresponds to a different rearrangement of the fault gouge. We also note that the STZ activation stress  $\sigma_d$ , also known as the direct effect stress in rock mechanics experiments, determines the instantaneous stress change due to a change in the slip rate. This stress is typically much smaller than the normal stress or the shear stress in laboratory experiments.

Figure 2.2 shows a plot of shear stress and free volume/porosity as a function of shear displacement for two different velocity steps. The first velocity step is from  $V = 10^{-6}$  m/s to  $V = 10^{-5}$  m/s, and the second velocity step is from  $V = 10^{-5}$  m/s to  $V = 10^{-4}$  m/s. When the velocity is suddenly increased, there is a transient increase in the shear stress, followed by evolution to a new sliding stress over a characteristic length scale. The evolution is similar to the Dieterich-Ruina friction law described in Section 1.2.4, though the FV law relates this frictional behavior to microscopic physics rather than simply fitting data. The stress decreases after each velocity step, which indicates that the parameters are velocity weakening, and because the stress change is the same for both velocity steps, the FV law incorporates logarithmic velocity dependence.

We discuss the FV law more extensively in Chapter 4, where we make careful comparisons between the FV law and other friction laws in dynamic earthquake rupture simulations.

## 2.5 Friction Dynamics

In this section, we look at the dynamics of friction when the STZ law is applied to a layer of fault gouge under shear. A schematic of the system is shown in Figure 2.3. A layer of gouge of width  $2w$  is sheared from the boundary at a constant driving rate  $V_0$ . We assume that the shear stress is constant within the layer. This is because the time scale for stress equilibration (the width of the gouge divided by the speed of sound) is much smaller than the time scale for effective temperature evolution (the inverse plastic strain rate). Due to this difference in time scales, the stress is always spatially uniform in the  $z$ -direction, which is the static solution to the continuum momentum conservation equation in this geometry. This means that stress in the material evolves according to

$$\frac{d\tau}{dt} = \frac{\mu}{w} \left( V_0 - \int_0^w \dot{\gamma} dz \right). \quad (2.16)$$

Driving the system causes the stress to increase at a rate determined by the shear modulus  $\mu$ , while plastic strain decreases the shear stress. Note that because the

CHAPTER 2. STZ FRICTION LAW

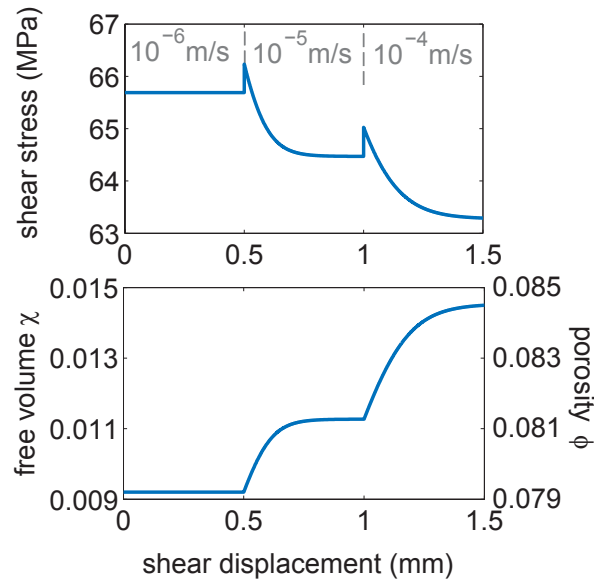


Figure 2.2: Dynamic evolution of the stress and free volume/porosity during two simulated velocity step experiments with the FV law. The first velocity step from  $V = 10^{-6}$  m/s to  $V = 10^{-5}$  m/s occurs at 0.5 mm, and the second velocity step from  $V = 10^{-5}$  m/s to  $V = 10^{-4}$  m/s occurs at 1 mm. The transient changes in stress are the same for both velocity steps, confirming the logarithmic velocity dependence of the FV law. The change in porosity is small compared to the total porosity, indicating that the change in the sheared layer thickness is small compared to the overall thickness. The porosity evolution uses  $\phi_0 = 0.07$  to convert from free volume.

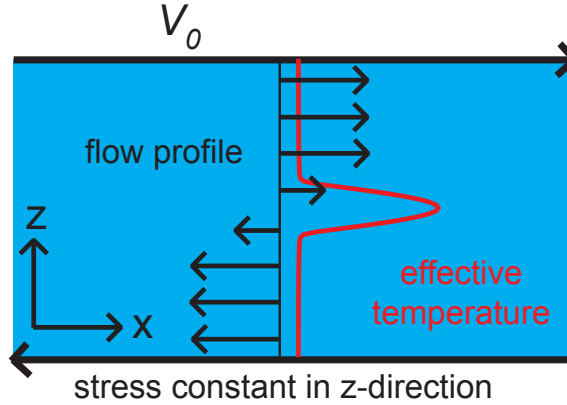


Figure 2.3: Diagram illustrating a layer of fault gouge driven at its boundary at a constant velocity  $V_0$ . We resolve the effective temperature dynamics as a function of position across the thickness of the gouge. This is illustrated by the red curve, which shows the effective temperature as a function of position in the gouge. Because the effective temperature evolves in space and time, the STZ model captures the dynamic evolution of the strain rate in the material, and the flow profile in the gouge, which is shown in black in the illustration. Stress is assumed to evolve rapidly compared to the effective temperature, and is always spatially homogeneous.

stress is constant across the width of the gouge, any localization of strain is due to spatial variations in the effective temperature (i.e. the configurational disorder in the gouge). Shear bands form because the disorder in the material becomes heterogeneous, and not because of spatial variations in the shear stress.

The equations for stress evolution (Equation (2.16)) and effective temperature evolution (Equation (2.11)) are integrated numerically to model the dynamics of friction in the layer. We use  $V_0 = 1$  m/s,  $w = 0.1$  m,  $\mu = 32$  GPa. At the start of integration, the stress is set to  $\tau(t = 0) = 50$  MPa. We solve for the effective temperature on a spatial grid with  $n_z = 51$  points in the  $z$ -direction, which resolves the dynamic evolution of the plastic strain rate within the fault gouge. We solve for the effective temperature in only half of the gouge, as the effective temperature is symmetric about  $z = 0$ . The spatial derivatives of the effective temperature are split into two terms and are approximated by second order central finite differences, and time integration is performed using a linearly implicit trapezoidal method with an adaptive time step. We use no conduction boundary conditions for the effective temperature at the boundaries of the gouge

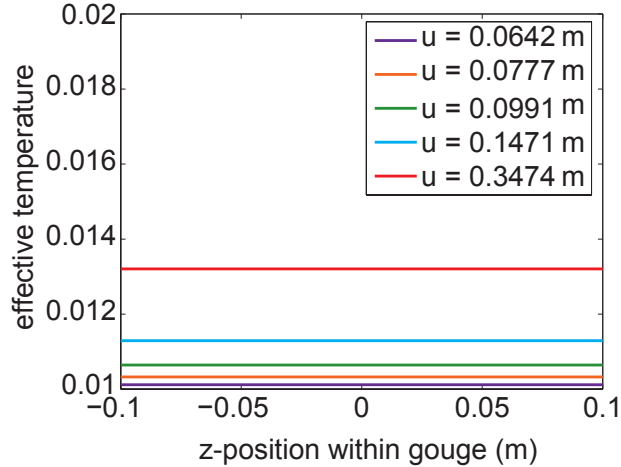


Figure 2.4: Effective temperature as a function of position at several different values of the shear displacement  $u$  for spatially uniform initial conditions. The diffusion term is zero, and by symmetry the effective temperature remains spatially homogeneous as the gouge is sheared.

layer.

The effective temperature dynamically evolves in the STZ model, which leads to a dynamic evolution of the plastic strain rate in the material. We consider two different types of initial conditions: spatially uniform in the  $z$ -direction, and the spatially uniform initial conditions plus a small perturbation. For the spatially uniform case, the initial effective temperature that we use is  $\chi(t = 0) = 0.009$ . If the initial effective temperature is spatially homogeneous, then by symmetry the strain rate is uniform and the subsequent plastic deformation is spatially uniform in the  $z$ -direction (Figure 2.4). In this case, the PDE for the effective temperature reduces to an ODE because the diffusion term is zero. Frictional behavior for homogeneous initial conditions is similar to that of the Dieterich-Ruina laboratory-based friction laws that are commonly used in earthquake modeling, which is discussed further in 4.

However, perfectly homogeneous initial conditions are not physically realistic. A spatially uniform initial effective temperature is extremely unlikely, and we approximate real initial conditions by adding a small perturbation (of the form  $\delta\chi \cdot \text{sech}(z/\delta w)$ , with  $\delta\chi = 10^{-10}$  and  $\delta w = w/250$ ). A single perturbation is sufficient to approximate heterogeneous initial conditions because with rate weakening parameters, we find that a single shear band forms at the point with the largest

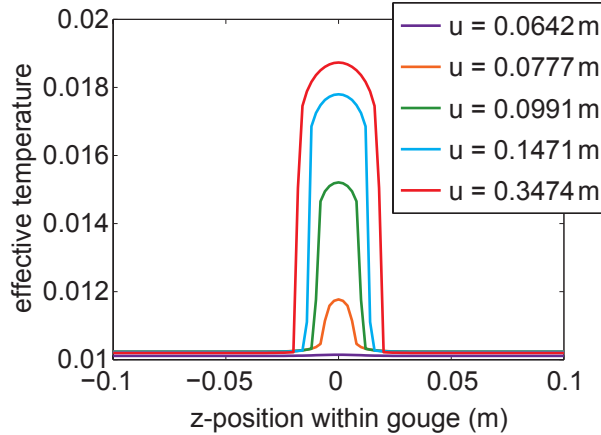


Figure 2.5: Plot of effective temperature as a function of  $z$ -position at several different values of the shear displacement  $u$  for the same spatially uniform initial conditions in Figure 2.4 plus a small perturbation described in the main text. As the gouge is sheared, the perturbation amplifies and grows into a shear band. The effective temperature grows much more rapidly with shear displacement when a shear band forms than when deformation is spatially uniform.

initial effective temperature regardless of the choice of heterogeneous initial conditions. When the initial effective temperature is perturbed, the diffusion term is no longer zero. We use a diffusion constant  $D = 0.0001 \text{ m}^2$  when numerically integrating the STZ equations with the perturbed initial effective temperature.

Figure 2.5 shows the effective temperature dynamics with a small perturbation added to the initial effective temperature. The perturbation spontaneously grows as the gouge is sheared and a narrow shear band dynamically forms. The unstable growth of the perturbation is due to a feedback in the effective temperature evolution law. Any spatial point with an elevated effective temperature also has a larger strain rate. The energy dissipation term in the effective temperature governing equation (Equation (2.11)) is proportional to the strain rate, so the effective temperature at a point with an elevated effective temperature grows more rapidly than others. This feeds back into the dissipation term, and leads to strain localization and the formation of a shear band.

The prediction that a perturbation to the initial effective temperature results in localization of strain can be confirmed through a linear stability analysis. Manning *et al.* [66] found that steady sliding was unstable if  $\chi_w < 1$ , which is precisely the conditions for steady-state rate weakening. This indicates that if the friction

## CHAPTER 2. STZ FRICTION LAW

law weakens with strain rate, any perturbation results in localized strain. Manning *et al.* also determined that shear bands can form even if the friction law is rate strengthening due to transient effects. While we focus on rate weakening parameters in this study, the prediction that rate strengthening materials can form shear bands has implications for many geophysical systems.

We show a plot of stress as a function of shear displacement for the two different sets of initial conditions in Figure 2.6. The curve for spatially uniform initial conditions is labeled “homogeneous,” and the curve for perturbed initial conditions is labeled “localized.” The curves are identical for shear displacements less than 0.1 m, at which point the shear band forms for the perturbed initial conditions. Once the shear band forms, the stress drops rapidly and the sliding friction is reduced. This indicates that localization is a mechanism for dynamic weakening. The strain rate is locally higher in the shear band, and the friction law weakens with strain rate, so the shear stress while sliding with a shear band is lower than for the case without a shear band.

The difference in the macroscopic stress shows that strain localization has a significant impact on the frictional properties of fault gouge. This affects larger scale phenomena at the interface scale such as stick-slip motion, which we examine in Chapter 3, and fault scale dynamics, which we study in Chapter 5.

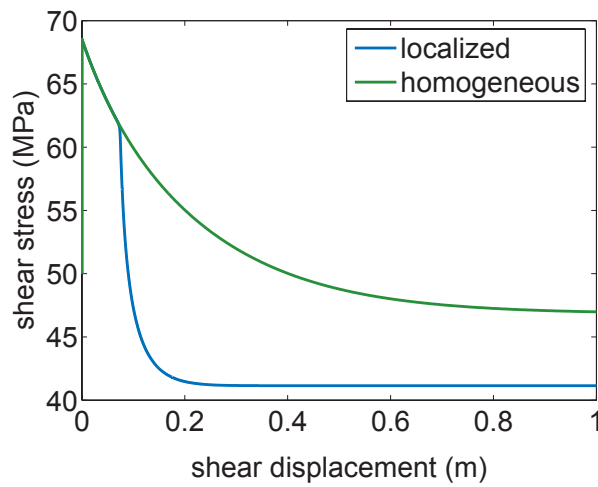


Figure 2.6: Plots of stress as a function of shear displacement for the plots in Figures 2.4 and 2.5. “Homogeneous” indicates that the initial effective temperature is spatially uniform, and the effective temperature for this curve is illustrated in Figure 2.4. “Localized” indicates that a small perturbation is added to the spatially uniform initial effective temperature; a shear band forms in this case. The effective temperature for the “localized” curve is shown in Figure 2.5. The formation of a shear band produces different macroscopic material behavior. The shear stress drops more rapidly with shear displacement for “localized” shear, and the steady sliding friction is significantly lower than the “homogeneous” case.

# Chapter 3

## Stick-Slip Instabilities

STZ Theory provides a continuum description of the grain scale physics of amorphous materials. For the remainder of the dissertation, we explore the consequences of the grain scale physics in STZ theory at larger scales. Here, we use the STZ model to study the dynamics of friction at the interface scale. Laboratory experiments probe the frictional properties of amorphous materials at this scale, and find that frictional slip often occurs through repeated cycles of stick-slip instead of steady sliding. In this chapter, we solve the STZ equations coupled to a spring slider, and examine the impact of strain localization on stick-slip instabilities.

### 3.1 Stick-Slip Instabilities

Dense amorphous materials include a wide range of systems, including granular materials, glassy materials, colloids, emulsions, and possibly even biological tissue. These materials often serve as lubricants for sheared interfaces, ranging in scale from atomically thin films to earthquake faults. While they differ vastly in scale, each is made up of a collection of smaller particles – the thin film contains a few layers of molecules, while the earthquake fault is filled with crushed grains of rock. Both the interfacial material and the large scale system as a whole can exhibit rich and complex dynamics. Most studies of these systems focus on the small scale physics in the material or the large scale dynamics of friction. In this dissertation, we bridge the two approaches using a constitutive law derived from small scale physics to investigate instabilities in both the deformation in the interfacial layer and the macroscopic friction.

Laboratory experiments show that granular materials [67], fault rocks [68, 69, 70], and thin films [71, 72, 73, 74] exhibit similar frictional dynamics, including

### CHAPTER 3. STICK-SLIP INSTABILITIES

a yield stress, hysteresis, rate dependent frictional resistance, and stick-slip. In this study, we focus on stick-slip instabilities, which are responsible for earthquake slip on seismic faults, noise from automobile brakes and tires, music from a violin, and excessive wear on frictional interfaces in machinery. Modeling the dynamics of friction in these materials is a challenging problem, as models must resolve the microscopic physics of deformation and simultaneously remain tractable for capturing the large scale behavior.

Experimental observations of friction are sometimes directly incorporated into phenomenological friction laws, such as the Stribeck curve [9] and the Dieterich-Ruina rate and state dependent friction laws [10, 11]. These fits to data capture many important features of experiments, but to date have not been derived from microscopic physics and do not resolve internal dynamic instabilities within the interfacial layer. Molecular dynamics simulations have provided extensive information about microscopic deformation and flow, but only for limited numbers of particles and a narrow range of time scales. Stick-slip motion has been explored in the context of constitutive models [75, 76, 77, 58] and molecular dynamics simulations [78, 79].

In this dissertation, we use a physics-based constitutive model that combines insights from atomistic simulations with the tractability of a constitutive law to connect macroscopic friction dynamics to the small scale physics of deformation. Our friction model is based on the theory of Shear Transformation Zones (STZs) [24, 25]. This continuum approach incorporates features from molecular dynamics simulations and fundamental constraints from nonequilibrium statistical physics and has been applied to a wide variety of materials [58, 61, 56]. The STZ constitutive model provides physical insight into plastic deformation, but is tractable for studying larger scale sheared interfaces. Additionally, STZ Theory has sufficient resolution of the microscopic scale to capture shear band instabilities and the spontaneous localization of strain [80, 57, 66]. When a shear band forms, deformation localizes to a region that is much narrower than the thickness of the material. Localization plays an important role in the frictional properties of bulk metallic glasses [31], granular materials [81], and bubble rafts [82].

In this study, we determine the effect of the microscopic physics of strain localization on the dynamics of stick-slip. We perform a linear stability analysis with the STZ equations to quantitatively determine how small-scale localization impacts the large scale frictional behavior. We compare localized strain, where a shear band dynamically forms, to homogeneous deformation, where no shear band forms and the strain rate is spatially uniform across the interfacial layer. We find that localization alters the parameter range where stick-slip occurs, thus demonstrating that the small scale physics plays an important role in the large

scale dynamics of friction.

We begin with a discussion of the physics behind the STZ model and the block slider equations in Section 3.2. In Section 3.3, we present the results of our stability analysis and our numerical studies with the STZ model. Section 3.4 concludes with a discussion of the implications of our work for friction and deformation in amorphous materials.

## 3.2 Model Equations

### 3.2.1 Block Slider Equations

We consider a spring slider with negligible mass (i.e. overdamped). The spring is pulled at a constant velocity  $V_0$ . The slider is illustrated on the left in Figure 3.1. The sheared interface is filled with an amorphous material. The material has a finite thickness of  $2w$  in the  $z$ -direction, and is much larger and translationally invariant in the other spatial directions, reducing the spatial dependence to  $z$  only. We also assume that the material is symmetric about  $z = 0$ , and therefore we only model the material for  $0 \leq z \leq w$ . A close-up of the amorphous material (center in Figure 3.1) shows that the shear strain can be heterogeneous within the material layer.

To explore the implications of microscopic strain localization on macroscopic friction, we couple the STZ equations (Equations (2.1) and (2.11)) to a spring slider. A block is attached to a spring pulled at a constant rate, and the block motion causes shear deformation in the amorphous material (left in Figure 3.1). For simplicity we ignore inertial effects. Experimental data often exhibits stick-slip motion in overdamped regimes [83], where the block oscillation time is much smaller than the duration of a stick-slip event. In this regime the frictional time scales are more important for the block dynamics than inertial effects. Because we are in an overdamped regime, the friction force balances the spring force. Therefore, we only require a dynamic equation for the frictional shear stress  $\tau$  in the amorphous material to complete the system of equations describing the STZ block slider model. Here  $\tau$  is taken to be constant in the  $z$ -direction. This follows from our assumption that the stress equilibration time scale is much faster than the time scales in the STZ friction law; the static solution to the momentum conservation equations in this geometry is a spatially uniform shear stress.

Stress in the material evolves due to elastic and plastic deformation. The spring of stiffness  $k$  is pulled at a constant rate  $V_0$ , which increases the shear stress by extending the spring. Meanwhile, plastic deformation occurs in the

CHAPTER 3. STICK-SLIP INSTABILITIES

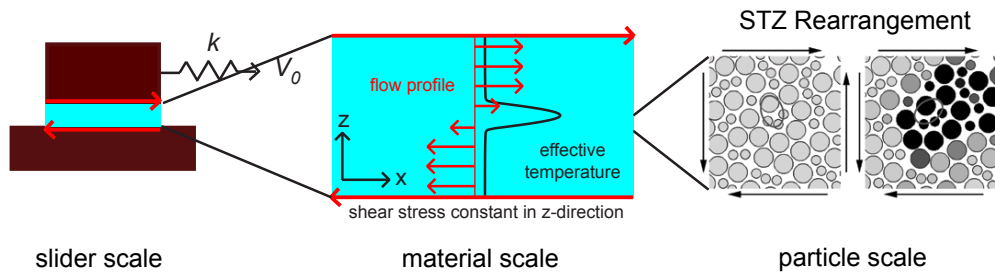


Figure 3.1: Illustration of the spring slider modeled with STZ Theory. (left) A block of negligible mass is pulled by a spring of stiffness  $k$  at constant velocity  $V_0$ . An amorphous material lubricates the sheared interface. (center) A close-up of the amorphous material indicates that we resolve the dynamic evolution of strain inside the material. In STZ Theory, the microscopic physics is captured through the evolution of an effective temperature, which is heterogeneous within the material. Our model accounts for the effect of strain localization on the motion of the block. (right) Close-up of an STZ reversal at the particle scale. As the material is sheared, an ellipse drawn through the particles switches from one orientation to the other. The dark particles on the right indicate where plastic deformation has occurred in the material. STZ image taken from Falk and Langer [24] (Reprinted with permission. Copyright 1998 by the American Physical Society. <http://link.aps.org/abstract/PRE/v57/p7192>).

## CHAPTER 3. STICK-SLIP INSTABILITIES

amorphous solid and causes the material to soften. Therefore, the shear stress  $\tau$  evolves according to

$$\dot{\tau} = k \left( V_0 - \int_0^w \dot{\gamma} dz \right). \quad (3.1)$$

Here, dots represent a time derivative. The first term on the right hand side represents elastic loading from the spring, and the second term represents material softening at a rate determined by the spatial integral of the plastic strain rate  $\dot{\gamma}$ . Because the system is overdamped, the spatial integral of the plastic strain rate over the entire material width is also the velocity of the slider block. The plastic strain rate is given by the STZ equation (Equation (2.1)), and is a function of the stress and the effective temperature.

### 3.2.2 Time Scales

The block slider equation (Equation (3.1)), along with the STZ equations (Equations (2.1) and (2.11)), involve a number of different time scales. The fastest among these is the STZ rearrangement time  $t_0$ . An estimate for  $t_0$  is a molecular vibrational time scale for a glassy material, or a characteristic particle diameter divided by the speed of sound in a granular material. These time scales are much faster than all others in the problem, and rearrangements are taken to be instantaneous in the STZ model.

The time scale for stress equilibration in the material is of the order of the thickness of the layer divided by the speed of sound. Note that since the layer contains many particles, this is certainly much slower than an individual STZ rearrangement. This time scale is also taken to be instantaneous in the model, which is implicit in Equation (3.1). For the theory to be applicable, all other processes must be slower than stress equilibration.

The time scale for effective temperature evolution is the inverse plastic strain rate. This describes both energy dissipation and diffusion and it must be slower than the stress equilibration time. Large strain rates tend to occur for large driving rates  $V_0$ , and also for stick-slip motion when the spring is very compliant. This restricts the range of driving rates as we numerically integrate the equations.

Because we assume that the slider is overdamped, we ignore the inertia of the block. This amounts to taking the time scale for oscillations of the spring slider to be much faster than the inverse plastic strain rate. The duration of a stick-slip event is thus much longer than the natural oscillation period of the unencumbered block and spring, which means that the frictional time scale dictates the dynamics of stick-slip. Stick-slip can also occur in an underdamped regime with a larger block mass, but we do not consider that limit in our analysis.

### CHAPTER 3. STICK-SLIP INSTABILITIES

Table 3.1: Dimensionless parameters for the block slider equations.

| Parameter             | Description  |
|-----------------------|--|
| $\epsilon = 10$       | Strain accumulated per STZ reversal                  |
| $\sigma_d = 1$        | STZ activation stress                                |
| $f_0 = 11.5$          | STZ activation energy                                |
| $c_0 = 1$             | Effective temperature specific heat                  |
| $D = 0.1$             | Squared effective temperature diffusion length scale |
| $\chi_w = 0.8$        | Effective temperature activation energy              |
| $q_0 = 1$             | Strain rate at which STZ Theory breaks down          |
| $V_0 = \text{varies}$ | Driving rate   |
| $k = \text{varies}$   | spring constant                                      |

#### 3.2.3 Non-Dimensional Equations

We non-dimensionalize the equations using the following parameters: scale all times by the STZ rearrangement time  $t_0$ , scale all lengths by the material width  $w$ , and scale all stresses by the STZ yield stress  $\tau_y$ . The parameters can thus be redefined as follows: stress  $\tau' = \tau/\tau_y$ , strain rate  $\dot{\gamma}' = t_0\dot{\gamma}$ , driving rate  $V_0' = V_0t_0/w$ , STZ activation stress  $\sigma_d' = \sigma_d/\tau_y$ , diffusion length scale  $D' = D/w^2$ , and spring constant  $k' = kw/\tau_y$ . The non-dimensional equations are (dropping all primes on variables)

$$\dot{\tau} = k \left( V_0 - \int_0^1 \dot{\gamma} dz \right), \quad (3.2)$$

$$\dot{\chi} = \frac{\dot{\gamma}\tau}{c_0} \left( 1 - \frac{\chi}{\hat{\chi}(\dot{\gamma})} \right) + \frac{\partial}{\partial z} \left( D\dot{\gamma} \frac{\partial \chi}{\partial z} \right). \quad (3.3)$$

where  $\hat{\chi}(\dot{\gamma}) = \chi_w / \log(q_0/\dot{\gamma})$  and  $\dot{\gamma} = f(\tau) \exp(-1/\chi)$ . The stress factor is given by  $f(\tau) = 2\epsilon \exp(-f_0) \cosh(\tau/\sigma_d)(1 - 1/\tau)$ .

The non-dimensional parameters that we use in numerical integration of the block slider model are given in Table 3.1. We keep all parameters constant except the driving rate and spring stiffness, which we vary to explore the parameter ranges that lead to stick-slip motion.

### 3.2.4 Small Scale Effects on Friction in STZ Theory

In STZ Theory, the dynamics of friction is controlled by the evolution of the effective temperature. The effective temperature is derived from the underlying statistical physics of dense, disordered solids and STZ Theory connects macroscopic frictional behavior to the evolution of the effective temperature. This includes resolving the spontaneous localization of strain. Other friction laws that do not resolve the internal dynamics of the interfacial material are *a priori* incapable of resolving the dynamical shear band instability.

Manning *et al.* [66] showed that a key parameter that connects the microscopic physics to the macroscopic dynamics in STZ Theory is the effective temperature activation barrier  $\chi_w$ . Manning *et al.* performed a linear stability analysis of the STZ equations, and showed that  $\chi_w$  determined the stability of deformation with a spatially uniform effective temperature. If this activation barrier is less than unity, homogeneous deformation is linearly unstable ( $\chi_w < 1$ ). This is precisely the conditions for rate weakening friction. Rate weakening refers to the strain rate dependence of the steady-state shear stress – as the strain rate increases, the steady-state stress decreases. Therefore, rate weakening materials always form shear bands given any heterogeneity in the initial effective temperature, as steady sliding is linearly unstable. If the activation barrier is less than unity, then steady sliding is stable. This corresponds to the parameter range for rate strengthening friction, where the shear stress increases as the strain rate increases. However, shear bands can still form if  $\chi_w > 1$  due to transient effects [80, 66].

Although shear bands form for both rate weakening and rate strengthening materials, we focus on rate weakening materials in this study. Previous studies with Dieterich-Ruina friction [75] and STZ Theory without strain localization [58] showed that rate weakening is required for steady sliding to be unstable in a single degree of freedom elastic system. When shear band formation is included, we also find that steady sliding is unstable only if friction is rate weakening, which we show in the next section.

## 3.3 Stick-Slip Dynamics

In this section, we explore the dynamics of the block slider model with STZ Theory. We investigate the effects of shear band formation on the stability of frictional sliding, and generate a phase diagram that distinguishes between parameters that produce stick-slip versus steady sliding with and without shear bands. We also identify more exotic stick-slip cycles, and connect the underlying microscopic physics to the observed complex dynamics. This involves both

## CHAPTER 3. STICK-SLIP INSTABILITIES

analytical and numerical studies with the STZ equations.

For fixed material parameters, the type of motion depends on the driving rate (the speed at which the spring is loaded), and the stiffness of the spring. If we fix the spring stiffness, large driving velocities result in steady sliding of the block. The slider moves at the same velocity as the load point (the end of the spring that is pulled at a constant velocity), and the shear stress is at its steady-state value. At slower driving rates, the block undergoes repeated stick-slip cycles. If we instead fix the driving velocity, stiff springs produce steady sliding and compliant springs produce stick-slip. The spring stiffness and the driving rate are both important for determining the slider dynamics, as observed in experiments [84].

In laboratory experiments, the transition from steady sliding to stick-slip is usually investigated by fixing the spring stiffness and varying the driving velocity, as it is much easier to change the driving velocity in an experiment. In STZ Theory, it is more straightforward to calculate the stiffness at which sliding becomes unstable as a function of velocity, because the velocity as a function of stiffness cannot be obtained in closed form. This is due to the nonlinear dependence of the stress and effective temperature on the driving rate. Ultimately, both approaches are equivalent as each determines the boundary in  $(V_0, k)$  space separating stick-slip and steady sliding. Because we solve for the stiffness as a function of velocity, we refer to the spring stiffness where the motion transitions from stable sliding to stick-slip as the critical stiffness  $k_{crit}(V_0)$ . Our analytical results focus on determining the critical stiffness as a function of the STZ parameters, allowing us to connect stick-slip to the microscopic physics of deformation.

An example of stick-slip with the STZ law is illustrated in Figure 3.2, which shows shear stress as a function of the slider velocity for one cycle of the motion. The slider velocity is plotted on a logarithmic scale. The vertical line indicates the velocity at which the spring is pulled  $V_0$ . At the left, the velocity is much smaller than the driving velocity  $V_0$  and the slider “sticks” (i.e. creeps at a small velocity). As the spring is loaded, the shear stress increases until the spring overcomes the frictional resistance. The block begins to slip much more rapidly than the rate at which the spring is pulled. The shear stress drops, and the block overshoots the load point, which causes it to “stick” again, and the cycle repeats.

Stick-slip motion occurs when steady frictional sliding is unstable, as shown in Figure 3.3. The plot shows the frictional stress as a function of the load point displacement. The slider begins sliding steadily, but the block motion transitions to repeated stick-slip cycles. The inset in Figure 3.3(b) shows that stick-slip motion involves elastic loading by the spring over a large load point displacement during the “stick” phase. The stress drops very rapidly during the “slip” phase, indicating a large slider velocity.

CHAPTER 3. STICK-SLIP INSTABILITIES

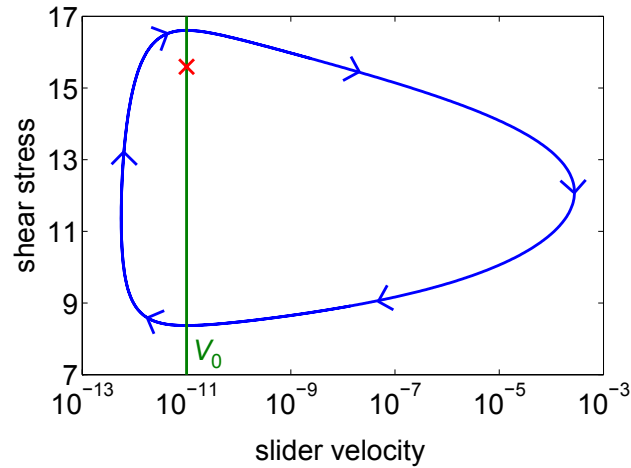


Figure 3.2: Stress and slider velocity evolution during periodic stick-slip motion with the STZ law. Instead of sliding steadily, which would be a single point on this diagram, the block cycles through successive “stick” and “slip” cycles. The “x” on the diagram indicates the steady sliding solution. At the far left, the block is moving much slower than the rate at which the spring is pulled (the vertical line), and the shear stress increases as the spring is extended. At the top, the spring force is large enough to initiate slip and the block slips rapidly relative to  $V_0$  until the spring. The cycle repeats as the stress build up again during the stick phase. Note that the slider velocity is not zero during a “stick” cycle – the block creeps much slower than the rate at which the spring is pulled, but never truly stops.

CHAPTER 3. STICK-SLIP INSTABILITIES

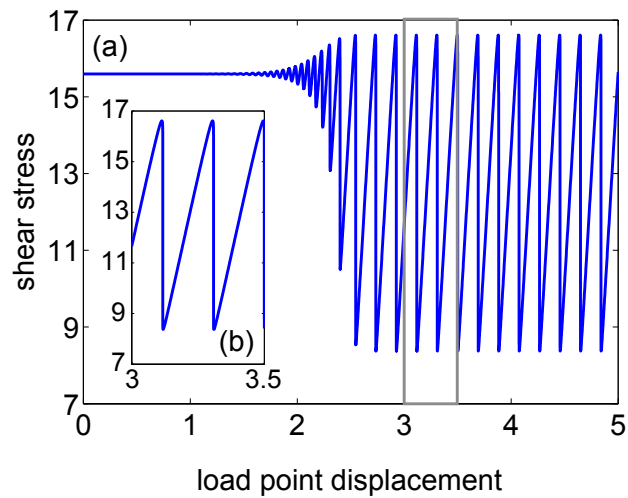


Figure 3.3: Shear stress as a function of load point displacement for stick-slip motion. The load point displacement refers to the displacement of the end of the spring that is pulled at a constant rate. (a) The block starts out sliding steadily, but steady sliding is unstable and the motion evolves into stick-slip cycles. (b) The inset shows a close up of stable, periodic stick-slip cycle, shown in Figure 3.2, contained in the gray box of the main Figure. The stress increases during the “stick” phase due to the elastic loading of the spring, while the rapid slip of the block suddenly drops the stress during the “slip” phase.

### 3.3.1 Analytical Results

Stick-slip instabilities occur when the steady sliding solution to the block slider equations becomes unstable to perturbations. The system of equations describing the block motion is

$$\dot{\tau} = k \left( V_0 - f(\tau) \int_0^1 \exp(-1/\chi) dz \right); \quad (3.4)$$

$$\dot{\chi} = \frac{f(\tau) \exp(-1/\chi) \tau}{c_0} \left[ 1 - \frac{\chi}{\hat{\chi}(\dot{\gamma})} \right] + Df(\tau) \frac{\partial}{\partial z} \left[ \exp(-1/\chi) \frac{\partial \chi}{\partial z} \right]. \quad (3.5)$$

These are the same equations as Equations (3.2)-(3.3), with the strain rate written out explicitly in terms of the stress and effective temperature. We analytically determine the critical stiffness using a linear stability analysis of the STZ equations. In Section 3.3.2, we confirm the results by numerically integrating the block slider model.

Linear stability analysis determines if perturbations to the stress and effective temperature grow or decay in time. Mathematically, this involves finding the real part of the eigenvalues of the Jacobian. Negative real parts imply perturbations to the stress and effective temperature decay exponentially in time, and steady sliding is stable. Positive real parts imply steady sliding is unstable, and perturbations to the stress and effective temperature grow exponentially in time.

The analysis is straightforward, though the intermediate expressions in the calculation are fairly complicated. We calculate stability criteria for homogeneous deformation, where the strain rate is uniform throughout the material, and for localized deformation, where the strain rate is determined by the dynamic evolution of the effective temperature. The details of the stability analysis is presented in the two following sections.

#### Homogeneous Deformation

First, we perform the stability analysis with the assumption that the effective temperature is spatially homogeneous. In this case, the diffusion term in the effective temperature equation is zero, and the spatial integral in Equation (3.4) is  $\int \exp(-1/\chi) dz = \exp(-1/\chi)$ . The dynamical system for homogeneous deformation is

$$\dot{\tau} = k (V_0 - f(\tau) \exp(-1/\chi)); \quad (3.6)$$

$$\dot{\chi} = \frac{f(\tau) \exp(-1/\chi) \tau}{c_0} \left[ 1 - \frac{\chi}{\hat{\chi}(\dot{\gamma})} \right]. \quad (3.7)$$

CHAPTER 3. STICK-SLIP INSTABILITIES

The Jacobian of the STZ equations for homogeneous deformation is

$$J_{11} = \frac{\partial \dot{\tau}}{\partial \tau} = -k f'(\tau) \exp(-1/\chi); \quad (3.8)$$

$$J_{12} = \frac{\partial \dot{\tau}}{\partial \chi} = -\frac{k f(\tau) \exp(-1/\chi)}{\chi^2}; \quad (3.9)$$

$$J_{21} = \frac{\partial \dot{\chi}}{\partial \tau} = \frac{[f'(\tau) \tau + f(\tau)] \exp(-1/\chi)}{c_0} \left(1 - \frac{\chi}{\hat{\chi}}\right) + \frac{f(\tau) \exp(-1/\chi) \tau \chi}{c_0} \frac{\partial \hat{\chi}}{\hat{\chi}^2 \partial \tau}; \quad (3.10)$$

$$J_{22} = \frac{\partial \dot{\chi}}{\partial \chi} = \frac{f(\tau) \exp(-1/\chi) \tau}{c_0 \chi^2} \left(1 - \frac{\chi}{\hat{\chi}}\right) + \frac{f(\tau) \exp(-1/\chi) \tau}{c_0} \left(\frac{\chi}{\hat{\chi}^2} \frac{\partial \hat{\chi}}{\partial \chi} - \frac{1}{\hat{\chi}}\right). \quad (3.11)$$

The maximum effective temperature is a function of the strain rate, which means that  $\hat{\chi}$  depends on both the stress and the effective temperature. When evaluated at steady state ( $V_0 = f(\tau) \exp(-1/\chi)$  and  $\chi = \hat{\chi}$ ), this becomes

$$J_{11} = \frac{\partial \dot{\tau}}{\partial \tau} = -\frac{k f'(\tau) V_0}{f(\tau)}; \quad (3.12)$$

$$J_{12} = \frac{\partial \dot{\tau}}{\partial \chi} = -\frac{k V_0}{\chi^2}; \quad (3.13)$$

$$J_{21} = \frac{\partial \dot{\chi}}{\partial \tau} = \frac{V_0 \tau \hat{\chi} f'(\tau)}{c_0 \chi_w f(\tau)}; \quad (3.14)$$

$$J_{22} = \frac{\partial \dot{\chi}}{\partial \chi} = \frac{V_0 \tau}{c_0 \hat{\chi}} \left(\frac{1}{\chi_w} - 1\right); \quad (3.15)$$

since the derivatives of  $\hat{\chi}$  with respect to stress and effective temperature are

$$\frac{\partial \hat{\chi}}{\partial \tau} = \frac{\hat{\chi}^2 f'(\tau)}{\chi_w f(\tau)}; \quad (3.16)$$

$$\frac{\partial \hat{\chi}}{\partial \chi} = \frac{\hat{\chi}^2}{\chi^2 \chi_w}. \quad (3.17)$$

The real part of the eigenvalues is the trace of the Jacobian, as near the transition from stable sliding to unstable sliding, the eigenvalues are complex. Steady sliding is unstable if the trace of the Jacobian is greater than zero:

$$\text{Tr}(J) = \frac{\partial \dot{\tau}}{\partial \tau} + \frac{\partial \dot{\chi}}{\partial \chi} = -\frac{k V_0 f'(\tau)}{f(\tau)} + \frac{V_0 \tau}{c_0 \hat{\chi}} \left(\frac{1}{\chi_w} - 1\right) > 0. \quad (3.18)$$

### CHAPTER 3. STICK-SLIP INSTABILITIES

Equation (3.18) reveals that stability is determined by two competing effects. The first term in Equation (3.18) comes from the spring force. This term is always negative, as the spring force is always a restoring force that pushes the block towards equilibrium. The second term in Equation (3.18) comes from the energy dissipation term in the effective temperature evolution equation. This term is destabilizing only if  $\chi_w < 1$  (i.e. for rate weakening parameters).

#### Localized Deformation

We now determine the role of localization by performing a linear stability analysis on the full STZ equations (Equations (3.4)-(3.5)). This involves the same steps as the homogeneous case, but with the inclusion of the diffusion term in Equation (3.5) and the spatial integral in Equation (3.4). We study how perturbations to a steady shear band solution to the effective temperature equations grow in time. To simplify the analysis, we assume that the perturbations to the effective temperature are not a function of  $z$ . Spatially varying perturbations can be considered through an analysis of normal modes. However, it turns out that the zero wavenumber mode is the least stable (the diffusion term in Equation (3.5) results in the higher wavenumber modes being more stable), so nothing extra is gained with a perturbation that varies with  $z$ .

For localized deformation, the Jacobian of the system is:

$$J_{11} = \frac{\partial \dot{\tau}}{\partial \tau} = -k f'(\tau) \int_0^1 \exp(-1/\chi) dz; \quad (3.19)$$

$$J_{12} = \frac{\partial \dot{\tau}}{\partial \chi} = -k f(\tau) \int_0^1 \frac{\exp(-1/\chi)}{\chi^2} dz; \quad (3.20)$$

$$\begin{aligned} J_{21} = \frac{\partial \dot{\chi}}{\partial \tau} = & \frac{[f'(\tau) \tau + f(\tau)] \exp(-1/\chi)}{c_0} \left(1 - \frac{\chi}{\hat{\chi}}\right) \\ & + \frac{f(\tau) \exp(-1/\chi) \tau \chi}{c_0 \hat{\chi}^2} \frac{\partial \hat{\chi}}{\partial \tau} \\ & + D f'(\tau) \frac{\partial}{\partial z} \left[ \exp(-1/\chi) \frac{\partial \chi}{\partial z} \right]; \end{aligned} \quad (3.21)$$

$$\begin{aligned} J_{22} = \frac{\partial \dot{\chi}}{\partial \chi} = & \frac{f(\tau) \exp(-1/\chi) \tau}{c_0 \chi^2} \left(1 - \frac{\chi}{\hat{\chi}}\right) \\ & + \frac{f(\tau) \exp(-1/\chi) \tau}{c_0} \left( \frac{\chi}{\hat{\chi}^2} \frac{\partial \hat{\chi}}{\partial \chi} - \frac{1}{\hat{\chi}} \right) \\ & + D f(\tau) \frac{\partial}{\partial \chi} \left\{ \frac{\partial}{\partial z} \left[ \exp(-1/\chi) \frac{\partial \chi}{\partial z} \right] \right\}. \end{aligned} \quad (3.22)$$

CHAPTER 3. STICK-SLIP INSTABILITIES

Perturbations to the effective temperature are independent of  $z$ , so the  $\chi$  derivative in the diffusion term in  $J_{22}$  only acts on the  $\exp(-1/\chi)$  factor:

$$\begin{aligned} \frac{\partial}{\partial \chi} \left\{ \frac{\partial}{\partial z} \left[ \exp(-1/\chi) \frac{\partial \chi}{\partial z} \right] \right\} &= \frac{\partial}{\partial z} \left[ \frac{\exp(-1/\chi) \frac{\partial \chi}{\partial z}}{\chi^2} \right] \\ &= \frac{1}{\chi^2} \frac{\partial}{\partial z} \left[ \exp(-1/\chi) \frac{\partial \chi}{\partial z} \right] \\ &\quad - \frac{2 \exp(-1/\chi)}{\chi^3} \left( \frac{\partial \chi}{\partial z} \right)^2. \end{aligned} \quad (3.23)$$

When evaluated at steady-state, where  $V_0 = f(\tau) \int \exp(-1/\chi) dz$  and the diffusion and energy dissipation terms balance, the Jacobian becomes:

$$J_{11} = \frac{\partial \dot{\tau}}{\partial \tau} = -\frac{k f'(\tau) V_0}{f(\tau)}; \quad (3.24)$$

$$J_{12} = \frac{\partial \dot{\tau}}{\partial \chi} = -k f(\tau) \int_0^1 \frac{\exp(-1/\chi)}{\chi^2} dz; \quad (3.25)$$

$$\begin{aligned} J_{21} = \frac{\partial \dot{\chi}}{\partial \tau} &= \frac{f(\tau) \exp(-1/\chi)}{c_0} \left( 1 - \frac{\chi}{\hat{\chi}} \right) \\ &\quad + \frac{f(\tau) \exp(-1/\chi) \tau \hat{\chi} f'(\tau)}{c_0 \chi_w f(\tau)}; \end{aligned} \quad (3.26)$$

$$\begin{aligned} J_{22} = \frac{\partial \dot{\chi}}{\partial \chi} &= \frac{f(\tau) \exp(-1/\chi) \tau}{c_0 \hat{\chi}} \left( \frac{1}{\chi_w} - 1 \right) \\ &\quad - \frac{2D f(\tau) \exp(-1/\chi)}{\chi^3} \left( \frac{\partial \chi}{\partial z} \right)^2. \end{aligned} \quad (3.27)$$

As with homogeneous deformation, the eigenvalues turn out to be complex at steady state. The real part of the eigenvalues is the trace of the Jacobian. Therefore, if the trace of the Jacobian is greater than zero, steady sliding is unstable:

$$\text{Tr}(J) = \frac{\partial \dot{\tau}}{\partial \tau} + \frac{\partial \dot{\chi}}{\partial \chi} = -\frac{k V_0 f'(\tau)}{f(\tau)} + \frac{\dot{\gamma} \tau}{c_0 \hat{\chi}} \left( \frac{1}{\chi_w} - 1 \right) - 2D \frac{\dot{\gamma}}{\chi^3} \left( \frac{\partial \chi}{\partial z} \right)^2 > 0. \quad (3.28)$$

There are two important differences between this expression and the equivalent expression for homogeneous deformation (Equation (3.18)). First is the presence of the diffusion term, which is negative and therefore stabilizes the growth of perturbations. The other important difference is that the energy dissipation term (the second term in Equation (3.28)) depends on the strain rate rather than the

## CHAPTER 3. STICK-SLIP INSTABILITIES

average strain rate. This term is much larger when a shear band forms due to the elevated strain rate in the shear band. Ultimately this implies that stick-slip motion occurs for a larger spring stiffnesses when a shear bands forms.

### Stability Analysis Results

For both homogeneous and localized deformation, the stability criteria (Equations (3.18) and (3.28)) depend on several different terms. In both expressions, the first term comes from the spring force, which is always less than zero and is therefore always stabilizing. This term is identical for the two cases. The second term in both expressions results from energy dissipation in the amorphous material. This term can be greater than zero, and thus can be destabilizing. Note that for homogeneous deformation, the dissipation term is proportional to the driving rate  $V_0$ , while for localized deformation, it is proportional to the plastic strain rate  $\dot{\gamma}$ . The strain rate in a shear band is larger than the overall driving rate, so localization makes energy dissipation more destabilizing. For localized deformation, the third term comes from diffusion. This term is always negative, and is thus stabilizes steady sliding. The increase in the energy dissipation term is the larger effect, implying that localization results in stick-slip motion over a larger range of parameters. The stability criteria connects the microscopic physics of the effective temperature (the energy dissipation and diffusion terms) to the macroscopic frictional behavior (the stress term).

The critical stiffness is the stiffness at which the terms exactly cancel. For the homogeneous case this is simply

$$k_{crit,h}(V_0) = \frac{f(\tau)\tau(V_0)}{f'(\tau)c_0\hat{\chi}(V_0)} \left( \frac{1}{\chi_w} - 1 \right). \quad (3.29)$$

To determine the critical stiffness for localized deformation, we must quantitatively determine the effect of localization (i.e. determine the strain rate and effective temperature in the shear band). We cannot do this analytically, as the effective temperature governing equation is highly nonlinear. We instead estimate it by assuming that to a first approximation, the strain rate is constant inside a shear band of thickness  $a$ , and negligible outside the shear band. This means that the strain rate in the shear band is  $V_0/a$ , and the effective temperature inside the shear band is  $\hat{\chi}(V_0/a)$ . We also must estimate  $\partial\chi/\partial z$  to quantify the effect of diffusion. Because the strain rate is negligible outside the shear band,  $\hat{\chi}$  is not defined, so we instead use the value of the effective temperature with driving rate  $V_0$ ,  $\hat{\chi}(V_0)$ . Therefore, if we have an estimate of the shear band thickness  $a$ , we can

### CHAPTER 3. STICK-SLIP INSTABILITIES

easily calculate  $\dot{\gamma} = V_0/a$ ,  $\hat{\chi}(V_0/a)$ , and  $\partial\chi/\partial z = (\hat{\chi}(V_0/a) - \hat{\chi}(V_0))/a$ , and use these values to estimate the critical stiffness.

We estimate the shear band thickness  $a$  by assuming that dissipation and diffusion roughly balance in the shear band. Equating these terms gives:

$$\frac{\dot{\gamma}\tau}{c_0} \sim D\dot{\gamma}\frac{\chi}{a^2}. \quad (3.30)$$

The strain rate divides out, and solving for  $a$  yields

$$a \sim \sqrt{\frac{Dc_0\chi}{\tau}}. \quad (3.31)$$

This expression shows that  $a$  scales with the diffusion length  $\sqrt{D}$ , but also depends on the stress, the effective temperature, and the effective temperature specific heat. Therefore, given the driving rate, we determine the steady state shear stress and effective temperature, and use these values to predict  $a$ .

Tests of Equation (3.31) through numerical integration show that the scaling for each of the parameters is correct. However, direct use of Equation (3.31) underestimates  $a$ . This is because the energy dissipation term is smaller than the estimate of  $\dot{\gamma}\tau/c_0$ , as  $\chi$  is not completely negligible compared to  $\hat{\chi}$ . A better estimate can be obtained by numerically integrating the STZ equations once to determine a constant of proportionality. We use the half width of the shear band at half the maximum strain rate as our estimate of  $a$ . This criteria predicts that the shear band thickness is about 3.7 times larger than in Equation (3.31) for the parameters in Table 3.1. The value of the critical stiffness is not very sensitive to this proportionality factor. If the factor is changed to 3 or 4.5, the critical stiffness decreases by about 10% in both cases. Both cases result in a decreased critical stiffness because there are two competing localization effects, dissipation and diffusion. Increasing the proportionality factor changes the dissipation effect more than the diffusion effect, and decreasing the proportionality factor changes the diffusion effect more than the dissipation effect.

Therefore, the shear band thickness for the parameters in our simulations is

$$a = 3.7\sqrt{\frac{Dc_0\hat{\chi}(V_0)}{\tau}}, \quad (3.32)$$

and the critical stiffness for localized deformation is

$$k_{crit,l}(V_0) = \frac{f(\tau)\tau(V_0)}{af'(\tau)c_0\hat{\chi}(V_0/a)} \left( \frac{1}{\chi_w} - 1 \right) - \frac{2Df(\tau)(\hat{\chi}(V_0/a) - \hat{\chi}(V_0))^2}{(a\hat{\chi}(V_0/a))^3 f'(\tau)}. \quad (3.33)$$

## CHAPTER 3. STICK-SLIP INSTABILITIES

Equations (3.29) and (3.33) determine the boundaries for homogeneous and localized deformation in  $(k, V_0)$  space separating stick-slip and steady sliding. Above  $k_{crit}$ , steady sliding is stable, and below  $k_{crit}$ , stick-slip occurs. The expression for localized deformation differs from the homogeneous expression due to the diffusion term and the larger dissipation term. These changes have competing effects – diffusion stabilizes steady sliding, while dissipation promotes unstable sliding. The increase in the energy dissipation term has a larger effect, and the critical stiffness is larger for localized shear than for homogeneous deformation. In both cases, rate weakening is required for steady sliding to be unstable (if  $\chi_w > 1$ , then the critical stiffness would have to be negative, which is unphysical). The function  $f(\tau)$  is determined by the stress dependence of the rate switching factor. In the case of exponential stress dependence,  $f(\tau)/f'(\tau) \approx \sigma_d$ , and the critical stiffness is proportional to the steady sliding stress and inversely proportional to the effective temperature. Note that the stress and effective temperature are both functions of the driving velocity  $V_0$ , which means that the critical stiffness depends on  $V_0$  for both types of deformation. The stress decreases with increasing driving rate (since friction is rate weakening), and the effective temperature increases with the driving rate. This means that as the driving rate increases, the critical stiffness decreases, which is consistent with experiments [84]. This rate dependence is not captured by Dieterich-Ruina friction, which predicts that the critical stiffness is independent of the driving rate.

An important implication of our analysis is that localized deformation cannot be approximated by homogeneous deformation with a reduced material thickness. This is because the diffusion term in Equation (3.33) reduces the critical stiffness, an effect that the homogeneous model cannot incorporate. It is necessary to resolve the internal material instabilities in order to produce the correct macroscopic behavior.

### 3.3.2 Numerical Results

We confirm our analytic predictions for the dependence of the critical stiffness on the driving rate through numerical integration of the STZ equations. We perform numerical simulations to ensure that our estimate for the shear band thickness is accurate, and to explore the connection between the internal disorder characterized by the effective temperature and irregular stick-slip dynamics.

We integrate Equations (3.4)-(3.5) along with the constitutive law (Equation (2.1)). We first turn the partial differential equation into a system of ordinary differential equations. We approximate the spatial derivatives using central second order finite differences, with the diffusion term is split into two separate terms

### CHAPTER 3. STICK-SLIP INSTABILITIES

using the product rule. We write the spatial integral in Equation (3.4) as a numerical integral using the trapezoidal method. Once the STZ equations are written as a system of ordinary differential equations, we use a second order linearly implicit trapezoidal method to advance the system in time. Because stick-slip events involve longer periods of elastic loading followed by rapid failure, we use an adaptive time stepping method to efficiently resolve the slider motion.

We vary the scaled driving rate from  $V_0 = 10^{-12}$  to  $10^{-4}$ , and vary the scaled spring stiffness at each velocity to find where the transition from steady sliding to stick-slip occurs. The other parameters are given in Table 3.1. For each set of  $V_0$  and  $k$ , we start the block at steady sliding. If the stress and slider velocity do not remain constant, then steady sliding is unstable. Figure 3.3(a) illustrates an example of the stress evolution when steady sliding is unstable – the shear stress begins to oscillate, and the oscillations grow into stick-slip cycles.

We compare slider motion in cases involving dynamic formation of a shear band with deformation that is homogeneous. To obtain homogeneous deformation, we start the system with a spatially homogeneous effective temperature. In contrast, to form a shear band, a small perturbation of the form  $\delta\chi \operatorname{sech}(z/\delta z)$  is added to the initial effective temperature. We find that the values of  $\delta\chi$  and  $\delta z$  do not influence the limit cycle of stick-slip motion nor the final width or amplitude of the shear band. For simplicity, we use values of  $\delta\chi = 10^{-4}$  and  $\delta z = 0.1$  for all of our localized simulations.

Figure 3.4 shows the phase diagram in  $(V_0, k)$  space that results from our analytical and numerical studies. As expected, the critical stiffness decreases with the driving rate, and the critical stiffness for localized deformation is larger than that for homogeneous shear. The analytical expression for the critical stiffness with homogeneous shear matches extremely well with the numerical results. For localized deformation, our analysis yields a curve that is slightly below the curve obtained numerically. This discrepancy is due to the approximations we used to estimate the shear band width and the magnitude of the diffusion term. Changing the value of the correction factor in the prediction of the shear band thickness  $a$  (Equation (3.32)) does not improve the analytical predictions. If the value of this factor is changed from 3.7 to 3 or 4.5, the prediction of the critical stiffness decreases by 10% in both cases. As mentioned above, the critical stiffness decreases as the correction factor is either increased or decreased due to the competing effects of dissipation and diffusion.

Our numerical results also indicate that the transition from steady sliding to stick-slip is continuous. As the stiffness is increased towards the critical stiffness, the amplitude of stick-slip cycles approaches zero. The transition is continuous at all velocities tested in our study.

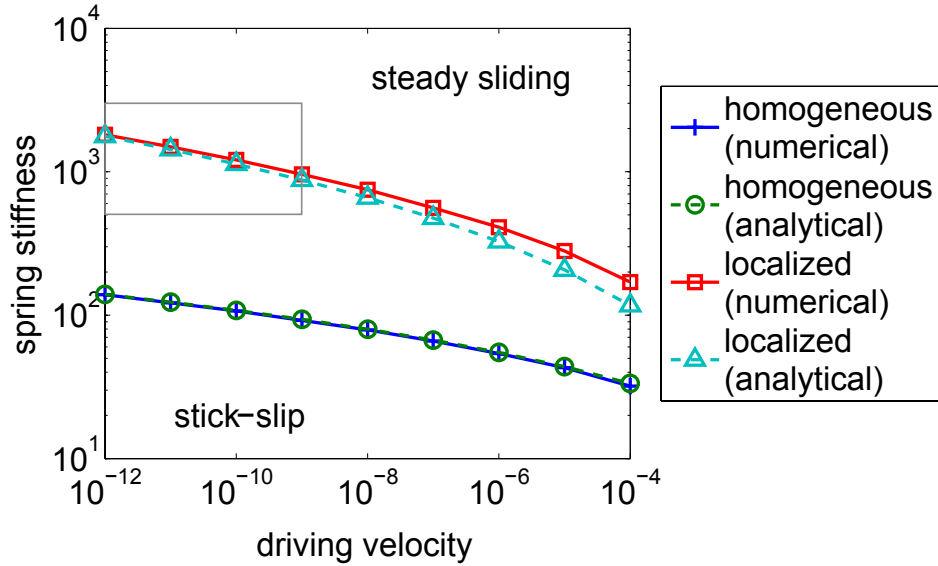


Figure 3.4: Comparison of analytical and numerical investigations of stick-slip. The plot shows the critical stiffness as a function of driving rate for the analytic expressions for homogeneous deformation and localized deformation (Equations (3.29) and (3.33), respectively) and the results obtained through numerical integration of the STZ equations. If the stiffness and driving rate are above the curve, then steady sliding is stable. If the values of the stiffness and driving rate are below the curve, motion occurs through stick-slip cycles. The analytical result for homogeneous shear matches extremely well with the numerical results. The prediction for localized deformation provides a good approximation of the shape of the boundary between stick-slip and steady sliding. The small discrepancy is due to the difficulty of estimating the shear band width  $a$ , as well as the fact that the strain rate is not constant in the shear band. The gray box indicates the region of parameter space where localized deformation produces multiple period stick-slip. This region is examined in detail in Figure 3.5.

### CHAPTER 3. STICK-SLIP INSTABILITIES

We also use numerical integration to explore the dynamics of stick-slip. We do not observe complex stick-slip cycles for the homogeneous case. We find that localization produces irregular stick-slip cycles in certain regions of parameter space. Simultaneous observations of irregular stick-slip and the internal effective temperature dynamics establishes a connection between the small scale physics and exotic macroscopic dynamics.

Multiple period stick-slip occurs for the lowest driving rates in our study, as shown in Figure 3.5. This is a closer look at the gray box at the far left of Figure 3.4, just below the localized transition from steady sliding to stick-slip. We see that there are many types of motion that occur in this small part of parameter space, including steady sliding, single period stick-slip, double period stick-slip, many ( $> 2$ ) period stick-slip, and material failure. Material failure refers to the fact that the strain rate becomes so large that the effective temperature diverges. Deformation in the amorphous material no longer occurs in isolated STZs at these large strain rates, and instead the deformation is more fluid-like. In the laboratory, stick-slip cycles are still likely to occur in this regime, but would require additional physics not included in STZ Theory to be accurately captured theoretically.

We look at two specific examples of the irregular slider dynamics, one example that exhibits two period stick-slip (the white square in Figure 3.5), and one example that exhibits many irregular stick-slip cycles (the square in Figure 3.5). Figure 3.6(a) shows shear stress as a function of load point displacement for stick-slip cycles with a doubled period. This stick-slip motion occurs for localized deformation with  $V_0 = 10^{-10}$  and  $k = 1100$ . The motion consists of a pair of alternating large and small events. The shear stress builds up to the same level during the “stick” phase of motion in both events, but the sticking time between slips alternates between two values. The slider slips much further during the big event, which relaxes the spring and drops the stress to a lower level, resulting in a longer sticking time following the large event compared to the sticking time after the small event. Figure 3.6(b) shows the slider velocity as a function of load point displacement. The large events result in a block velocity that is several orders of magnitude larger than in the small event. The inset (Figure 3.6(c)) shows an enlarged plot of the slider velocity during the “stick” phases, with labels identifying the small and large events. The slider moves slightly faster prior to the large event. However, the slider velocity is nearly an order of magnitude below the driving velocity during the “stick” phases prior to both events.

The slider slips more in the large event due to differences in the internal state of the material within the shear band – the strain rate profile in the material is different during large and small events. Both the slider velocity and the plastic strain rate are larger during the large stick-slip events. Small differences in the

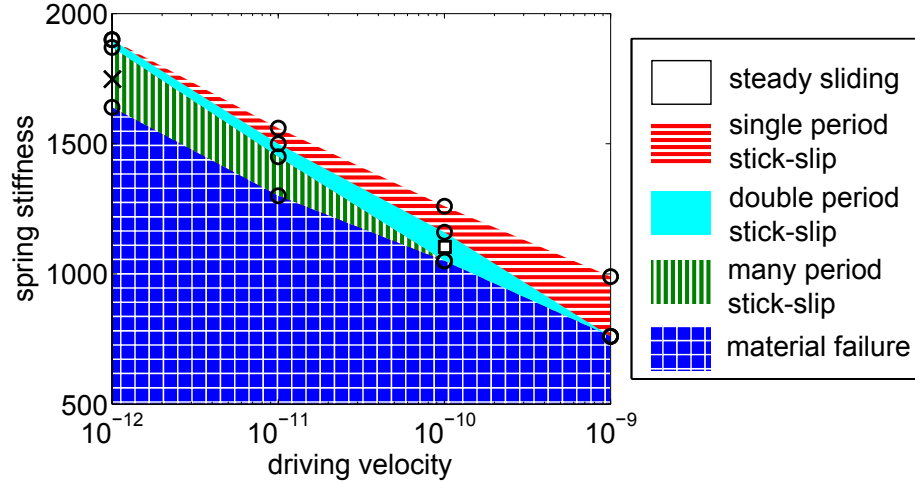


Figure 3.5: Diagram of parameter space where multiple period stick-slip occurs. This is a close-up of the gray box at the far left of Figure 3.4, just below the transition from steady sliding to stick-slip for localized deformation. In this smaller region of parameter space, many types of motion occur, including steady sliding, single period stick-slip, double period stick-slip, many ( $> 2$ ) period stick-slip, and material failure. All of the curves are plotted for localized deformation, as multiple period stick-slip does not occur for homogeneous shear. Material failure means that strain rates during the “slip” cycles are so large that STZ Theory breaks down. A laboratory slider would likely still exhibit stick-slip motion in this part of parameter space, but additional physics would have to be added to STZ Theory to model the motion theoretically. The circles indicate the specific values of  $k$  at fixed  $V_0$  where we observe a transition from one type of stick-slip motion to another. The white square indicates the specific example of double period stick-slip that we examine in Figures 3.6-3.7, and the “x” indicates the specific example of many period stick-slip that we examine in Figure 3.8.

CHAPTER 3. STICK-SLIP INSTABILITIES

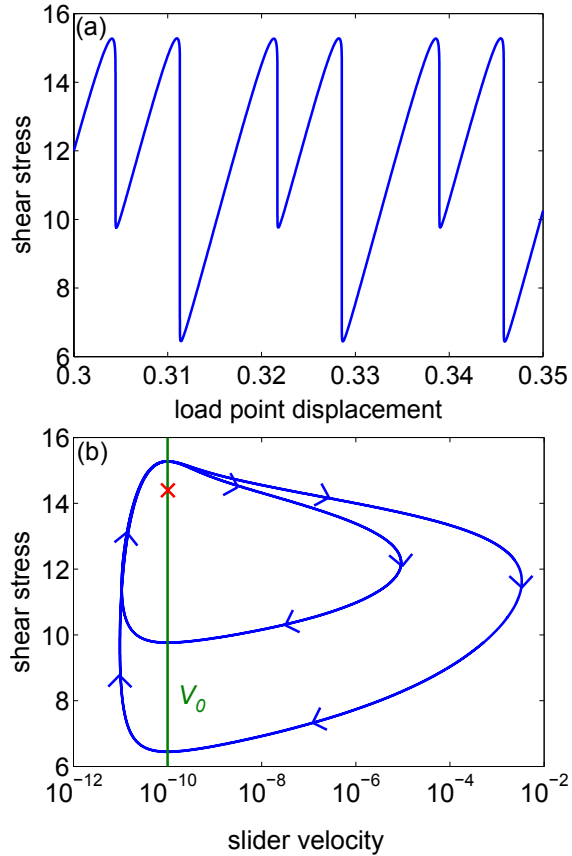


Figure 3.6: Two period stick-slip, with  $V_0 = 10^{-10}$  and  $k = 1100$ . This point in the parameter space is shown by a white square in Figure 3.5. (a) Shear stress as a function of load point displacement. Instead of a single stick-slip event, there are two different stress drop sizes. The stress builds up to the same level to initiate failure in both event sizes, but the recurrence time differs between the events. The block slips more in the large event due to the microscopic effects of localization. (b) Stress and slider velocity evolution during two period stick-slip. The slider velocity is several orders of magnitude larger in the large stick-slip event. The velocity evolution during the “stick” phase leading up to failure is very similar in the large and small events. The stick-slip events have different sizes because of the internal effective temperature profile, which we examine in detail in Figure 3.7.

CHAPTER 3. STICK-SLIP INSTABILITIES

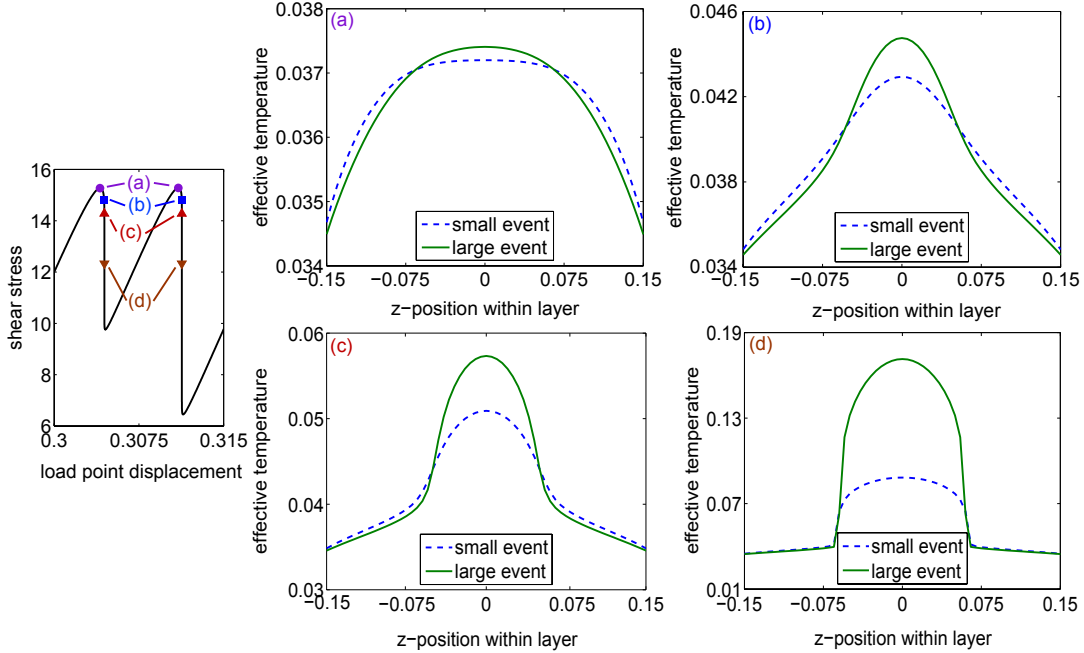


Figure 3.7: Close-up of the effective temperature shear band in large and small stick-slip events. The far left plot shows the shear stress as a function of load point displacement for a large and a small stick-slip event. At four different values of the stress, shown by the dots on the two different curves, we plot the effective temperature profile across the layer ( $z$ -direction). Because the stress is identical for the pair of curves in each of the four plots, the only difference between the block sliders is the effective temperature profile – the physical internal state of the sheared material is responsible for any differences in the dynamics. (a) At the peak stress prior to the slip event, the effective temperature profile is slightly different – the shear band is narrower and the effective temperature is larger in the center prior to the large event. (b) Because of feedbacks in the effective temperature dynamics, this difference is amplified, and the elevated effective temperature in the center point grows faster during the large event. This further increases the effective temperature at the center as the plots in (c) and (d) illustrate. Because the effective temperature is larger during the small event, the strain rate is larger and the shear stress drops to a lower value due to dynamic weakening. This is why the shear stress in the large event drops nearly twice as much as in the small event.

### CHAPTER 3. STICK-SLIP INSTABILITIES

effective temperature have a large impact on the slider dynamics. Figure 3.7 (far left) shows shear stress as a function of load point displacement for a large and small stick-slip event which alternate in a two period cycle. At a series of four values of the shear stress, we plot the effective temperature as a function of  $z$  position within the layer. Because the shear stress is equal, differences in the stick-slip events must arise from differences in the internal dynamics of the effective temperature.

Figure 3.7(a) shows the effective temperature at the stress peaks. Prior to the large event, the effective temperature is slightly elevated at the center of the material. Dynamic feedbacks in the effective temperature evolution during slip amplify this difference. The slightly elevated effective temperature implies a higher density of STZs at the center of the material. The strain rate is also larger, and so the material dissipates more energy. Energy dissipation leads to faster growth of the effective temperature, which produces the profiles in Figure 3.7(b). The difference is further amplified in Figure 3.7(c), and in Figure 3.7(d) the difference between the effective temperatures correspond to nearly a factor of 1000 increase in the plastic strain rate. As the effective temperature grows, the stress drops more rapidly during the large event due to dynamic weakening. Because the stress drop is larger, the block slides farther due to the decreased frictional resistance.

This mechanism leads to further period doublings as the spring stiffness decreases, until the cycles are irregular. Figure 3.8(a) shows the shear stress as a function of load point displacement for a series of irregular stick-slip events. This block slider system is driven at  $V_0 = 10^{-12}$  with a spring stiffness of  $k = 1700$ . The shear stress at which the slip cycle begins is very similar for both smaller and larger events. Figure 3.8(b) shows the evolution of stress and slider velocity during the four stick-slip events in the gray box in Figure 3.8(a). The slider velocity ranges over many orders of magnitude in the slip events. There is variation in the block velocity during the “stick” phase, though it is always well below the load point velocity  $V_0$ , shown by the horizontal line. The block velocity during the “stick” phase is largest following a small event, and smallest after a large event. However, the slider velocity during the “stick” phase is not completely indicative of the size of the next event, as the slider velocity during the “stick” phase takes on a range of values prior to both large and small slip events.

Figures 3.8(a) also shows that there are groups of smaller slip events followed by a larger slip event. The groups often have three or four stick-slip events, with several small events followed by a large event. Consecutive larger events can also occur, as can be seen around a load point displacement of 0.3 in Figure 3.8(a). The consecutive large events exhibit a smaller stress drop than the large events in the set of three or four events.

CHAPTER 3. STICK-SLIP INSTABILITIES

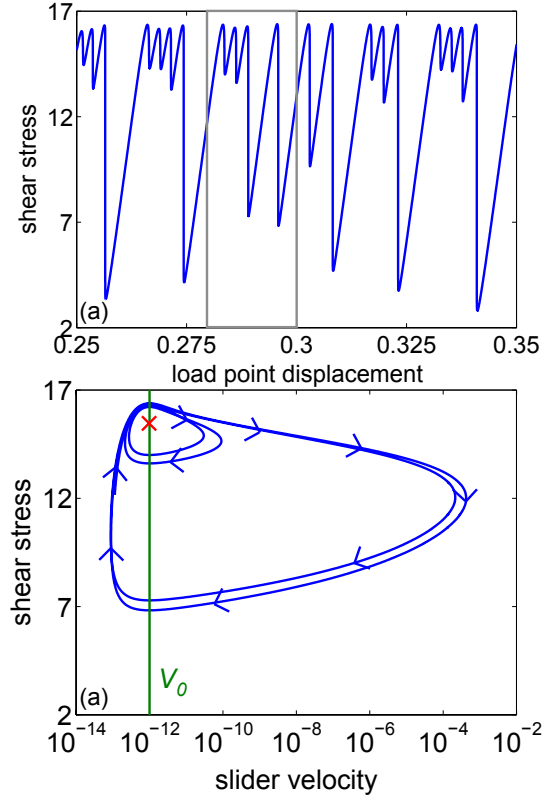


Figure 3.8: Irregular stick-slip events due to strain localization, with  $V_0 = 10^{-12}$  and  $k = 1700$ . This point in parameter space is shown by an “x” in Figure 3.4. (a) Shear stress as a function of load point displacement. Stress drops of many sizes occur, with irregular recurrence times. The peak stress is similar for all events, though there are some small variations. Events usually occur in groups of two or three, with one or two smaller events preceding a large event, but there can also be several consecutive larger sized events. (b) Stress and slider velocity evolution during complex stick-slip cycles. The plot shows the four stick-slip cycles in the gray box in (a). The innermost loop is the first small stick-slip, and the subsequent events are progressively larger. The vertical green line indicates the load point velocity  $V_0$ . The block velocity during sliding varies over many orders of magnitude. During the “stick” phase, there is variation in the velocity of the block. Small events are followed by increased block velocity during the “stick” phase, while the slider velocity is lower after large events. However, the slider velocity prior to a slip event does not determine its size.

The small scale physics of strain localization leads to the various sizes of slip events due to the same mechanism described above for the double period stick-slip cycles. The effective temperature is largest in the center of the material prior to the largest events, and then dynamic feedbacks cause the effective temperature to grow more rapidly, similar to the plots in Figure 3.7. The transitions to complex, chaotic behavior in our model arise from variations in the internal state of the material rather than instabilities associated with three (or more) macroscopic phenomenological degrees of freedom in a dynamic system, providing physical insight into the mechanisms that give rise to exotic friction behavior.

### 3.4 Discussion

Our study shows that strain localization plays an important role in stick-slip instabilities in amorphous materials. The critical spring stiffness is larger for localized deformation than for homogeneous deformation, and our analytic expressions for the critical stiffness are in good agreement with numerical integration. The primary effect that increases the critical stiffness for localized strain is an increase in the strain rate in the shear band. Diffusion also plays a role by mitigating the increase in the critical stiffness, though the increased strain rate is the dominant effect in determining the stability of steady sliding. Our analysis shows that the localization effect cannot be replicated in a homogeneous model by simply reducing the thickness of the material, and that resolving the microscopic dynamics is important for capturing the large scale friction.

Other constitutive laws such as Dieterich-Ruina also predict stick-slip motion [75]. In the Dieterich-Ruina law, the critical stiffness is independent of the driving rate, while in STZ Theory the stiffness decreases with increasing driving rate. This general trend is in agreement with laboratory experiments [84], and previous studies with STZ Theory that did not resolve the dynamic strain localization instability [58].

We also find that localized stick-slip can occur in irregular cycles. The effective temperature profile immediately before large and small events is slightly different, and this change in the microscopic physical state leads to macroscopically different friction dynamics. Phenomenological constitutive laws find that stick-slip can occur with irregular periods, though this requires additional state variables to provide the degrees of freedom necessary for chaotic stick-slip [76]. Our model instead relates irregular stick-slip to the internal physics of localization.

Many experiments show irregular stick-slip [85, 74, 67]. The exotic phenomena could arise from many different sources of complexity, such as additional

### CHAPTER 3. STICK-SLIP INSTABILITIES

time scales associated with the apparatus and/or complex molecules in the interfacial layer which have their own internal dynamics or entanglements. Our study shows that even for simple interfacial materials, the small scale physics of strain localization can also be a source of complexity. Experiments on simpler amorphous materials that can simultaneously examine the dynamics of strain localization (e.g. experiments that can image particle displacements) could examine the region in parameter space where we observe irregular stick-slip to test the connection STZ Theory makes between the microscopic physics and the microscopic dynamics.

Our model assumes that the effective temperature is only a function of position across the layer thickness. This simplifies the modeling, but experiments show that amorphous materials are heterogeneous in other spatial directions [86]. Extending slider models to additional dimensions may be important for fully capturing the complex stick-slip dynamics seen in various experiments.

Molecular dynamics simulations of amorphous materials show that stick-slip motion often occurs due to a phase transition from a solid to a fluid in the material [78]. This behavior is also observed in experiments [71]. The STZ model does not include the physics of this transition – melting occurs at the strain rate where the effective temperature diverges, but STZ Theory does not include a constitutive description of the material once it melts. At these high strain rates, plastic deformation no longer occurs in isolated STZs, and the material instead flows like a fluid. Future modeling efforts that incorporate this melting transition can determine its effects on stick-slip for comparison with simulations and experiments.

Experiments could determine the thickness of shear bands during stick-slip motion to test our quantitative predictions for the effect of localization. In thin films, the material is often only a few molecules thick [85]. So, for these systems, localization may not be important as the shear band thickness may be wider than the entire material. In thicker materials such as granular materials, this effect is more likely to be important. Daniels and Hayman [67] observed stick-slip events in a granular material and imaged particle displacements before and after the event. They found that slip occurred only over a few particle diameters in the layer for some of the stick-slip events. Experiments on granular materials where grains can be imaged, or experiments with fault gouge that examine gouge microstructures following the experiment [70] can determine the shear band thickness. Such experiments could potentially test our predictions for the effect of shear bands on stick-slip instabilities.

Our model for stick-slip does not include inertial effects. We assume that the frictional time scale dominates stick-slip motion, and that oscillations of the

### CHAPTER 3. STICK-SLIP INSTABILITIES

spring/mass system occur much faster than the inverse plastic strain rate time scale. Inertial effects are important in some regimes [79], and can be included in the block slider equations for numerical studies. However, these dynamical systems involve additional variables and analytical studies are consequently much more difficult. Stick-slip motion may require that the inverse plastic strain rate, mass/spring oscillation time, and stress equilibration time all be similar. This requires substantially more complicated modeling to resolve stress equilibration and wave propagation through the amorphous material. Addition of a mass resulted in chaotic motion with Dieterich-Ruina friction [87], so inertial dynamics could produce interesting dynamic phenomena in the STZ model.

Stick-slip instabilities are an important aspect of friction that must be understood to better constrain the dynamics of interfaces. Our results show that strain localization plays an important role in the macroscopic dynamics. Increasing the resolution of other relevant small scale phenomena in models of macroscopic dynamics should ultimately improve our ability to predict the deformation and failure in amorphous materials.

# Chapter 4

## Comparing Friction Laws in Dynamic Rupture

We now turn our attention to the fault scale and study dynamic earthquake ruptures that are governed by STZ Theory. In our novel multi-scale approach to the earthquake problem, our first research efforts assume that the shear strain in the fault gouge is homogeneous. This work occurred first chronologically, and therefore it utilizes the simpler Free Volume Law, which is an older STZ formulation than the version based on effective temperature. Because this dissertation is organized by scale rather than chronology, more recent work at the interface scale that uses the effective temperature version of STZ Theory is presented in Chapters 2 and 3. In this chapter, we make detailed comparisons between the Free Volume law and the Dieterich-Ruina and Slip Weakening laws, and determine the fault scale impact of the grain scale physics in a simplified version of STZ Theory. We extend the fault scale research to include spontaneous localization of strain in Chapter 5.

The work in this chapter is published by Daub and Carlson in the *Journal of Geophysical Research* [56]. Some of the discussion of constitutive laws from this paper appears in Chapters 1 and 2, while this chapter focuses on the results of the dynamic earthquake rupture simulations.

### 4.1 Constitutive Laws in Dynamic Rupture

In simulations of dynamic earthquake rupture, friction laws link characteristics of microscopic adhesion and dissipation to their implications for fault-scale behavior. A variety of friction laws have been studied in the context of individual

## CHAPTER 4. COMPARING FRICTION LAWS IN DYNAMIC RUPTURE

ruptures [88, 19, 89, 90, 91] and sequences of earthquakes [92, 93, 94]. Determining how friction laws arise from microscopic mechanisms and lead to complex behavior remains a central question in earthquake source physics.

Constitutive laws governing dynamic rupture models can be divided into two classes: (1) single variable slip-dependent or velocity-dependent laws, where shear stress weakens according to an *a priori* fixed function of slip or slip velocity, and (2) rate and state laws, which incorporate explicit rate (i.e. velocity) dependence and one or more physically motivated thermodynamic-like state variables to capture the history dependence of friction. In the single variable category, we consider the linear slip-weakening (SW) law [1, 2, 3], which is the most widely studied example in this class in the geophysical literature. Slip-weakening friction is discussed in Section 1.2.2, and purely slip velocity dependent laws are discussed in Section 1.2.3. The rate and state laws that we study include the Dieterich-Ruina (DR) law [10, 11], which is discussed in Section 1.2.4, and the Free Volume (FV) law, which connects fault evolution to microscopic physical processes in a layer of fault gouge [59] and is discussed in Chapter 2.

The linear SW law is frequently used as a simplified description of friction. The law prescribes a specific linear relationship between slip and weakening of the shear stress, depends on few parameters, and ignores more complicated processes such as dynamic re-strengthening and slip rate dependence. The DR law adds experimentally observed slip rate dependence, and re-establishes frictional strength after weakening through state variable evolution. The FV law uses Shear Transformation Zone Theory [24, 25] to model the plastic deformation of granular fault gouge, and incorporates dilation and compaction as the basis for fault weakening and re-strengthening, respectively.

The FV law provides a good description of laboratory experiments for boundary lubrication [58] and numerical simulations of dense granular flows [27]. In this study, we extend these investigations to fault-scale behavior and compare the FV law to the SW and DR law, contrasting their implications for dynamic rupture. Additionally, we consider versions of the DR and FV laws modified to include rapid velocity weakening. Because the physics of the earthquake source is poorly constrained, examining the dynamic ruptures that arise from different friction laws can aid seismologists in assessing the range of possible physical outcomes occurring at the earthquake source.

## 4.2 Comparing the DR and FV Models

Both the DR and FV friction laws depend on the slip rate and a single state variable. Rate and state laws are often analyzed in the context of velocity step experiments. In this section, we make a close comparison between these laws, and discuss the important differences between these friction laws. We consider the DR law with the ageing state variable evolution equation:

$$\tau = \sigma \left[ f_0 + a \log \left( \frac{V}{V_0} \right) + b \log \left( \frac{\theta V_0}{l} \right) \right]; \quad (4.1)$$

$$\frac{d\theta}{dt} = 1 - \frac{\theta V}{l}. \quad (4.2)$$

We compare the DR law with the FV law, which is given by the equations

$$V = V_* \exp[-f_* - (\chi_s + \chi_h)/\chi] (1 - m_0) \sinh(\tau/\sigma_d); \quad (4.3)$$

$$\frac{d\chi}{dt} = -R_c \exp(-\chi_c/\chi) + \alpha\tau V. \quad (4.4)$$

The value of  $m_0$  depends on whether the shear stress is above the yield stress:

$$m_0 = \begin{cases} 1, & [\tau \leq \tau_0 \exp(\chi_h/\chi)]; \\ \frac{\tau_0}{\tau} \exp(\chi_h/\chi), & [\tau > \tau_0 \exp(\chi_h/\chi)]. \end{cases} \quad (4.5)$$

We compare these two constitutive laws in detail in this section.

The transient behavior of a rate and state friction law is illustrated by a velocity step experiment. A single degree of freedom block is driven by an externally imposed velocity. Alternatively, one can interpret the velocity step as the response of a single degree of freedom elastic slider in the limit of an infinitely stiff spring constant. The block initially slides at the steady-state velocity  $V_{ss}$  with the state variable at the corresponding steady-state value. This is followed by a sudden step increase  $\Delta V$  in the imposed sliding velocity. The dynamic response of the slider is shown in Figure 4.1. Initially, shear stress increases (the so-called ‘‘Direct Effect’’); the magnitude of the increase is defined to be  $A$ . Over some characteristic length scale, defined to be  $L$ , the frictional stress evolves to its new value. The difference between the initial steady-state value of the stress and the new steady-state is defined to be  $A - B$  (the ‘‘Evolution Effect’’ is quantified by  $B$ ). Mathematically,

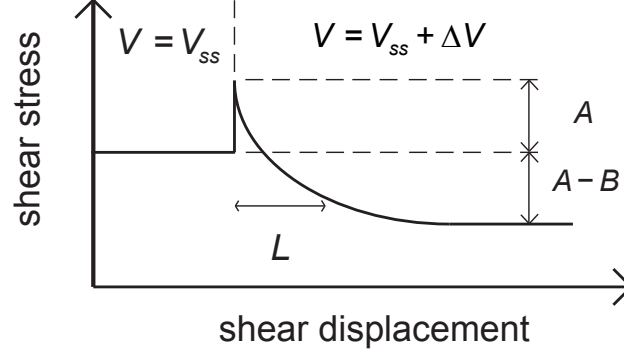


Figure 4.1: Shear stress versus slip for a velocity step experiment. The slip velocity is perturbed from steady sliding at  $V_{ss}$  to  $V_{ss} + \Delta V$ , and the transient response of the system is shown. The instantaneous increase in friction ( $A$ ), the length scale for evolution ( $L$ ), and the new steady-state ( $A - B$ ) are shown in the plot.

these parameters are identified by [95, 19]

$$A = V \left. \frac{\partial \tau}{\partial V} \right|_{V=V_{ss}, \theta=\theta_{ss}} ; \quad (4.6)$$

$$A - B = V \left. \frac{d\tau_{ss}}{dV} \right|_{V=V_{ss}} ; \quad (4.7)$$

$$L = - \left. \frac{V}{\frac{\partial(d\theta/dt)}{\partial \theta}} \right|_{V=V_{ss}, \theta=\theta_{ss}} . \quad (4.8)$$

The quantities  $A$  and  $L$  are evaluated at the initial steady-state values of the velocity and state variable, and  $A - B$  at the initial steady state velocity. The quantities  $A$ ,  $A - B$ , and  $L$  can be calculated for any rate and state law, and laws with more than one state variable will have a length scale associated with each state variable. We attach a subscript when referring to these quantities calculated for a specific friction law to distinguish them from the general definitions.

For the DR law, applying Equations (4.6)-(4.8) to Equations (4.1) and (4.2) results in the following:

$$A_{\text{DR}} = \sigma a; \quad (4.9)$$

$$(A - B)_{\text{DR}} = \sigma (a - b); \quad (4.10)$$

$$L_{\text{DR}} = l. \quad (4.11)$$

CHAPTER 4. COMPARING FRICTION LAWS IN DYNAMIC RUPTURE

This demonstrates that  $a$  and  $b$  determine the velocity dependence of friction, and that there is a fixed length scale  $l$  for transient effects.

Calculation of quantities  $A$ ,  $A - B$ , and  $L$  (Equations (4.6)-(4.8)) for the FV law enables a direct comparison with the equivalent parameters for the DR law. The resulting equations are rather cumbersome. Approximate expressions for  $A_{\text{FV}}$ ,  $(A - B)_{\text{FV}}$ , and  $L_{\text{FV}}$  are:

$$A_{\text{FV}} \approx \sigma_d; \quad (4.12)$$

$$(A - B)_{\text{FV}} \approx \sigma_d [1 - (\chi_s + \chi_h) / \chi_c]; \quad (4.13)$$

$$L_{\text{FV}} \approx \frac{\chi_{ss}^2}{\alpha \chi_c \tau_{ss}} = \frac{\chi_c}{\alpha \tau_{ss} \left[ \log \left( \frac{R_c}{\alpha \tau_{ss} V_{ss}} \right) \right]^2}. \quad (4.14)$$

The steady-state value of the shear stress  $\tau_{ss}$  is found by simultaneously solving Equation (4.3) (with the stress, free volume, and slip rate at steady-state) and the steady-state expression for the free volume  $\chi_{ss} = \chi_c / \log(R_c / (\alpha \tau_{ss} V_{ss}))$ . Note that  $\tau_{ss}$  depends on the slip rate, though it turns out that the stress does not change as much as the free volume with varying slip rates due to the logarithmic velocity dependence. These approximations assume that  $\sigma_d / \tau_{ss} \ll 1$  (i.e. the typical shear stress is much larger than the transient stress increase needed to flip an STZ) and that the stress is not close to the yield stress. The approximate values (Equations (4.12)-(4.14)) are within a few percent of the exact values for the parameters we choose as long as the steady-state stress is not near the yield stress (deviations from Equation (4.12)-(4.14) are most significant if  $m_0 \approx 1$ ). The approximation that the stress is not near the yield stress is appropriate for analysis of velocity step experiments where the slip rate is perturbed from steady sliding and the fault never stops sliding. However, when studying dynamic rupture, slip often initiates on a locked fault and deviations from these expressions can be more significant. Therefore, these expressions are useful in comparing the law to laboratory experiments, while the exact constitutive law (Equations (4.3)-(4.4)) is implemented into the dynamic rupture calculations. In our rupture simulations, we always start the fault at  $V = 0$  for simplicity, but rapid slip acceleration can still occur if the fault begins with a slip rate much slower than seismic slip rates.

The quantities  $A_{\text{FV}}$  and  $(A - B)_{\text{FV}}$  are independent of slip rate, as are the corresponding values in the DR law  $A_{\text{DR}}$  and  $(A - B)_{\text{DR}}$ . This verifies that the STZ activation stress  $\sigma_d$  is equivalent to the DR law direct effect stress  $a\sigma$ . Since the direct effect in the DR law is proportional to the effective normal stress,  $\sigma_d$  should also be proportional to the effective normal stress with a similar proportionality constant. The steady-state velocity dependence of both laws is logarithmic. If the reference free volumes satisfy  $\chi_s + \chi_h > \chi_c$ , the free volume law is steady-state

## CHAPTER 4. COMPARING FRICTION LAWS IN DYNAMIC RUPTURE

velocity weakening. In this manner, the FV law allows for the physical interpretation that the velocity dependence of friction is based on the relative values of these three characteristic free volumes. In the steady-state velocity weakening regime, as the slip velocity increases, the rate at which STZs flip orientation grows faster than the rate at which the gouge compacts. Therefore, lower stress is required to balance compaction and dilation to maintain the steady-state value of the free volume. The FV law predicts dilatancy hardening and steady-state velocity strengthening if  $\chi_s + \chi_h < \chi_c$ . Parameters in this regime do not allow for earthquake instabilities.

In experiments on laboratory faults, velocity weakening is usually not observed until strain localizes to a narrow shear band. Since the FV law assumes uniform strain throughout the gouge, we focus on matching the behavior of laboratory experiments once they reach the velocity weakening regime and a narrower active shearing thickness is established. One way to reconcile the observed trend in the velocity dependence of experiments with the velocity dependence of the FV law is to note that the reference free volumes depend on the constituents of the gouge. Since wear and comminution occur throughout the experiments, the reference free volumes could change (for instance, creation of smaller grains could decrease  $\chi_c$ ) to match the observed trend towards velocity weakening. These changes modify the porosity  $\phi$  without significantly changing the shearing thickness  $w$ . Since such changes alter the free volume and the reference free volumes, this will significantly alter the frictional properties of the gouge.

Figure 2.2 shows a plot of shear stress and free volume/porosity as a function of shear displacement for two different velocity steps. This verifies that  $A_{\text{FV}}$  and  $(A - B)_{\text{FV}}$  are independent of slip rate. The transient changes in stress are the same regardless of the sliding velocity, which confirms the predictions of Equations (4.12)-(4.13).

The key difference between the two friction laws involves the length scale for state variable evolution  $L$ . The length scale in the DR law  $L_{\text{DR}}$  is constant, while the length scale for the FV law  $L_{\text{FV}}$  varies with slip velocity (Equation (4.14)). In the FV law, in order to slip steadily at a higher velocity, the material must dilate (though the plot in Figure 2.2 shows that the changes in porosity are small compared to the overall porosity, so the layer thickness does not change significantly). Our calculation shows that  $L_{\text{FV}}$  is proportional to the square of the steady-state free volume and increases at higher slip rates. In the DR law, the natural length scale is the size of asperity contacts, which is independent of the slip rate and exhibits no velocity dependence. Seismic slip velocities range over many orders of magnitude, from slow quasistatic loading to unstable rapid slip. The varying length scale in the FV law has a potentially large impact.

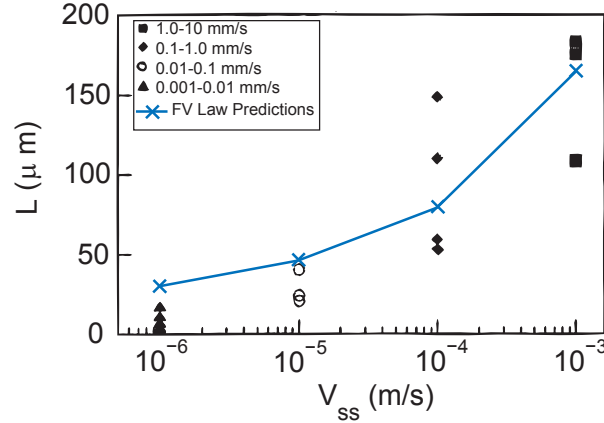


Figure 4.2: Experimental data for  $L$  [34] and the corresponding predictions of the FV law. The FV law predictions are given by Equation (4.14) with the following parameters:  $\chi_s = 0.3407$ ,  $\sigma_d = 0.25$  MPa,  $\chi_c = 0.1145$ ,  $f_0 = 222.3$ ,  $V_0 = 10^{-6}$  m/s,  $R_c = 5$  s $^{-1}$ ,  $\alpha = 0.3$  (MPa s) $^{-1}$ ,  $\chi_h = 0.0028$ , and  $\tau_0 = 44.12$  MPa. The DR law predicts that  $L$  is independent of slip rate – the above plot is a horizontal line for DR friction. The FV law follows the observed trends in laboratory faults.

Mair and Marone [34] observe systematic variations of the slip distance with slip rate for friction evolution in experiments involving fault gouge. Figure 4.2 compares the FV law and their laboratory data. Values of  $L_{FV}$  are calculated from Equation (4.14). We note variations in  $L_{FV}$  with slip velocity that exhibit behavior very similar to laboratory faults. This suggests the FV law may capture important behavior for gouge filled faults which is absent in the DR law.

The plots in Fig. 2.2 show that the length scale  $L_{FV}$  depends on the slip rate. The displacement needed for stress to weaken to its new steady value is larger in the second velocity step (from  $10^{-5}$  m/s to  $10^{-4}$  m/s) than in the first velocity step (from  $10^{-6}$  m/s to  $10^{-5}$  m/s). This is easiest to see in the lower plot in Fig. 2.2, as the free volume is still evolving at the right edge of the plot while the free volume has stabilized within the same displacement during the previous velocity step.

In addition to the slip rate dependence of  $L_{FV}$ , the FV law provides a means to quantitatively bridge the difference in scales between laboratory faults and natural faults. Because the DR law is phenomenological, it is difficult to estimate precisely how the DR parameters  $a$ ,  $b$ , and  $l$  (Equation 1.2) may or may not

depend on the scale of the fault. The FV law based on grain-scale physics includes a specification for how parameters depend on the scale of the fault or experiment. The dilation coefficient  $\alpha$  is inversely proportional to the slipping thickness  $w$ . This is because the dilation term depends on the strain rate. The strain rate will be larger for a thinner layer at a given slip velocity, and the scaling of  $\alpha$  with  $w$  reflects this. The FV Law predicts  $L_{FV} \propto w$  (since  $L_{FV} \propto 1/\alpha$  and  $\alpha \propto 1/w$ ), and increasing the width of the gouge layer increases the length scale in the FV law. This predicted scaling is consistent with the experiments of Marone and Kilgore [96]. This suggests natural faults exhibit a length scale a few orders of magnitude greater than laboratory values. The direct effect  $A_{FV}$  and the steady-state velocity dependence  $(A - B)_{FV}$  are independent of the layer thickness  $w$ , and remain unchanged with fault scale.

The thickness of the actively shearing layer in laboratory experiments cannot be directly measured since strain tends to localize within the gouge during experiments. Because strain localizes over many velocity steps, we assume that during an individual velocity step the shear band thickness is uniform, and the uniform shear assumption in the FV law is a good approximation for that single velocity step. We can then use the FV law to estimate the shear band thickness of the laboratory experiments. Using the same parameters as in Figure 4.2, we can calculate the change in free volume due to a velocity step. The change in pore space is due to layer dilation, so the additional porosity due to dilation is approximately  $dw/w$ , where  $dw$  is the measured change in layer thickness. Therefore, the change in free volume  $d\chi$  (equal to the porosity change) is related to the layer thickness  $w$  and the thickness change  $dw$  by  $d\chi = dw/w$ , so given an experimental value of  $dw$  an estimate of  $w$  can be computed. We find that with  $w = 0.75$  mm, the FV law follows the dilation data for experiments in the velocity weakening regime [34]. This calculated value is also within reason given the microstructural observations in the experiments. For natural faults we estimate  $w = 0.45$  m, a typical thickness of the gouge layer in a study by Chester and Chester [37]. The estimates of  $w$  for laboratory and natural faults allow us to determine the parameters for our rupture dynamics simulations for natural faults.

### 4.3 Dynamic Ruptures

In this section, we compare the effects of the SW, DR, and FV laws in the spontaneous propagation of elastodynamic ruptures. The previous section considers small single degree of freedom sliders to determine  $A$ ,  $A - B$ , and  $L$  for each law. Now we numerically simulate ruptures that propagate along faults for

## CHAPTER 4. COMPARING FRICTION LAWS IN DYNAMIC RUPTURE

which the length is typically orders of magnitude larger than laboratory samples. Comparisons between the SW and DR laws have been made for dynamic rupture simulations [97]. Here we extend comparisons to include the FV law.

We model the fault as the interface between two homogeneous, isotropic, linear elastic half spaces (Figure 4.3). The fault is the  $xy$  plane, and this boundary is governed by the chosen friction law. We consider only simple 2D in-plane or anti-plane ruptures, and thus by symmetry all quantities on the fault plane have no  $y$  dependence. Due to this imposed in-plane or anti-plane geometry, the vector slip velocity reduces to a scalar  $V(x, t)$ , and the stress tensor has only one shear component  $\tau(x, t)$ . For in-plane ruptures, the slip velocity only has a component in the  $x$ -direction ( $V(x, t) = V_x(x, t)$ ) and the shear stress is the  $xz$ -component ( $\tau(x, t) = \tau_{xz}(x, t)$ ), while in anti-plane problems the slip rate has only a  $y$ -component ( $V(x, t) = V_y(x, t)$ ) and the shear stress is the  $yz$ -component ( $\tau(x, t) = \tau_{yz}(x, t)$ ).

The elastodynamic equation requires that on the fault plane, the shear stress  $\tau(x, t)$  and the slip velocity  $V(x, t)$  satisfy [98, 88]

$$\tau(x, t) = \tau_{\text{load}}(x) + f(x, t) - \frac{\mu}{2c_s}V(x, t). \quad (4.15)$$

The stress and slip rate also satisfy the friction law on the fault, and the two equations are solved simultaneously. The initial loading stress  $\tau_{\text{load}}(x)$  is constant except for a small overstressed patch spanning the full depth of the fault of width  $L_{\text{trig}}$  (where the initial load is  $\tau_{\text{trigg}}$ ). This patch, the medium shade of gray in Figure 4.3, nucleates the rupture. This does not capture the slow nucleation process that initiates real earthquakes, but this simple nucleation procedure preserves the differences between ruptures with various friction laws. The stress transfer functional  $f(x, t)$  tracks dynamic stress changes due to past fault slip, and the final term explicitly extracts radiation damping [98], where  $c_s$  is the shear wave speed and  $\mu$  is the shear modulus. We calculate the stress transfer functional  $f(x, t)$  using a spectral method [88, 99], and use the displacement formulation of this method. Note that although the radiation damping term is present in Equation (4.15), our method of computing  $f(x, t)$  accounts for the full elastodynamic response and does not result in a quasidynamic model.

Periodic boundary conditions are imposed on the fault. To prevent replicas of the rupture from affecting the solution, we place strong frictional barriers to rupture at the outer edge of the fault (the darkest shade of gray in Figure 4.3). For the SW law, this barrier is defined by a large value of the yield stress. For the DR and FV laws, the barrier is obtained by increasing the value of  $A$ . The specifics of the outer fault barriers do not affect the solution we calculate on the portion

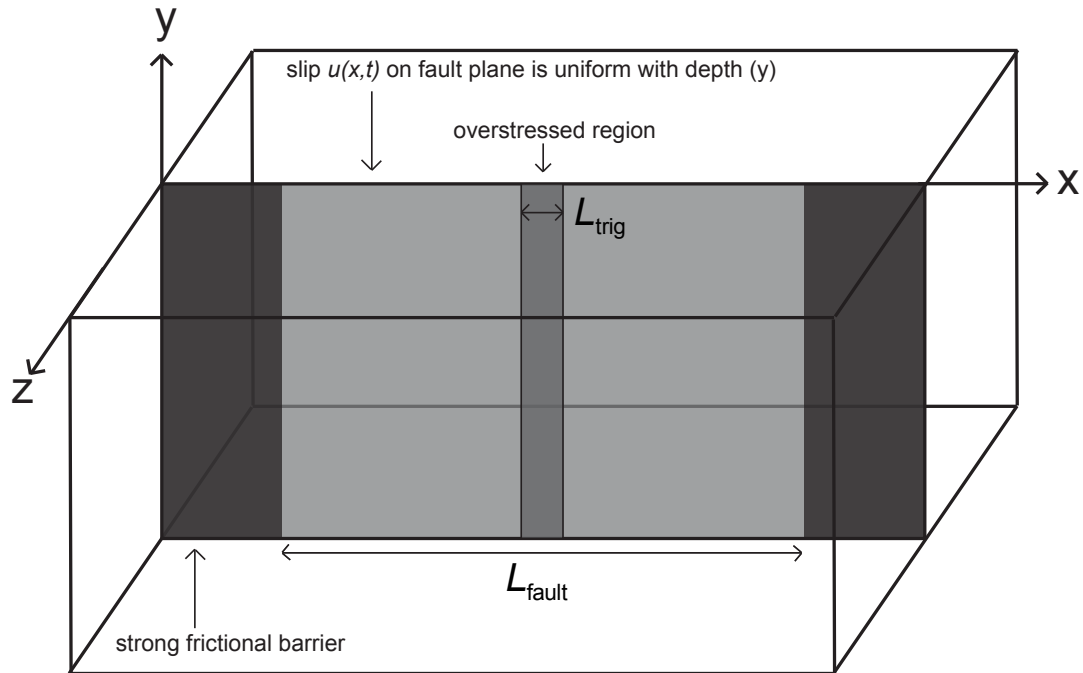


Figure 4.3: Schematic of the fault used in dynamic rupture calculations. Two identical homogeneous, isotropic, linear elastic half spaces are loaded far from the fault. Slip varies only in the  $x$ -direction, and boundary conditions are periodic. The symmetry in the  $y$ -direction requires that the slip and slip rate are scalars, either in the  $x$ -direction for in-plane loading or in the  $y$ -direction for anti-plane loading. The initial load is uniform except for an overstressed patch (medium shade of gray) which triggers rupture, and friction parameters are uniform except for strong barriers (darkest shade of gray) to prevent periodic replicas from affecting the solution.

## CHAPTER 4. COMPARING FRICTION LAWS IN DYNAMIC RUPTURE

of the fault that can rupture. Integration in time is achieved using a second order Runge-Kutta scheme [100].

Previously, Lapusta *et al.* [100] confirmed that simulations of anti-plane elastodynamic ruptures with the DR law are numerically stable. They identified a critical cell size  $h^*$  for velocity-weakening friction parameters, with

$$h^* = \frac{\gamma\mu L}{B - A}. \quad (4.16)$$

Ruptures were numerically stable if the spatial grid spacing  $dl$  was much smaller than  $h^*$ . The model-dependent  $\gamma$  is a constant of order unity, and  $\mu$  is the shear modulus. For in-plane ruptures, the same expression applies with the shear modulus  $\mu$  replaced by the expression  $\mu/(1 - \nu)$ , where  $\nu$  is Poisson's ratio [20]. For our analysis, we can extend these results to the FV law, but because the length scale  $L_{FV}$  is slip rate dependent, we must replace  $L$  in Equation (4.16) with the minimum of  $L_{FV}$  over all slip rates to determine the critical cell size for FV law ruptures. From Equation (4.14), we determine that the smallest value of  $L_{FV}$  occurs at the smallest value of the free volume. In single event rupture calculations, this is the initial value of the free volume at  $t = 0$ . We choose a spatial grid spacing  $dl$  that satisfies  $h^*/dl = 40$  and this choice gives well-resolved simulations. Parameters for our simulations are given in Table 4.1 unless otherwise noted.

Shear stress in ruptures utilizing the DR and FV laws does not have explicit dependence on slip. Instead, the slip dependence of shear stress is deduced from dynamic rupture simulations, which was done for the DR law by Okubo [101] and Bizzarri and Cocco [102]. In Figure 4.4 we show how stress weakens as a function of slip for each law at a point 4 km from the hypocenter. We only plot the portion of the curve where the stress is weakening, and for slip beyond the range of the plot the stress is constant in the SW law and relatively constant (increasing slightly due to dynamic re-strengthening) in the DR and FV laws. The linear slip weakening law follows the prescribed curve, as expected. The DR law weakens linearly with slip, and the slip required for the DR law to reach its minimum stress is larger than  $L_{DR}$ , as noted by Bizzarri and Cocco [102]. The ratio between the total slip required to reach the minimum shear stress and  $L_{DR}$  is about 15, which corroborates the results of Cocco and Bizzarri [103] and Lapusta and Rice [104]. The DR law matches the SW law nearly identically – this close match is a deliberate result of our choice of the friction parameters which equates the peak stress and the area under each curve for the first meter of slip. The cutoff at one meter was chosen to be larger than the amount of slip needed to reach the minimum shear stress. The area under the plot of shear stress as a function of slip determines the energy lost to frictional dissipation per unit area (the combination

CHAPTER 4. COMPARING FRICTION LAWS IN DYNAMIC RUPTURE

Table 4.1: Parameters for dynamic rupture simulations. Shared model parameters are: grid spacing  $dl$ , number of spatial grid points  $nx$ , shear modulus  $\mu$ , shear wave speed  $c_s$ , Poisson's ratio  $\nu$ , Courant-Friedrichs-Lewy Ratio  $cfl = c_s dt/dl$  (determines the time step  $dt$ ), length of the fault permitted to rupture  $L_{\text{fault}}$ , size of the triggering patch  $L_{\text{trigg}}$ , initial shear load  $\tau_{\text{load}}$ , and stress in the triggering patch  $\tau_{\text{trigg}}$ . The frictional parameters are discussed with each model in the main text.

| Dynamic Rupture Simulation Parameters   |   |
|---|---|
| Shared Parameters   | SW Law  |
| $dl = 0.01$ km<br>$nx = 2048$<br>$\mu = 32.03812032$ GPa<br>$c_s = 3.464$ km/s<br>$\nu = 0.25$<br>$cfl = 0.3$<br>$L_{\text{fault}} = 16$ km<br>$L_{\text{trigg}} = 1.3$ km<br>$\tau_{\text{load}} = 68$ MPa<br>$\tau_{\text{trigg}} = 74$ MPa | $d_c = 0.31$ m<br>$\tau_p = 73.85$ MPa<br>$\tau_d = 63.375$ MPa   |
| FV Law  | DR Law  |
| $\chi_s = 0.3407$<br>$\sigma_d = 0.25$ MPa<br>$\chi_c = 0.1145$<br>$f_* = 222.3$<br>$V_* = 10^{-6}$ m/s<br>$R_c = 5$ s $^{-1}$<br>$\alpha = 0.0005$ (MPa m) $^{-1}$<br>$\chi_h = 0.0028$<br>$\tau_0 = 44.12$ MPa<br>$\chi(t = 0) = 0.0061$    | $L_{\text{DR}} = 21.5$ mm<br>$a = 0.0027$<br>$b = 0.0077$<br>$f_0 = 0.7$<br>$V_0 = 10^{-6}$ m/s<br>$\sigma = 100$ MPa<br>$V_1 = 10^{-6}$ m/s<br>$\theta(t = 0) = 21500$ s |

CHAPTER 4. COMPARING FRICTION LAWS IN DYNAMIC RUPTURE

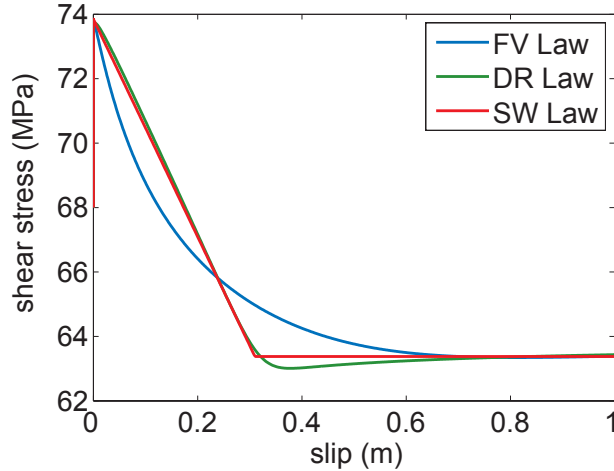


Figure 4.4: Plots of shear stress as a function of slip for an anti-plane rupture at a point 4 km away from the hypocenter for the linear SW, FV and DR laws. The SW law weakens linearly with slip by construction. The DR law also exhibits linear weakening with slip, and its close match to the SW law is due to intentional choice of parameters. The FV law weakens more rapidly with initial slip due to the small value of  $L_{FV}$  at low slip rates, while weakening is more gradual at larger slips when the fault slips more rapidly. The FV law requires more total slip to fully weaken to its minimum shear stress. The shear stress increases slightly for the FV and DR laws beyond the range of the plot as the time-dependent healing in each law results in some re-strengthening. Parameters were chosen for the laws to have equal areas under the slip weakening curve and thus have the same energy lost to frictional dissipation. Parameters are given in Table 4.1.

of fracture energy and shear heating). Matching the area under the stress versus slip curve for each law is motivated by the fact that earthquake fracture energies are the most reliable frictional quantity that can be estimated from ground motion observations [105]. By equating this quantity for all three laws, we assume that the partitioning of released strain energy between dissipation and seismic radiation is the same.

The FV law exhibits weakening that differs significantly from the other laws. During the initial phases of slip (i.e. at low slip rates), the length scale  $L_{FV}$  is relatively small, and consequently stress weakens rapidly with slip. The length scale  $L_{FV}$  increases at larger slip rates, and as a result the curve exhibits an

## CHAPTER 4. COMPARING FRICTION LAWS IN DYNAMIC RUPTURE

increasingly gentle slope once the fault begins to slip more rapidly. Compared to the DR and SW laws, the initial onset of weakening occurs more rapidly for the FV law, while the total slip distance over which the fault weakens is ultimately larger.

Both the FV and DR laws have a slip-hardening phase as slip initiates. The duration of slip-hardening is very short, only lasting for the first few millimeters of slip in both the FV and DR laws, and it is difficult to see in Figure 4.4. The peak stress is reached at a slip of 1.04 mm for the FV law and 3.32 mm for the DR law. This difference is due to the smaller length scale in the FV law at low slip rates. However,  $L_{FV}$  is smaller than  $L_{DR}$  by approximately a factor of two at small slip rates, indicating that the duration of slip hardening does not scale linearly with the length scale in the friction law.

Time histories of the dynamics on the fault at a point 4 km from the hypocenter are shown in Figure 4.5. With the chosen parameters each friction law supports ruptures that are expanding cracks. Note that an expanding crack is a rupture in which there is no healing during the expanding phase of the slip. Instead, the rupture grows, and slip ceases only after encountering the boundary. In contrast, a self-healing pulse corresponds to a narrow rupture where healing occurs shortly after the arrival of the rupture front.

The slip rate plots in Figure 4.5 illustrate the crack-like nature of the earthquake simulation with all friction laws. The DR and SW laws are nearly identical in the dynamic evolution of slip rate and shear stress, confirming the results of Bizzarri *et al.* [97]. As in Figure 4.4, this is an intentional consequence of our parameter choices. The DR rupture front arrives slightly earlier than that of the SW law. Other than this difference, the SW and DR laws exhibit nearly identical time histories for both slip rate and shear stress. The rupture front arrives earliest in the FV law; this is due to the smaller value of  $L_{FV}$  at nucleation slip velocities. The FV law also exhibits lower peak slip rates. The difference in the peak slip rate is due to the largest slip rates occurring just prior to the shear stress reaching its minimum value. While the stress is decreasing, stored elastic energy is released and slip accelerates. Throughout this process, the more rapidly the shear stress weakens, the larger the slip acceleration. For the FV law, the rate that stress weakens with slip is not uniform, which means that slip accelerates very rapidly at first, and less rapidly as the weakening rate decreases. The weakening rate of the FV law rupture is lower than that of the DR or SW law ruptures when the ruptures reach their peak slip rate. Consequently, the maximum slip rate for the FV law rupture is smaller.

State variable evolution is similar for the FV and DR laws. Arrival of the crack tip causes a period of rapid dilation followed by more gradual compaction for the

CHAPTER 4. COMPARING FRICTION LAWS IN DYNAMIC RUPTURE

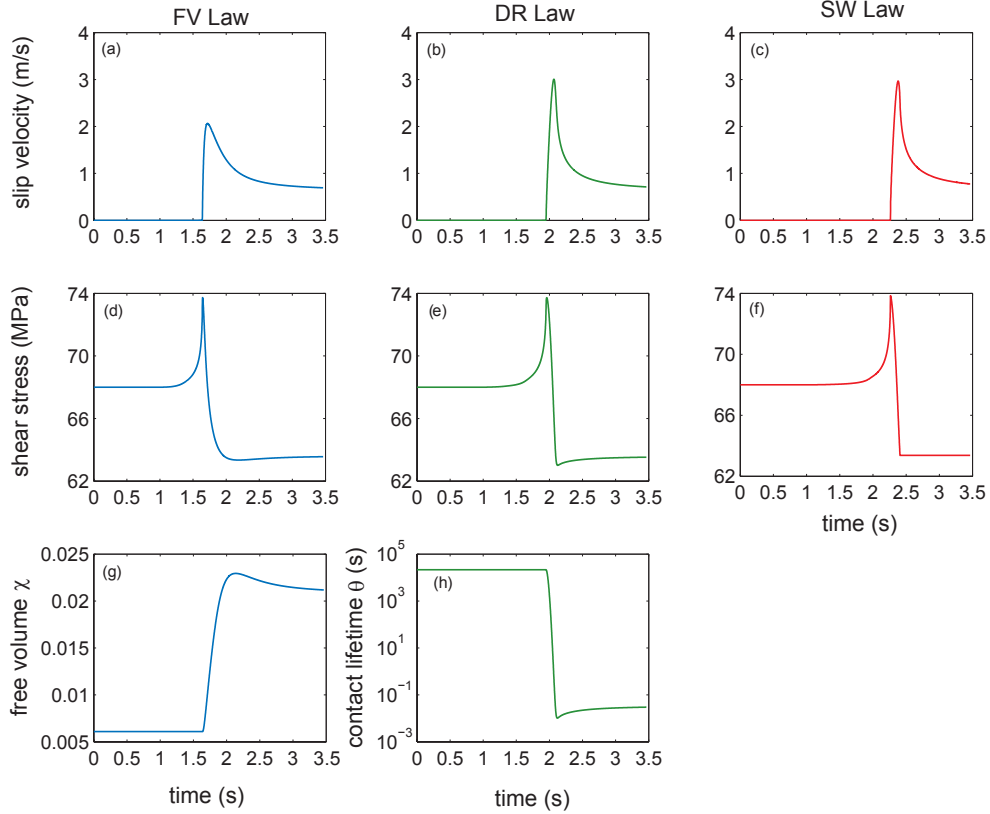


Figure 4.5: Fault dynamics during rupture at a point 4 km away from the hypocenter for the FV (a,d,g), DR (b,e,h), and SW (c,f) laws. As a function of time, (a)-(c) plot slip rate, (d)-(f) plot shear stress, and (g)-(h) plot the appropriate state variable for the FV or DR law. The velocity plots show all laws support expanding crack solutions. The FV law rupture arrives slightly earlier – the rupture reaches the limiting shear wave speed more rapidly due to the smaller nucleation length in the FV law. The peak slip velocity is also smaller for the FV law. The ruptures governed by the SW and DR laws have nearly identical time dependence of slip rate and shear stress. The DR law rupture arrives slightly earlier, but otherwise the laws produce matching ruptures. Shear stress increases at the crack tip to induce slip, and the minimum shear stress occurs at the extreme value of the respective state variable for the FV and DR laws. Parameters are given in Table 4.1.

## CHAPTER 4. COMPARING FRICTION LAWS IN DYNAMIC RUPTURE

FV law. The contact lifetime in the DR law drops very rapidly initially, and grows slightly on the crack interior. The minimum shear stress in each law corresponds to the maximum value of the free volume in the FV law or the minimum contact lifetime in the DR law.

For in-plane ruptures, an important distinction between the friction laws arises in the context of supershear ruptures. The in-plane geometry permits rupture velocities faster than the shear wave speed, confirmed in simulations by *Andrews* [1976b] and laboratory experiments by *Rosakis et al.* [106]. Supershear ruptures radiate seismic waves away from the fault in a different manner than subshear ruptures [49], and seismic records give evidence for supershear rupture velocities in several earthquakes [107, 108, 109].

The nucleation length of the friction law influences the transition to supershear. Sub-Rayleigh ruptures radiate shear waves ahead of the crack tip on the fault. If the stress peak due to this shear wave is large enough, it can initiate unstable slip that propagates faster than the shear wave speed. For matching frictional dissipation, the FV law has a smaller nucleation length. Given identical initial shear loads and frictional dissipation, the smaller nucleation length can allow a supershear transition to occur for the FV law when a DR rupture remains sub-Rayleigh. This phenomena is illustrated in Figure 4.6. These plots show the spatio-temporal evolution of slip rate for both the FV and DR friction laws. Both ruptures start out as expanding sub-Rayleigh cracks, and the smaller nucleation length for the FV law enables a transition to supershear rupture. A crack-like rupture is maintained throughout fault slip for both friction laws.

Fixing all model parameters except for the initial shear stress  $\tau_{\text{load}}$  and the length scale at nucleation slip rates (the value of  $L_{\text{FV}}$  at the initial free volume, or  $L_{\text{DR}}$ ), we generate a diagram which distinguishes between when the rupture transitions to supershear versus when it remains sub-Rayleigh. The length scale in the DR law is varied by changing  $l$ . Note that the initial value of the state variable depends on  $l$  ( $\theta(t=0) = l/V_1$ ), and this is also altered by changes in  $l$ . The length scale in the FV law is altered by changing the dilation coefficient  $\alpha$  and the compaction rate  $R_c$ , keeping the relative magnitude of dilation and compaction  $\alpha/R_c$  fixed (the steady-state friction depends on only the combination  $\alpha/R_c$ ). All other parameters in Table 4.1 remain fixed for all simulations. The nucleation patch is the same in every simulation. The differences in the supershear transition between the DR and FV laws are independent of the nucleation procedure.

The resulting diagrams are shown in Figure 4.7 with the horizontal axis showing either (a) the frictional energy dissipated per unit area at a point 4 km from the hypocenter in the first meter of slip, or (b)  $L$  at nucleation slip rates. The vertical axis is the initial shear load  $\tau_{\text{load}}$  in both plots. Points on each plot are

CHAPTER 4. COMPARING FRICTION LAWS IN DYNAMIC RUPTURE

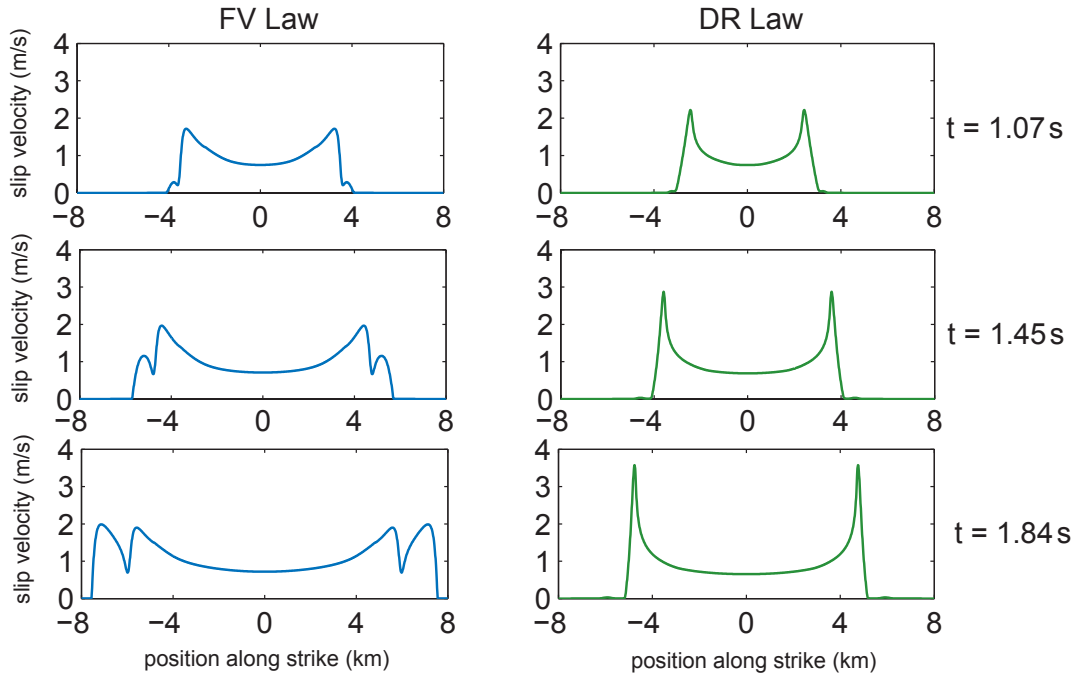


Figure 4.6: Snapshots of slip velocity along strike at three different times. Results are plotted for the FV law on the left and the DR law on the right. Initial conditions on the fault are identical, as is the amount of energy lost to frictional dissipation. The smaller nucleation size of the FV law allows the rupture to transition to supershear, while no supershear rupture occurs for the DR law. Parameters are the same as in Table 4.1 except  $\tau_{\text{load}} = 69$  MPa,  $R_c = 5.7$  s $^{-1}$ ,  $\alpha = 0.00057$  (MPa m) $^{-1}$ ,  $l = 18.45$  mm, and  $\theta(t = 0) = 18450$  s.

the largest value of the (a) dissipated energy per area or (b)  $L$  at which unstable supershear rupture was observed in our simulations. Above and to the left of these points, the crack will propagate faster than the shear wave speed. Growth of ruptures for conditions below and to the right are confined to sub-Rayleigh speeds. Plot (a) confirms more systematically what was observed in Figure 4.6. Given equal frictional energy dissipation, for a range of initial shear loads the FV law can nucleate supershear rupture when the DR law cannot. If  $L$  at nucleation slip rates is matched between the two laws, the reverse is true and ranges of parameters exist where the DR law permits transition to supershear which is absent for the FV law. However, in this case the frictional energy dissipated is much greater for the FV law because of the velocity dependence of  $L_{FV}$  which takes its smallest value at the onset of rupture.

## 4.4 Rapid Weakening

There is increasing experimental evidence that friction at rapid slip velocities is lower than what would be predicted by extrapolating the DR law to seismic slip velocities [110, 21, 22, 111, 112]. Many earthquake modelers adapt constitutive laws that weaken rapidly with velocity to account for the weakening observed in the laboratory. Neither the DR law nor the FV law considered in the previous section incorporates weakening which is faster than logarithmic with slip rate. Both laws must be modified to account for rapid weakening. In this section, we develop the rapid weakening constitutive laws and implement them into dynamic rupture simulations to assess how the slip rate dependence of  $L_{FV}$  impacts dynamic ruptures that weaken more rapidly than logarithmically with slip rate.

Recently, Rice [113] introduced a modification of the DR law based on flash heating at asperity contacts. The modified DR law allows for rapid velocity weakening at higher slip rates. The modification is implemented using a phenomenological correction factor which provides a crossover from weakening logarithmically at small slip rates to weakening as  $1/V$  at seismic slip rates. The characteristic slip rate  $V_W$  at which this functional change in weakening occurs is estimated based on thermodynamic calculations to be 0.1-1 m/s [113]. The discussion in Rice [113] focused mainly on the steady-state friction at high slip rates, while the actual friction law used in simulations [23] matches the one we present here.

The phenomenological correction for flash heating to the DR law results in a modification to Equation (1.2) of the form

$$\tau = \frac{\sigma [f_0 + a \log(V/V_0) + b \log(\theta V_0/l)]}{1 + l/V_W \theta}. \quad (4.17)$$

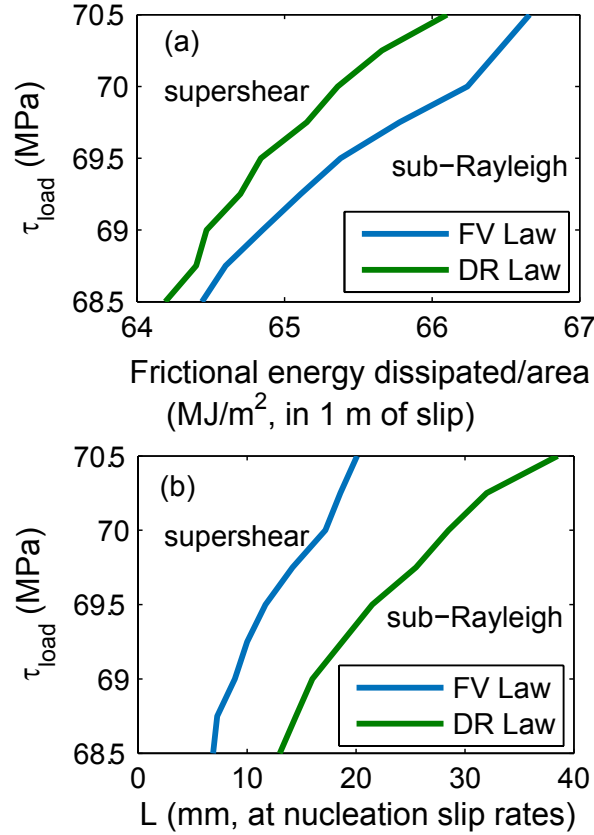


Figure 4.7: Rupture type diagrams for in-plane ruptures with the FV and DR laws as a function of the initial shear load and (a) energy per unit area dissipated by friction during the first meter of slip at a point 4 km from the hypocenter, (b)  $L$  at nucleation slip rates. Each individual point on the plot is the largest energy per area or  $L$  at which unstable supershear rupture is observed to develop on the bounded fault. Above and to the left of these points, supershear ruptures will occur, and below and to the right crack growth is confined to sub-Rayleigh speeds. For equal dissipated frictional energy (a), the FV law curve is further to the right and a region exists between the curves where the FV law transitions to supershear and the DR law does not (Figure 4.6 illustrates a specific example in this region). In (b), the DR law curve sits to the right, and DR law can rupture faster than the shear wave speed while the FV law does not for identical initial shear loads.

CHAPTER 4. COMPARING FRICTION LAWS IN DYNAMIC RUPTURE

The law maintains the ageing evolution law for the state variable  $\theta$ , Equation (1.3). For our rapid weakening simulations with the DR law, Equation (4.17) is used as the constitutive model for the fault. This modifies the steady-state friction so that

$$\tau_{ss} = \frac{\sigma [f_0 + (a - b) \log (V_{ss}/V_0)]}{1 + V_{ss}/V_W}. \quad (4.18)$$

The DR flash heating law at steady state (Equation (4.18)) introduces the factor  $(1 + V_{ss}/V_W)^{-1}$  to the friction law, which modifies the friction at the large slip rates when heating of asperity contacts becomes significant. This law has been used in dynamic rupture calculations. For low loading stresses, the DR law with flash heating tends to produce ruptures that are self-healing pulses rather than expanding cracks [19]. It has been suggested that earthquakes propagate as self-healing pulses [53]. In order to compare the DR and FV laws in this regime, we alter the FV law to allow rapid weakening which can also lead to pulse-like rupture. We modify the FV law to match the functional form of the steady-state velocity weakening in the DR flash heating model (Equation (4.18)).

The rapid weakening friction law that we adopt for dynamic rupture simulations is

$$V = V_* \exp [-f_* - (\chi_s + \chi_h) / \chi] (1 - m_{RW}) \times \sinh \left[ \tau / \sigma_d + \frac{R_c}{\alpha \sigma_d V_W} \exp (-\chi_c / \chi) \right]; \quad (4.19)$$

$$\frac{d\chi}{dt} = -R_c \exp (-\chi_c / \chi) + \alpha \tau V. \quad (4.20)$$

These correspond to Equations (4.3)-(4.4) modified for rapid weakening. The the additional term in the hyperbolic sine changes the slip rate dependence at high slip rates to match the additional factor  $(1 + V_{ss}/V_W)^{-1}$  in the DR flash heating law at steady-state. As in the FV law without rapid weakening, the STZs distinguish between locked and slipping solutions to the constitutive equations. The variable  $m_{RW}$  is introduced to either lock the fault or set the STZ populations to their steady-state value. For the rapid weakening FV law the variable  $m_{RW}$  is given by:

$$m_{RW} = \begin{cases} 1, & [\tau \leq \tau_0 \exp (\chi_h / \chi) - \frac{R_c}{\alpha V_W} \exp (-\chi_c / \chi)]; \\ \tau_0 \exp (\chi_h / \chi) / \left[ \tau + \frac{R_c}{\alpha V_W} \exp (-\chi_c / \chi) \right], & \\ \tau_0 \exp (\chi_h / \chi) - \frac{R_c}{\alpha V_W} \exp (-\chi_c / \chi). & [\tau > \tau_0 \exp (\chi_h / \chi) - \frac{R_c}{\alpha V_W} \exp (-\chi_c / \chi)]. \end{cases} \quad (4.21)$$

## CHAPTER 4. COMPARING FRICTION LAWS IN DYNAMIC RUPTURE

The variable  $m_{RW}$  sets the STZs to their steady-state value when the fault is slipping, and locks the fault below the yield stress.

In addition to modifying the steady-state velocity dependence to account for rapid weakening, the alterations to the FV law have the advantage of preventing the free volume from diverging at high slip rates so that unlike the original FV law, the rapid weakening version has steady-state solutions for all slip velocities. The length scale  $L_{FV}$  increases with slip velocity as before.

Friction parameters used in rapid weakening simulations are listed in Table 4.2. For both laws, rapid weakening leads to a decrease in the critical cell size  $h^*$  due to increased  $B - A$  at high slip rates, so numerically stable simulations require a smaller grid spacing.

Figure 4.8 shows the time histories of slip velocity, shear stress, and the appropriate state variable for anti-plane ruptures governed by the rapid weakening FV and DR laws. Each quantity is measured at a point 1.5 km from the hypocenter on a 6 km long fault. A low loading stress  $\tau_{\text{load}} = 22$  MPa promotes rupture in the form of a self-healing slip pulse for both choices of the constitutive law. A brief pulse of rapid slip heals and quickly recovers shear stress once the fault locks. We note that the free volume dilates more rapidly than the FV law without rapid weakening, and the free volume has little variation over a large range of slip velocities.

A plot of shear stress as a function of slip for each law at a point 1.5 km from the hypocenter is shown in Figure 4.9. As before the DR law, now with flash heating, differs from the FV law, now with rapid weakening, in the slip rate dependence of the length scale  $L_{FV}$  in contrast to the constant  $L_{DR}$ . Parameters are selected for equal slip in ruptures with each law. When slip is fixed in this manner the DR law dissipates more frictional energy. As with the ruptures without rapid weakening, the FV law requires additional slip to weaken to its minimum shear stress. The nucleation length is smaller for the FV law, so the DR flash heating law requires an increase in the DR  $b$  parameter for both laws to permit rupture for an identical initial shear load.

Snapshots of the slip rate as a function of position along strike for an anti-plane rupture with the rapid weakening FV law are shown in Figure 4.10. This illustrates how the rupture grows in both space and time. The plots indicate that the rupture starts out as a crack-like rupture before it transitions to a self-healing pulse-like rupture. The DR law with flash heating produces ruptures with similar slip rates and pulse spatial widths, although the slipping front takes longer to reach the fault boundary than in the FV law with rapid weakening.

For in-plane ruptures, the initial shear load determines whether the earthquake ruptures as a self-healing pulse, an expanding crack limited by the Rayleigh wave

CHAPTER 4. COMPARING FRICTION LAWS IN DYNAMIC RUPTURE

Table 4.2: Parameters for DR and FV law dynamic ruptures with rapid weakening. Symbols for the shared model parameters are defined in Table 4.1, except for the characteristic rapid weakening velocity  $V_W$ .

| Rapid Weakening Simulation Parameters |                           |
|---------------------------------------|---------------------------|
| Shared Parameters                     |                           |
| $dl = 0.004$ km                       |                           |
| $nx = 2048$                           |                           |
| $\mu = 32.03812032$ GPa               |                           |
| $c_s = 3.464$ km/s                    |                           |
| $\nu = 0.25$                          |                           |
| cfl = 0.3                             |                           |
| $L_{\text{fault}} = 6$ km             |                           |
| $L_{\text{trigg}} = 1.3$ km           |                           |
| $\tau_{\text{load}} = 22$ MPa         |                           |
| $\tau_{\text{trigg}} = 74$ MPa        |                           |
| $V_W = 1$ m/s                         |                           |
| FV Law                                | DR Law                    |
| $\chi_s = 0.3407$                     | $L_{\text{DR}} = 50$ mm   |
| $\sigma_d = 0.25$ MPa                 | $a = 0.0027$              |
| $\chi_c = 0.1145$                     | $b = 0.017$               |
| $f_* = 222.3$                         | $f_0 = 0.7$               |
| $V_* = 10^{-6}$ m/s                   | $V_0 = 10^{-6}$ m/s       |
| $R_c = 5$ s $^{-1}$                   | $\sigma = 100$ MPa        |
| $\alpha = 0.0005$ (MPa m) $^{-1}$     | $V_1 = 10^{-6}$ m/s       |
| $\chi_h = 0.0028$ m                   |                           |
| $\tau_0 = 44.12$ MPa                  |                           |
| $\chi(t = 0) = 0.0061$                | $\theta(t = 0) = 50000$ s |

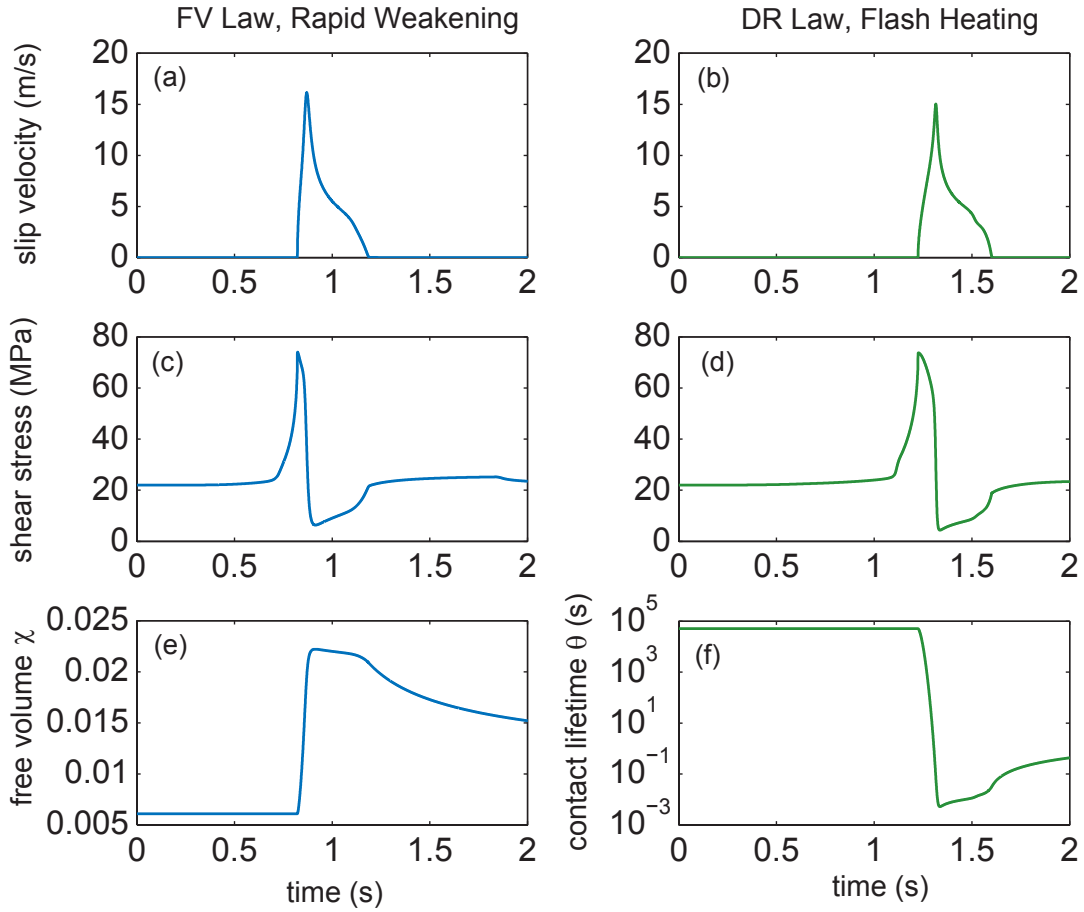


Figure 4.8: Fault dynamics for rapid weakening friction models. (a-d) Both laws rupture as self-healing pulses with low initial loading stresses. The slip rates are larger than with the laws without rapid weakening. (e) Because the evolution equation for the free volume depends on the stress (Equation (4.4)), rapid weakening alters the free volume dynamics. After a rapid period of dilation, free volume varies little over a wide range of slip velocities before the fault heals and compaction begins. (f) State variable evolution for the DR law with flash heating. The contact lifetime drops rapidly with the arrival of the rupture, and increases with time once the fault heals to regain frictional strength. Parameters for these anti-plane simulations are given in Table 4.2.

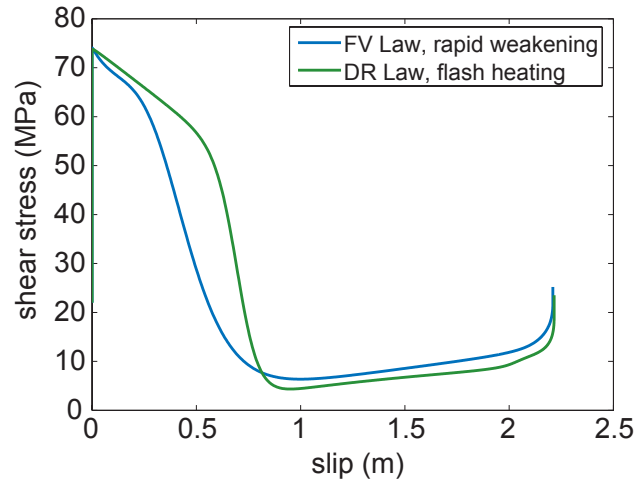


Figure 4.9: Shear stress as a function of slip for anti-plane dynamic ruptures with the rapid weakening friction laws. Parameters were selected for each pulse to yield the same net slip (the DR law dissipates more energy in frictional sliding). As with the laws without rapid weakening, the FV law weakens more rapidly with initial slip, and more gradually during rapid slip. Matching slip between the laws requires a significantly larger value of  $L_{DR}$  than in ruptures without rapid weakening. As a consequence, the DR  $b$  parameter must be increased to give the two laws comparable nucleation lengths. Without this change, the flash heating model will not rupture with identical initial shear loads. Parameters for these simulations are given in Table 4.2.

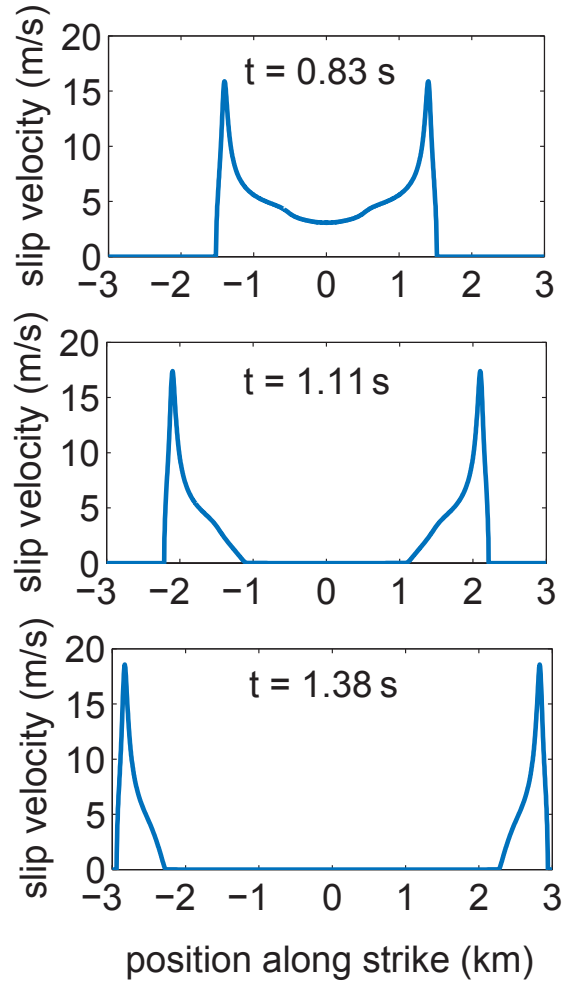


Figure 4.10: Snapshots of slip velocity as a function of position for anti-plane rupture with the rapid weakening FV law. The slip rate is shown at three different times, illustrating how the rupture evolves in both space and time. In the top plot, slip is propagating as an expanding crack. As time progresses in the subsequent plots, slip ceases in the center of the fault and the rupture continues as an expanding pulse. The slip velocity evolves in a similar manner for the DR law with flash heating, though the rupture is slower to advance out to the ends of the fault. Parameters for this simulation is given in Table 4.2.

## CHAPTER 4. COMPARING FRICTION LAWS IN DYNAMIC RUPTURE

speed, or a supershear crack. The diagram in Figure 4.11 shows which mode occurs as a function of the initial shear load and frictional energy dissipation for the FV and DR laws with rapid weakening. The frictional energy dissipated per area in the first meter of slip at a point 1.5 km from the hypocenter is plotted on the horizontal axis, and the initial shear load is plotted on the vertical axis. Results for the FV (DR) law are plotted as plusses (squares) for the sub-Rayleigh/supershear transition and circles (triangles) for the crack/pulse transition. Each point on the plot corresponds to the smallest initial stress permitting supershear crack propagation for the sub-Rayleigh/supershear transition, or the smallest initial stress for which pulse-like rupture is not observed for the crack/pulse transition.

For the lowest stresses, pulse-like rupture limited by the Rayleigh wave speed occurs. The stress at which the ruptures transition from pulses to expanding cracks is independent of the amount of frictional dissipation within a given law. However, the DR law requires a smaller initial shear stress to rupture as a self-healing pulse, despite the fact that the two laws have identical velocity weakening in steady-state. The difference arises because the DR law attains a lower dynamic sliding stress (Figure 4.9). The dynamic friction determines the initial shear stress at which the transition to pulse-like rupture occurs [19]. Here the steady-state velocity weakening rate in the friction law is of primary importance, as the DR and FV rapid weakening laws both transition to pulse-like rupture at similar stresses. However, because the functional form of the steady-state velocity weakening is identical in the FV and DR rapid weakening laws, the difference in the initial stresses at which the crack/pulse transition occurs in Figure 4.11 is due to the stress weakening differently with slip in the two friction laws.

At intermediate values of the initial load a sub-Rayleigh expanding crack solution exists. At higher stresses the crack transitions to supershear rupture velocities. Both the FV and DR rapid weakening laws show that the stress at which the transition to supershear occurs depends on the amount of frictional dissipation. Comparing the two laws, the sub-Rayleigh/supershear transition appears nearly identical on the scale of Figure 4.11, with approximately 0.5 MPa difference between the curves (similar to the difference in the sub-Rayleigh/supershear transition for the laws without rapid weakening, Figure 4.7, where the difference appears more pronounced because of the expanded scale). This is partly due to increasing the DR  $b$  parameter to decrease the nucleation length in the DR rapid weakening law, which diminishes the nucleation length discrepancy relative to that in the laws without rapid weakening. However, we note that for the laws without rapid weakening, the faults are loaded within several MPa of failure. Therefore, a difference of 0.5 MPa in the initial load is a significant fraction of the strength excess, and the strength excess is crucial in determining if a rupture can transition

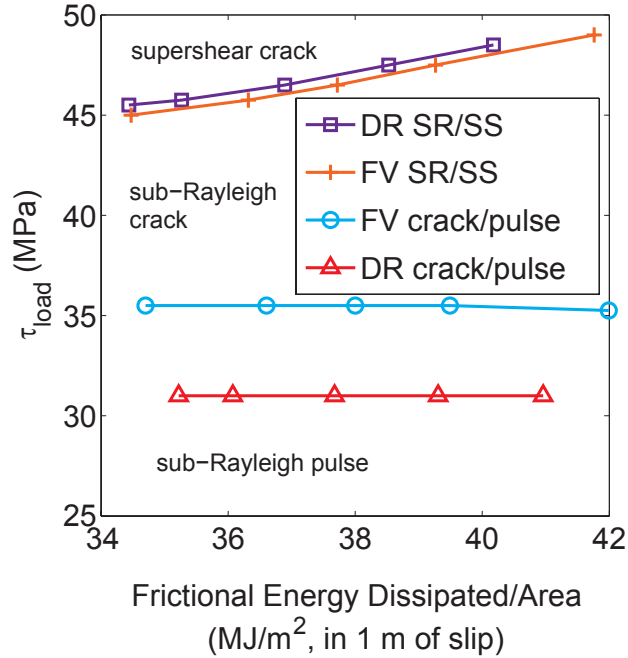


Figure 4.11: Rupture type diagram for in-plane ruptures with rapid weakening. Points on the plot indicate the smallest initial shear stress for which supershear rupture or sub-Rayleigh crack-like rupture is observed on the fault for a given amount of energy dissipated to friction. Above the sub-Rayleigh/supershear (SR/SS) transition, the rupture is a supershear crack. Below the crack/pulse transition line, the rupture is a sub-Rayleigh pulse. Between the two lines, the rupture is a sub-Rayleigh crack. The crack/pulse transition is independent of the frictional energy dissipated for a given law, consistent with the anti-plane study of Zheng and Rice [19]. However, we note that the DR law requires lower initial loads for pulse-like rupture than the FV law despite identical steady-state velocity weakening. The sub-Rayleigh/supershear transition depends on the specifics of frictional dissipation, with only a slight difference between the DR and FV laws. Parameters are the same as in Table 4.2 except for the initial loading stress  $\tau_{\text{load}}$  and the friction parameters  $\alpha$  and  $R_c$  for the FV law or  $l$  and  $\theta(t=0)$  for the DR law, which are varied in the simulations.

to supershear. For the laws with rapid weakening, the fault is loaded tens of MPa from failure, and a difference of 0.5 MPa in the initial load is less important. The vertical scale on each of the plots reflect this difference in the strength excess between the laws with or without rapid weakening (the scale in Figure 4.7 is about 10 times smaller than the scale in Figure 4.11).

The rupture type plot indicates that when comparing the DR and FV rapid weakening laws, the most significant difference is associated with how the shear stress weakens with slip and not the nucleation length. The distinct forms in which stress weakens with slip for the FV and DR laws results in an increase of 4 MPa in the stress at which the crack/pulse transition occurs for the FV law with rapid weakening compared to the DR law with rapid weakening. The DR law with rapid weakening has a larger nucleation length, but the difference is small enough that the sub-Rayleigh/supershear transition occurs at roughly the same initial stress relative to the strength excess in rapid weakening laws.

## 4.5 Discussion

Our comparisons between the FV law, DR law, and SW law show that the slip rate dependence of  $L_{FV}$  impacts many properties of dynamic ruptures. These properties include the manner in which stress weakens with slip, the peak slip rate attained during rupture, and the stress at which supershear rupture is nucleated. The slip rate dependence of  $L_{FV}$  is also important in ruptures with constitutive laws that are modified to allow rapid weakening. The rapid weakening laws result in dynamic ruptures that are self-healing pulses with low initial shear stress which transition to pulse-like rupture at different initial shear stresses for the FV and DR laws with rapid weakening.

Because friction laws have implications at all scales of earthquake rupture, we discuss our results in the context of these various scales. At each scale of the earthquake problem there are uncertainties and modeling challenges. A primary objective of those working on earthquake source physics is to use mechanisms and constraints from statistical physics, material science, and rock mechanics to reduce the uncertainty and produce sharper bounds on the range of behavior that might be observed. However, even under controlled laboratory conditions friction, fracture, and deformation remain active areas of research and lack a complete microscopic description. Our hope is that a multiscale approach that investigates macroscopic consequences in parallel with microscopic mechanisms will provide insights spanning a broad range of scales.

At the scale of faults, friction laws control the complexity of individual ruptures

## CHAPTER 4. COMPARING FRICTION LAWS IN DYNAMIC RUPTURE

and the associated ground motion. Models of the earthquake source are complicated by uncertainties involving the stress level on earthquake faults [114, 115], how shear stress weakens with slip during rupture [116], and the energy balance of faulting [117]. Additionally, while earthquake records have been inverted for constitutive parameters [55, 118], these studies estimate slip-weakening distances that are much larger than the total slip in smaller earthquakes ( $d_c$  of order 1 m in Figure 1.2.1(b)). This makes it difficult to estimate the correct constitutive parameters. Comparing friction laws in the context of earthquake ruptures helps determine what macroscopic observables, such as peak ground velocity and radiated seismic energy, can be affected by these uncertainties. The FV law and the DR law produce different peak slip rates in our calculations. This will likely affect the peak ground velocity predicted in the vicinity of the fault for each law [119]. Additionally, our modeling indicates that the FV law and DR law transition to supershear at different shear loads for a given frictional dissipation. Supershear rupture velocities radiate shear waves that do not attenuate with distance from the fault [49], and thus supershear rupture can affect the spatial extent of regions with high ground velocities.

On a smaller scale, the aggregate behavior of gouge influences the dynamics of friction. This scale can be studied in the laboratory and through numerical simulations. The FV law ties weakening and re-strengthening to dilation and compaction, and predicts a slip rate dependence of  $L_{FV}$  that is absent in the DR law. The FV law closely matches the slip rate dependence of  $L$  observed by Mair and Marone [34] for sheared granular layers. For bare granite surfaces, little variation in  $L$  is observed over slip rates ranging from  $10^{-2}$  to  $10^{3.5}$   $\mu\text{m/s}$  by Blanpied *et al.* [120]. Because the rate dependence of the length scale  $L_{FV}$  is due to dilation, the amount of dilation of the sheared layer determines how much variation in the length scale will occur. The Blanpied *et al.* experiments use relatively smooth granite surfaces, which dilate less than a rough surface or a layer of gouge. The FV law would thus predict less variation in the length scale  $L_{FV}$  for these experiments. Dilation with increasing slip rate is observed in rock mechanics experiments [96, 34] and boundary lubrication experiments [85]. However, the dilatancy of real faults during rapid seismic slip is unknown. Large overburden pressures may not allow for significant dilation. Previous studies have added observed laboratory porosity evolution to the DR framework [65, 121]. The FV law differs from other models of dilation and compaction in that it ties velocity weakening directly to dilation and compaction of the gouge layer. The porosity models in the DR framework maintain a length scale that does not vary with slip rate, which is different than the evolution predicted by the FV law. In numerical studies, STZ theory compares favorably with molecular dynamics simulations of

## CHAPTER 4. COMPARING FRICTION LAWS IN DYNAMIC RUPTURE

amorphous materials [24, 25] and with contact dynamics simulations of granular materials [27].

At the smallest scales, individual grain contacts and associated wear, heating, fracture and deformation determine the most basic interactions for fault friction. Establishing the physical interactions that are the most important at the high pressures and slip rates of earthquake rupture is an active area of research in earthquake source physics. Because the physics of granular and amorphous systems are not fully understood, determining the consequences of these microscopic interactions for earthquake rupture remains a challenge. The FV law begins with a more microscopic picture than other constitutive laws, though many of the possible more complicated microscopic features are still ignored. Fault zones contain pore fluids, which influence fault healing [122], and can become pressurized due to shear heating [123]. How contacts adhere, heal, and regain strength has tremendous implications for fault re-strengthening and earthquake recurrence over a broad range of temporal scales [63, 124, 125] – a granular description of fault gouge where only contact forces are relevant is only the beginning of a microscopic description of fault zones. We expect many of these other effects will be important, especially on the time scale of earthquake recurrence. STZ Theory was initially formulated in the context of amorphous solids with more complicated particle interactions than those which arise for granular materials [24, 25]. Interestingly, the STZ equations which describe the other amorphous materials are the same as those for granular materials, suggesting that there are at least some features in this class of systems which may be universal. However, none of these theories incorporate the full range of complex interactions which are likely to occur in gouge. While the FV law begins to link microscopic physics to fault scale behavior, the greater variety of grain-scale physics need to be incorporated into future constitutive models to fully capture the complex dynamics occurring in fault zones during the seismic cycle.

# Chapter 5

## Strain Localization in Dynamic Rupture

We continue to investigate the fault scale implications of STZ Theory in this chapter by extending our fault scale earthquake models to resolve gouge scale strain localization. This is a challenging multi-scale problem that quantifies the fault scale effect of the small scale physical process of localization. In this chapter, we make comparisons between ruptures governed by STZ Theory with homogeneous strain and ruptures governed by STZ Theory where strain spontaneously localized to a narrow shear band. We also study the dynamics of localization in the fault gouge, and examine the role that localization plays in fault scale rupture propagation.

The research in this chapter that compares homogeneous shear with localized shear in dynamic earthquake rupture is work that is published by Daub, Manning, and Carlson in *Geophysical Research Letters* [57].

### 5.1 Earthquake Rupture and Strain Localization

The earthquake rupture problem spans a wide range of length and time scales, from microscopic contacts between individual grains through complex networks of faults. The basic interactions at the smallest scales form the basis for larger scale behavior. Modeling earthquake rupture is therefore extremely challenging, as models must capture the essential physics at a given scale and determine how larger scales are affected by the smaller scale physics. Because the friction law is usually the only ingredient in an earthquake model that accounts for small scale physics, developing constitutive laws that efficiently incorporate physical processes

is essential for improving our understanding of the physics of the earthquake source.

Here, we focus on the implications of a constitutive law that accounts for the small scale process of strain localization in the granular fault cores of earthquake faults. In our model, a shear band that is narrow even on the scale of the fault gouge spontaneously forms due to fault slip. Localization of strain is observed in many studies of faulting, including numerical simulations [30], laboratory experiments [33], and field observations of exhumed faults [37]. The prevalence of shear bands in many studies indicates that localization widely affects faults.

Constitutive laws used in dynamic rupture models usually do not explicitly account for localization. Traditionally, dynamic rupture is modeled on a planar fault with a slip-weakening [1, 2, 3] or rate and state friction law [10, 11], where the fault strength depends only on a single state variable. We include localization in our modeling by resolving the dynamic evolution of the strain rate on a spatial grid that spans the width of the fault core. In our model, the fault dynamically selects how to distribute strain within the fault core, and can accommodate both broad and localized shear within the slip history of a single earthquake. This approach allows us to investigate the fault scale consequences of the dynamics of shear localization.

## 5.2 Modeling Dynamic Ruptures with Localization

Modeling dynamic rupture with strain localization is a challenging multi-scale problem. A simplified illustration of the range of scales in the earthquake problem is shown in Figure 5.1. The fault consists of a layer of gouge sheared between elastic rock (left in Figure 5.1). Within the layer of fault gouge, deformation tends to spontaneously localize into narrow shear bands, as shown in the center picture in Figure 5.1. At the grain scale, the gouge deforms plastically when groups of particles rearrange (right, Figure 5.1). The STZ model captures the plastic deformation at the grain and gouge scales, and also acts as a friction law that describes fault scale behavior in elastodynamic rupture simulations. The STZ equations and their microscopic basis are discussed in Chapter 2.

A more detailed illustration of the fault that we model is shown in Figure 5.2. The left picture shows a side view of the fault plane. We assume that slip does not vary in the  $y$ -direction, and that slip occurs only in the  $x$ -direction. The right picture shows a top view of the fault. A layer of gouge of half width  $w$ , which is described by STZ Theory, is sheared between elastic rock. The inset shows a

CHAPTER 5. STRAIN LOCALIZATION IN DYNAMIC RUPTURE

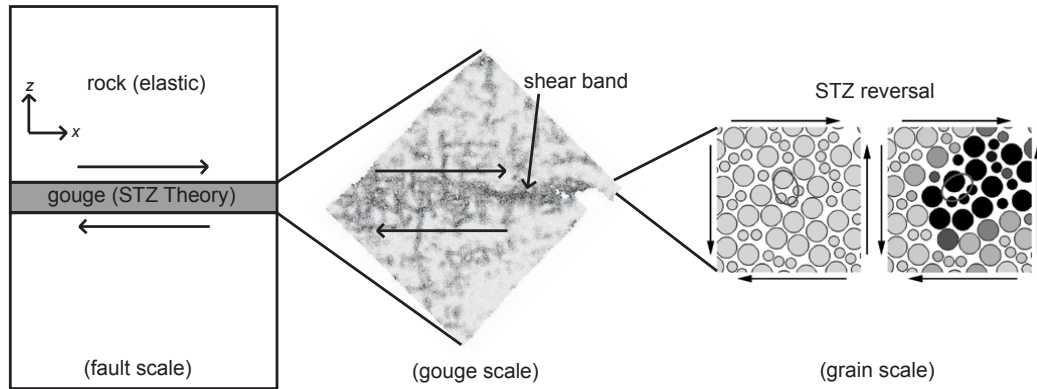


Figure 5.1: Diagram illustrating the multi-scale nature of the earthquake rupture problem. The system progressively decreases in scale from left to right. (left) Fault scale, with a thin layer of fault gouge sheared between elastic rocks. (center) Deformation within the fault gouge, where a shear band that is much narrower than the gouge thickness accommodates plastic strain in the gouge. Shear band image taken from Falk and Shi [26] and reoriented to match the sense of shear of the fault and grains. (right) Individual rearrangements occur at the grain scale and produce plastic strain in the fault gouge. The left grain scale picture shows a “positive” STZ orientation, and as the grains are sheared the gouge deforms plastically and the particles change to a “negative” orientation in the right grain picture. STZ diagram taken from Falk and Langer [24] (Reprinted with permission. Copyright 1998 by the American Physical Society. <http://link.aps.org/abstract/PRE/v57/p7192>).

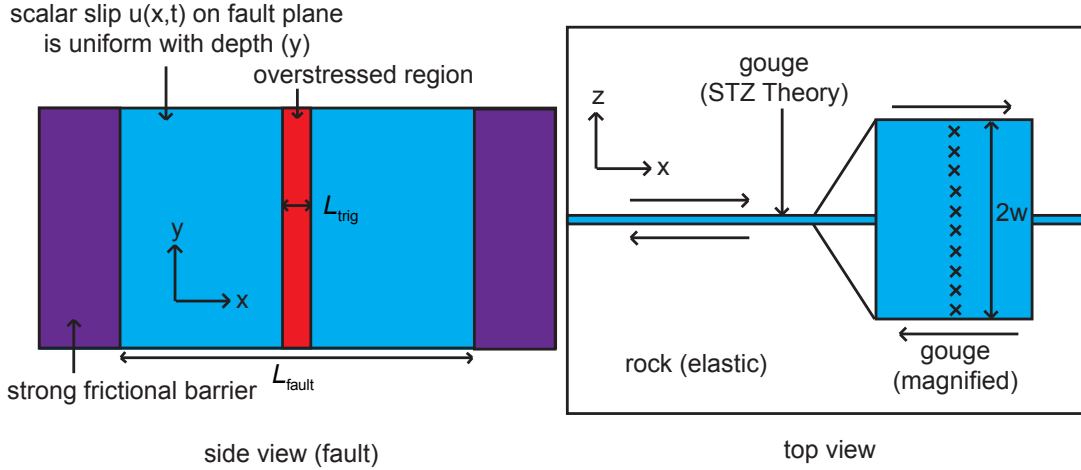


Figure 5.2: Diagram illustrating the fault in the dynamic rupture model. (left) Side view of the fault plane. Slip is assumed to be uniform with depth. The triggering patch (red) initiates slip, and the rupture spontaneously propagates along strike through the light gray region before it hits the strong barriers (purple) to stop the rupture. (right) Top view of the fault. A thin layer of fault gouge, which is described by STZ Theory, is sheared between elastic rock. Within the fault gouge, we resolve the dynamic evolution of the effective temperature across its width (inset). The effective temperature evolves independently at each position along strike, and dynamic fault slip at each point drives the process of strain localization in the model.

close up of the fault gouge, where the spatial grid in the  $z$ -direction resolves the dynamic evolution of the effective temperature in response to fault slip.

The elastodynamic response of the surrounding rock is modeled using a boundary integral method [98, 88, 99], 1995]. In the boundary integral method, the shear stress  $\tau$  on the fault can be written

$$\tau(x, t) = \tau_0(x) + \phi(x, t) - \frac{\mu}{2c_s} V(x, t). \quad (5.1)$$

The total shear stress on the fault is the combination of three terms: the initial shear stress on the fault  $\tau_0(x)$ , the stress transfer functional  $\phi(x, t)$ , and radiation damping. The stress transfer functional accounts for all dynamic stress changes due to prior slip on the fault, and is calculated using FFTs. We note that although the radiation damping term is explicitly written out in Equation (5.1), the full dynamic response is accounted for with this method.

CHAPTER 5. STRAIN LOCALIZATION IN DYNAMIC RUPTURE

Table 5.1: Parameter descriptions and their values in the STZ model.

|                           |   |
|---------------------------|---|
| $t_0 = 0.000001$ s        | STZ rearrangement time scale  |
| $\epsilon = 10$           | Strain increment for STZ rearrangement  |
| $f_0 = 40$                | STZ activation energy scaled by thermal energy                                |
| $\sigma_d = 0.5$ MPa      | STZ activation stress (also known as the direct effect stress)                |
| $\tau_y = 25$ MPa         | STZ yield stress  |
| $c_0 = 400$               | Effective temperature specific heat   |
| $\chi_w = 0.2$            | Effective temperature activation barrier                                      |
| $q_0 = 0.08$              | Nondimensional strain rate ( $\dot{\gamma}t_0$ ) where STZ Theory breaks down |
| $R_0 = 5$ s <sup>-1</sup> | Inverse of STZ relaxation time scale  |
| $\beta = 0.1$             | STZ relaxation activation barrier   |
| $\chi_0 = 0.007$          | Lowest effective temperature that can be reached by relaxation                |
| $D = \text{varies}$       | Squared diffusion length scale  |

This approach resolves the localization at the gouge scale, but because the model is a continuum approximation for the gouge deformation, it can be solved simultaneously with the elastodynamic equation at the fault scale. The elastodynamic equation (Equation 5.1) provides a relationship between the shear stress  $\tau$  and the slip rate  $V$ . The plastic strain rate integrated over the gouge width also gives a relationship between the shear stress and the slip rate:

$$V = \int_{-w}^w \dot{\gamma} dz = f(\tau) \int_{-w}^w \exp(-1/\chi) dz. \quad (5.2)$$

These two equations are solved simultaneously for the shear stress and slip rate at every point on the fault, along with the dynamic evolution of the slip and the effective temperature. Table 5.1 lists the parameters in the STZ friction law, and the values that we use in our simulations.

The geometry we study allows for both supershear and sub-Rayleigh propagation speeds. For simplicity, we assume that the friction parameters and initial conditions for the effective temperature do not vary along strike ( $x$ -direction). Additionally, the initial shear stress is uniform along strike ( $\tau_0(x) = \tau_0$ ) with the exception of a triggering patch of width  $L_{\text{trig}}$  where the stress is elevated to  $\tau_{\text{trig}}$  to nucleate rupture. Strong barriers with a large yield stress  $\tau_y$  stop the rupture once it reaches the edge of the fault. The effective temperature is symmetric about  $z = 0$ , so we only solve for the effective temperature in one half of the gouge layer.

To solve the partial differential equation for the effective temperature, we

CHAPTER 5. STRAIN LOCALIZATION IN DYNAMIC RUPTURE

Table 5.2: Elastodynamic parameters in rupture simulations.

|                                  |   |
|----------------------------------|---|
| $\mu = 32.03812032$ GPa          | Shear modulus   |
| $c_s = 3.464$ km/s               | Shear wave speed  |
| $\nu = 0.25$                     | Poisson's ratio   |
| $L_{\text{fault}} = 8$ km        | Length of fault that can rupture  |
| $L_{\text{trigg}} = 1$ km        | Length of triggering patch  |
| $\tau_{\text{trigg}} = 67.5$ MPa | Triggering stress   |
| $dl = 0.005$ km                  | Grid spacing in the $x$ -direction  |
| $nx = 2048$                      | Number of grid points in the $x$ -direction                                   |
| $\text{cfl} = 0.3$               | Courant-Friedrichs-Lewy Ratio $\text{cfl} = c_s dt/dl$                        |
| $w = 0.1$ m                      | Half width of fault gouge layer   |
| $nz = 101$                       | Number of $z$ -direction grid points spanning half width of gouge             |
| $dz = 0.001$ m                   | Grid spacing in $z$ -direction  |
| $n_{\text{sub}} = 10$            | Substeps within elastodynamic time step for effective temperature integration |
| $\tau_0 = \text{varies}$         | Initial shear stress  |

approximate the spatial derivatives in the effective temperature evolution with central, second order finite differences. Our finite difference scheme separates the diffusion term into two terms, and the differences are computed on a spatial grid in the  $z$ -direction spanning the half width of the gouge. The stress is assumed to be constant across the gouge, which means that the spatial variation of the effective temperature determines how strain localizes within the fault core.

Our time integration scheme treats the effective temperature derivatives in the diffusion term implicitly, and treats the energy dissipation and relaxation terms explicitly. The energy dissipation term must be treated explicitly in the boundary integral method due to its dependence on the strain rate. The diffusion constant, due to its dependence on the strain rate, must also be treated explicitly. Because of this, the time steps must be small enough to resolve the evolution of the strain rate to determine the correct diffusion time scale. Because the effective temperature (and therefore the strain rate) evolve on a time scale faster than the time for seismic waves to propagate along the fault, our time integration scheme involves taking  $n_{\text{sub}}$  substeps within an elastodynamic time step to integrate the effective temperature stably, as done in Noda, Dunham, and Rice [126]. The elastodynamic parameters for our simulations are listed in Table 5.2.

As with the smaller scale numerical investigation of friction dynamics, the effective temperature initial conditions determine the subsequent evolution of strain

rate in the gouge. If the initial effective temperature is spatially uniform across the width of the gouge ( $z$ -direction), we refer to the rupture as “homogeneous.” Homogeneous only refers to the strain rate across the width of the gouge at any one spatial point – the effective temperature varies along strike as it evolves in response to slip on the fault, and it is also time dependent. The spatially uniform initial effective temperature in our simulations is identical to the initial effective temperature in the investigation of friction dynamics (Section 2.5),  $\chi(t = 0) = 0.009$ .

If the initial effective temperature includes a small perturbation identical to the perturbation in the investigation of friction dynamics (Section 2.5), then we refer to the rupture as “localized.” This means that at any given position, the strain rate can vary across the width of the gouge due to the evolution of the effective temperature. The strain rate profile also varies along strike, as the effective temperature evolves due to rupture propagation. At any given time, there are both spatial points that have not ruptured that still match the initial conditions, as well as points that are actively slipping, where the strain rate profile is determined by the effective temperature evolution.

Additionally, for “localized” ruptures, we examine a variety of different diffusion constants. If the diffusion length scale ( $\sqrt{D}$ ) is smaller than the half width of the gouge  $w$ , then a shear band that is narrow on the scale of the gouge forms. This case is referred to as a “narrow shear band.” If the diffusion length scale is of the order of the half width of the gouge or larger, then the shear band that forms fills the entire width of the gouge. This case is referred to as a “broad shear band.”

### 5.3 Comparing Localized and Homogeneous Ruptures

First, we examine how strain localization alters rupture propagation relative to a homogeneous rupture. A plot comparing how stress weakens with slip for a homogeneous rupture and a localized rupture is shown in Fig. 5.3(a). The shear band width dynamically selected by the effective temperature is 10% of the total gouge width  $2w$ . During the initial stages of slip, the curves are indistinguishable. For the later stages of slip, shear stress weakens much more rapidly due to the dynamic instability of localization, increasing the stress drop. Homogeneous deformation and dynamic localization produce very different slip rates, as can be seen in Fig. 5.3(b). The rupture front arrives earlier and has a higher peak slip rate when strain localization occurs.

To illustrate the importance of the dynamic instability, we contrast our results

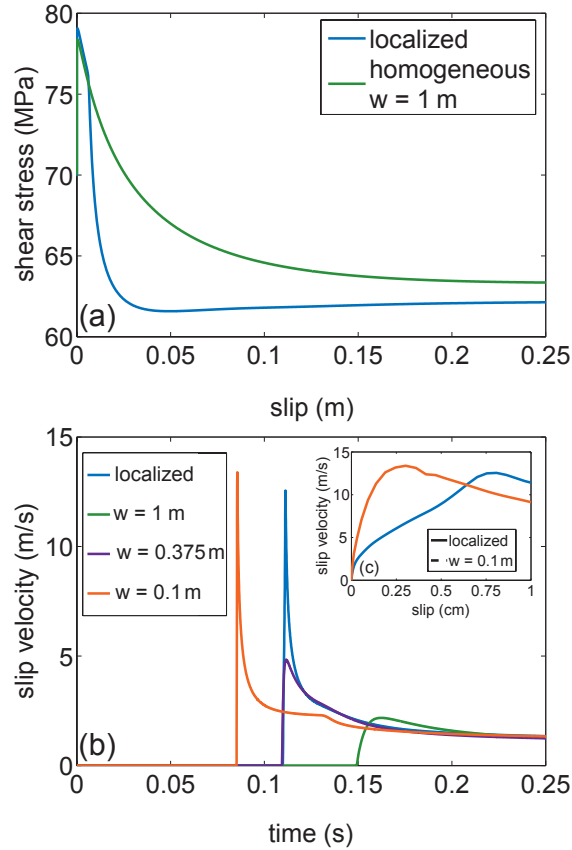


Figure 5.3: Dynamic rupture evolution at a point 0.35 km from the hypocenter. (a) Comparison of shear stress as a function of slip. Dynamic localization of deformation produces dynamic weakening not observed with the rupture with homogeneous strain. (b) Plot of slip rate as a function of time. The dynamic strain localization rupture is compared with a host of models with homogeneous strain. None of the values of the imposed gouge width  $w$  can match both the peak slip rate and rupture front arrival of the rupture with localized strain. (c) Inset: Slip rate as a function of slip for the localized and narrowest width homogeneous rupture. The more rapid acceleration of slip in the narrowest homogeneous rupture is distinct from the localized model.

for localized shear with two additional homogeneous ruptures of different fixed gouge widths  $w$  chosen to match particular aspects of the localized rupture. Slip velocity as a function of time is plotted at a point 0.35 km from the hypocenter for all models in Fig. 5.3(b). The properties that we compare are the peak slip velocity and the time at which slip initiates. The rupture front in the intermediate model ( $w = 0.375$  m) matches the arrival time of the localized rupture, but the peak slip rate is smaller. For the narrowest gouge thickness ( $w = 0.1$  m), we see peak slip rates similar to the localized rupture but earlier arrival. Figure 5.3(c) plots the slip rate as a function of slip for the homogeneous rupture with  $w = 0.1$  m and the localized rupture. This clearly shows that the initial broad deformation in the localized rupture does not simply delay the rupture, but also lessens the slip acceleration during the earliest stages of slip.

## 5.4 Dynamics of Localization

Now we examine the dynamics of localization in earthquake ruptures. Different shear band thicknesses form for localized ruptures with varying diffusion length scales. Shear band thicknesses ranges from broad shear bands that fill the entire gouge layer to narrow shear bands that are much narrower than the gouge width. The distinction between broad and narrow shear bands is important because localization is a mechanism for dynamic weakening. The narrower the shear band, the larger the strain rate in the shear band, and the lower the shear stress. We illustrate the effect of changing the diffusion constant in Figure 5.4. The plot shows the shear stress as a function of slip at a point 2 km from the hypocenter for four different values of the diffusion constant, as well as the same curve for a homogeneous rupture. The plot confirms that narrow shear bands increase the dynamic weakening due to localization, and decrease the sliding friction during earthquake rupture.

A plot of shear stress as a function of slip at a point 2 km from the hypocenter is shown in Figure 5.5. The shear stress weakens in two distinct phases. For slip less than 0.1 m, stress weakens gradually with slip. This corresponds to an approximately spatially uniform effective temperature, before the shear band grows rapidly. For slip between 0.1 m and 0.3 m, the stress drops rapidly due to the rapid growth of the shear band. Once the stress fully weakens, the stress increases due to re-strengthening. In this case, slip stops shortly before 0.7 m, and the fault heals.

The evolution of the effective temperature during dynamic rupture is similar to its evolution in the simple sheared layer of gouge. Snapshots of the effective

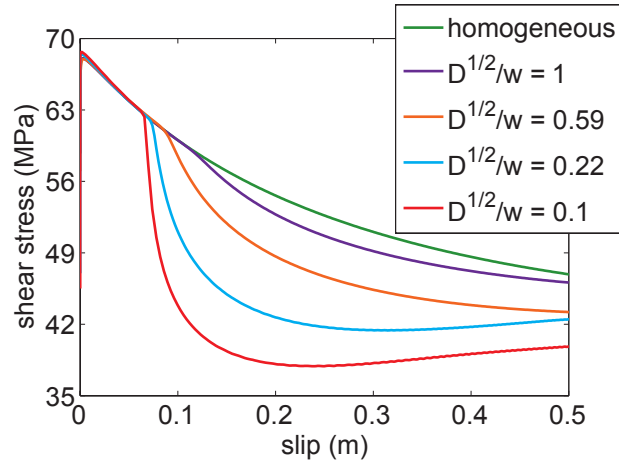


Figure 5.4: Plot of shear stress as a function of slip for varying diffusion constants scaled by the half-width of the fault gouge  $\sqrt{D}/w$  at a point on the fault 2 km from the hypocenter. In each case, the dynamically selected shear band width in the fault gouge is proportional to the effective temperature diffusion length scale. The uppermost curve is a “homogeneous” rupture for comparison, where the initial effective temperature is spatially uniform and no shear band forms. The other curves are all “localized” ruptures. The uppermost curve that includes diffusion ( $\sqrt{D}/w = 1$ ) is a “broad shear band,” as the diffusion length scale is equal to the gouge width. The lowermost curve is a “narrow shear band” with a diffusion length scale that is significantly smaller than the gouge half-width ( $\sqrt{D}/w = 0.1$ ). As the diffusion length scale decreases, the shear band becomes narrower, and the stress decreases more rapidly and reaches a lower value. The variation of stress as a function of slip with the diffusion length scale shows that strain localization is a mechanism for dynamic weakening.

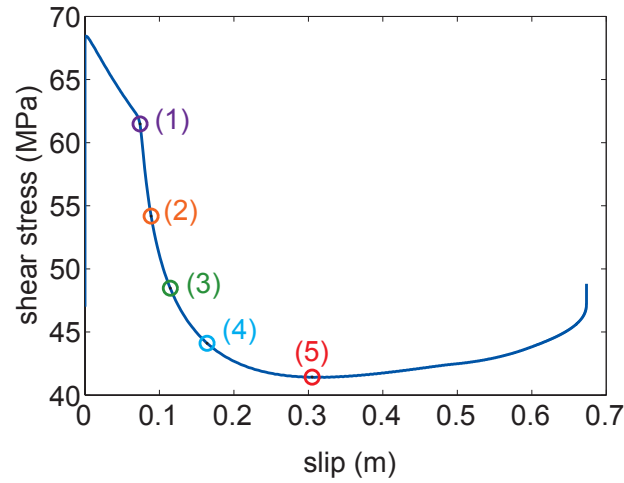


Figure 5.5: Plot of shear stress as a function of slip at a point on the fault 2 km from the hypocenter. The shear stress drops in two different stages. First is an early stage where the effective temperature is uniform in the fault gouge, which lasts for the first 0.1 m of slip. After about 0.1 m of slip, more rapid dynamic weakening occurs, which is coincident with the shear band formation. Once the stress decreases to its minimum value at 0.3 m of slip, the fault continues to slip and the stress gradually rises. Slightly before 0.7 m of slip is reached, slip ceases and the fault heals, which indicates that slip propagates as a self-healing pulse for these conditions. The diffusion constant in this simulation is  $\sqrt{D}/w = 0.2236$ , and the initial stress is  $\tau_0 = 47$  MPa.

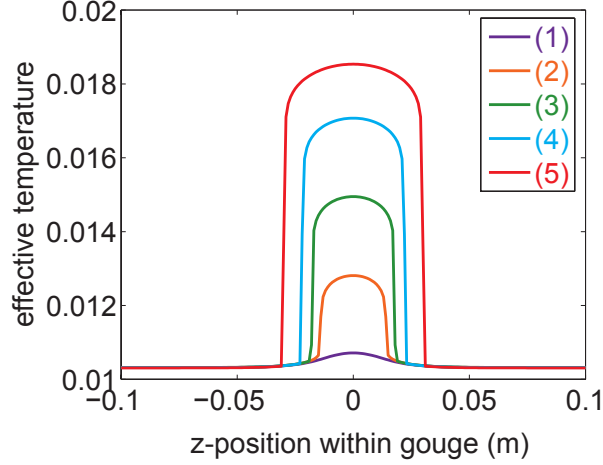


Figure 5.6: Plot of effective temperature as a function of  $z$ -position within the gouge at a point 2 km from the hypocenter at representative points shown in the stress versus slip plot (Figure 5.5). The horizontal range in this plot shows the entire gouge width in the simulation. The effective temperature is spatially uniform after 0.1 m of slip, at which point the feedbacks amplify the initial perturbation and a shear band forms. As slip propagates, the effective temperature increases and diffuses outwards. For slip beyond 0.3 m, the effective temperature decreases due to the relaxation term and maintains the width in curve (5). The diffusion constant in this simulation is  $\sqrt{D}/w = 0.2236$ , and the initial stress is  $\tau_0 = 47$  MPa.

temperature as a function of position within the gouge thickness at several points along the stress versus slip curve are shown in Figure 5.6. The earliest effective temperature plot shows that during the initial weakening phase of the stress versus slip curve, the gouge deforms approximately homogeneously. This is because the feedbacks in the effective temperature equation require time to amplify heterogeneity in the initial conditions. The duration of this phase of weakening is controlled by the magnitude of the initial perturbation to the effective temperature. Larger initial perturbations require less time to dynamically grow and shorten the amount of slip before the shear band forms.

As the effective temperature in the shear band increases, the shear stress in the gouge drops rapidly with increasing slip. The shear stress is lower because the strain rate is elevated in the shear band, and the STZ friction law weakens with strain rate. Additionally, the stress drops more rapidly because the relevant length scale for friction evolution is now the shear band width ( $\sim \sqrt{D}$ ) instead

of the half gouge width  $w$ . These two factors combine to significantly reduce the frictional dissipation on the fault during fault slip.

As the successive plots of the effective temperature show, the effective temperature in the shear band grows in magnitude, and the width of the shear band increases as the stress on the fault drops. The expanding width is due to the diffusion of effective temperature. The shear band reaches its maximum width when the stress reaches its minimum value, and the same shear band width is maintained for the duration of slip.

The rapid weakening of the shear stress coincides with the largest strain rates during rupture. Figure 5.7 shows strain rate profiles across the gouge width at several times during the weakening phase of dynamic rupture. The largest strain rates occur just as the shear band forms. This is because shear stress decreases most rapidly with slip at this time, releasing the most strain energy from the bulk. The strain rate at the center of the gouge decreases as the stress continues to drop with further slip, and the shear band broadens due to diffusion of the effective temperature. Because the slip rate is the strain rate integrated across the width of the gouge, the largest slip rates also occur when the stress decreases most rapidly with slip.

## 5.5 Fault Scale Rupture Propagation

At the scale of faults, ruptures can grow in space and time in a number of ways. Slip can propagate as an expanding crack, where points on the fault continue to slip after the rupture front arrives, or as a self-healing pulse, where at any given point the duration of slip is much shorter than the total time the fault is rupturing. Additionally, because we consider in-plane dynamic ruptures, the crack-like propagation mode can occur at sub-Rayleigh speeds or at supershear speeds. The initial stress is one factor determining the type of rupture growth – supershear rupture tends to occur at high initial stress, sub-Rayleigh rupture at intermediate initial stress, and pulse-like rupture at low initial stress.

The other important factor determining how slip propagates on a fault is the friction law – how much the fault weakens when it slips, and how much energy is dissipated on the fault. Here, we investigate the impact of strain localization on fault-scale rupture propagation. Because our simulations show localization decreases the frictional dissipation and reduces the shear stress, the width of the shear band in the gouge plays an important role in determining how slip propagates along the fault. We vary the diffusion length scale  $\sqrt{D}$ , which controls the degree of localization. Small values of the diffusion constant produce narrow

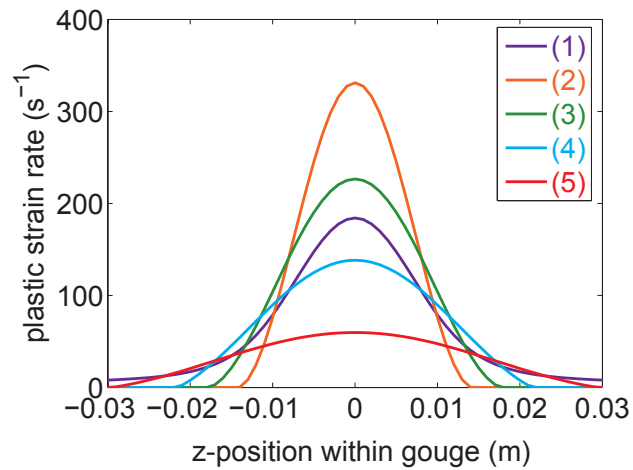


Figure 5.7: Plot of plastic strain rate as a function of position within the gouge at a point 2 km from the hypocenter at representative points shown in the stress versus slip plot (Figure 5.5). Note that the horizontal range in this plot is smaller than in Figure 5.6, as the strain rate is more sharply peaked than the effective temperature. The largest strain rate occurs early in the weakening process, as this is when the stress drops most rapidly with slip and releases elastic strain energy from the bulk at the largest rate. The diffusion constant in this simulation is  $\sqrt{D}/w = 0.2236$ , and the initial stress is  $\tau_0 = 47$  MPa.

## CHAPTER 5. STRAIN LOCALIZATION IN DYNAMIC RUPTURE

shear bands, while larger values of the diffusion constant produce broad shear bands. We vary the diffusion length scale  $\sqrt{D}$  over an order of magnitude, ranging from shear bands that diffuse to the full width of the gouge ( $\sqrt{D} = w$ ) to much narrower shear bands ( $\sqrt{D} = 0.1w$ ).

In the STZ constitutive model the fault never truly locks. The strain rate is zero only if the shear stress decreases to below the yield stress  $\tau_y$ . However, because fault healing results in the shear stress increasing with time, the stress cannot drop below the yield stress to cause fault slip to completely cease. We therefore define a pulse-like rupture when the slip rate at the center of the fault is three orders of magnitude smaller than the peak slip rate at the rupture front.

We illustrate the different ways that slip propagates on the fault for a value of the diffusion constant that allows for pulse-like rupture ( $D = 0.0005 \text{ m}^2$ ,  $\sqrt{D}/w = 0.2236$ ) in Figure 5.8. Pulse-like rupture does not occur for all values of the diffusion constant, only for smaller values that provide more dynamic weakening. If the initial stress is  $\tau_0 = 55.5 \text{ MPa}$ , then the rupture propagates as a supershear crack. Slip initiates ahead of the sub-Rayleigh crack tip and grows unstably, as the series of plots of slip rate as a function of position along strike illustrate.

If the initial stress is  $\tau_0 = 48.5 \text{ MPa}$ , fault slip occurs as an expanding sub-Rayleigh crack. In this series of snapshots of slip rate as a function of position, once slip initiates at a given point, the point continues to slip until the rupture reaches the boundary of the fault. This type of rupture occurs for intermediate values of the shear stress.

For lower values of the shear stress, rupture propagates as an expanding, self-healing pulse. This type of rupture is illustrated for  $\tau_0 = 47 \text{ MPa}$ . The rupture begins as an expanding crack as shown in the top plot of slip rate as a function of position along strike, but then slip stops in the center of the fault and the subsequent propagation is pulse-like. In this type of rupture, a given point slips for less time than the duration of the entire earthquake.

If the initial stress is too low, the dynamic rupture cannot propagate over the entire spatial extent of the fault. Arresting ruptures can be pulse-like, where the rupture transitions to pulse-like rupture but arrests before it reaches the fault boundary, or crack-like, where the rupture arrests while it is an expanding crack. An example of an arresting pulse and an example of an arresting crack are shown in Figure 5.8. While the slip rate as a function of position look similar for the two ruptures, the arresting pulse meets our criteria for pulse-like rupture while the arresting crack does not. The arresting pulse occurs for  $\tau_0 = 45.75 \text{ MPa}$ , and for even lower stresses the rupture arrests before the rupture becomes pulse-like ( $\tau_0 = 44.5 \text{ MPa}$ ).

We determine the range of stresses that produce each different type of rupture

CHAPTER 5. STRAIN LOCALIZATION IN DYNAMIC RUPTURE

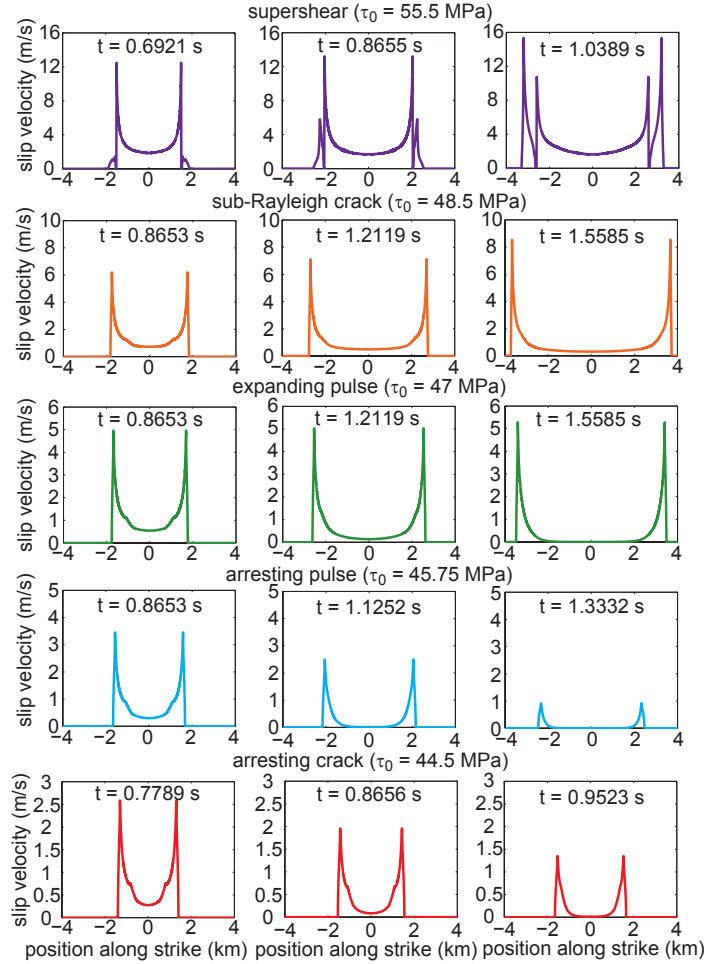


Figure 5.8: Snapshots of slip rate as a function of position along strike for the various types of rupture. The effective temperature diffusion constant in these simulation is  $\sqrt{D}/w = 0.2236$ . At the largest stress ( $\tau_0 = 55.5$  MPa), slip nucleates ahead of the rupture front and propagates faster than the shear wave speed. Crack-like rupture traveling sub-Rayleigh speeds occurs at an intermediate stress ( $\tau_0 = 48.5$  MPa). The rupture propagates as a self-healing pulse for lower shear stress, and can rupture the entire fault as a pulse ( $\tau_0 = 47$  MPa), or slip can arrest before the pulse reaches the edge of the fault ( $\tau_0 = 45.75$  MPa). For the lowest values of shear stress ( $\tau_0 = 44.5$  MPa), slip arrests while the rupture is still a crack. While the arresting ruptures look very similar, they are classified differently because the arresting pulse meets our criterion for pulse-like rupture described in the main text, while the arresting crack does not.

for multiple values of the diffusion length scale. This produces a diagram that indicates rupture type as a function of the diffusion length scale and the initial stress (Figure 5.9). For each value of the initial stress and each value of the diffusion constant, a corresponding point can be located on the plot. Points corresponding to example plots showing the different rupture types (Figure 5.8) are indicated on the plot as circles. For a specific choice of parameters ( $D$  and  $\tau_0$ ), the region where this point falls determines the type of rupture that our simulation produces.

As expected, the additional weakening and reduced frictional dissipation for the more localized ruptures reduces the minimum shear stress for all types of rupture. The upper curve (orange) in Figure 5.9 is the minimum stress needed to nucleate supershear rupture. An order of magnitude reduction in the diffusion constant reduces the minimum stress needed to nucleate supershear rupture by about 7 MPa. This is a significant fraction of the initial shear stress on the fault, and shows that the reduction in frictional energy dissipation and the increase in dynamic weakening due to localization can significantly alter how slip propagates on the fault.

The lower curves (green, blue, and red) in Figure 5.9 indicate how localization affects rupture propagation at lower initial shear stress. For broad shear bands, slip can only grow in a crack-like manner, but as the diffusion constant is decreased, pulse-like rupture can occur. This is because localization leads to additional dynamic weakening, which was shown to be the crucial frictional characteristic determining when slip propagates as a self-healing pulse by Zheng and Rice [19]. The solid line marks the lowest stress required to propagate slip over the entire fault. This involves crack-like rupture if  $\sqrt{D} > 0.5w$  and pulse-like rupture if  $\sqrt{D} < 0.5w$ . The initial stress needed to fully rupture the fault (solid black) decreases by nearly 10 MPa over the range of diffusion constants that we simulated. This is also a significant fraction of the initial shear stress. As with the supershear rupture transition, the small scale process of localization can alter the manner in which slip propagates at the fault scale.

## 5.6 Discussion

Our simulations with the STZ friction law reveal that the dynamic weakening provided by localization can have a significant impact on fault dynamics. In the STZ model, shear bands spontaneously form and grow in response to dynamic fault slip. This provides a unique description of fault friction. Rather than assuming planar slip with a slip-weakening or Dieterich-Ruina friction law, the dynamic

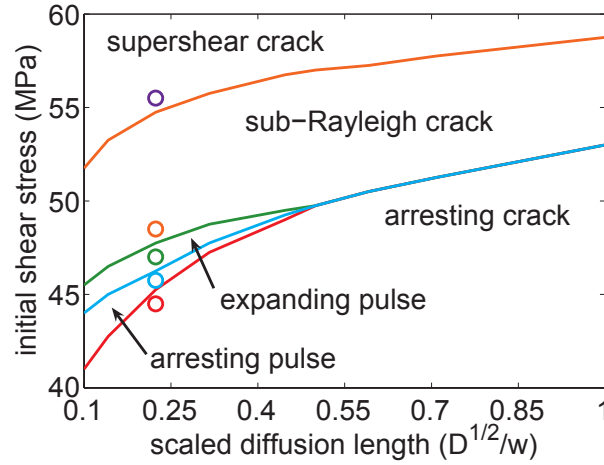


Figure 5.9: Rupture classification diagram as a function of diffusion length scale and initial shear stress for ruptures with STZ Theory. For a given value of the initial shear stress and the diffusion length scale, the region that the point falls into determines the type of rupture that is observed. For larger values of the diffusion length scale (i.e. “broad shear bands”), slip can propagate as a supershear crack, sub-Rayleigh crack, or arresting crack only. For smaller values of the diffusion length scale (i.e. “narrow shear bands”), slip can also propagate as an expanding or arresting pulse. The pulse-like rupture can occur for narrow shear bands because of the dynamic weakening provided by strain localization. The rupture with the narrowest shear band that we simulated reduces the minimum stress required for slip to propagate on the fault (blue line) relative to the broadest shear band by 9 MPa, which is a significant fraction of the initial stress on the fault. The circles on the diagram indicate the specific examples of ruptures that are shown in Figure 5.8.

## CHAPTER 5. STRAIN LOCALIZATION IN DYNAMIC RUPTURE

evolution of the effective temperature determines the strain rate in the fault zone.

Strain localization alters the stress drop and slip rate of dynamic rupture. The stress drop in a simulation that dynamically forms a shear band is larger than if no shear band forms. The peak slip rate is also larger in simulations that form shear bands because the stress weakens over a smaller slip length scale and releases stored elastic energy more rapidly. Ground motion away from the fault tends to be larger if the peak slip rate is increased [119], which suggests that strain localization may impact the ground motion in real earthquakes.

Additionally, we find that localization plays an important role in determining rupture propagation speeds. The stress which marks the transition to supershear changes by a significant amount for the narrowest shear bands. There is evidence of supershear rupture speeds in many earthquakes [107, 108, 127, 128], as well as observations of supershear rupture in laboratory slip experiments [106]. Supershear ruptures radiate seismic waves with a distinct attenuation pattern compared to sub-Rayleigh ruptures [49]. Therefore, understanding the conditions which lead to supershear rupture is important for determining seismic ground motions.

In our simulations, localization provides the dynamic weakening necessary for pulse-like rupture. Our simulations do not produce pulse-like ruptures for homogeneous deformation because there is not enough frictional weakening to allow for pulses in the absence of strain localization. Strain localization reduces the minimum initial stress for the earthquake to rupture the entire fault by about 10 MPa, a significant amount relative to the initial stress on the fault. Seismic observations suggest pulse-like rupture propagation in many earthquakes [53]. Zheng and Rice [19] determined that pulse-like rupture tends to occur for low initial shear stress and with friction laws that exhibit increased velocity weakening in steady state. Our simulations are consistent with their results, as pulses occur at lower initial shear stresses for the narrower shear bands, where there is more dynamic weakening.

In our study, we vary the effective temperature diffusion length scale over an order of magnitude to determine how the amount of dynamic weakening impacts the propagation of ruptures. This parameter is selected because the diffusion length scale is poorly constrained, and because it is difficult to predict precisely what the shear band width will be for a given set of parameters. The final shear band width that the material chooses is dynamically selected by a balance between the nonlinear processes of energy dissipation, effective temperature diffusion, and healing. The width is proportional to the diffusion length scale  $\sqrt{D}$ , but it also depends on the stress, the effective temperature, and the effective temperature specific heat.

We consider a range of effective temperature diffusion length scales because

simulations, experiments, and field observations yield a wide range of shear band thicknesses in amorphous materials. Simulations of glassy materials indicate that shear band thicknesses tend to be approximately 10 particle diameters [24], though for granular materials this could be very different because particles have a greater variety of sizes. Morgan and Boettcher [30] determined that deformation in numerical simulations of fault gouge tends to localize to a narrower shear band when a particle size distribution more heavily weighted towards small particles is used. In each of their simulations, the shear band is only a few particle diameters wide. However, simulations do not include the full range of particle sizes that are found in natural faults [129]. Experimental investigations of shear band thicknesses in granular materials indicate that shear band thickness should scale with the “mean particle diameter,” defined such that 50% of the particles by weight have larger size [130]. Rock mechanics studies on laboratory faults with gouge observe shear band thicknesses that depend on the grain sizes, with the shear band thicknesses ranging from around 100  $\mu\text{m}$  [32] to several millimeters [35]. The thickness of shear bands in natural faults range from hundreds of microns to a few millimeters [36, 37, 38].

The thicknesses of slip zones observed in exhumed faults are even narrower than the shear bands in our simulations [36, 37, 38], indicating that the dynamic weakening from strain localization could be even more dramatic than our results indicate. We did not explore smaller diffusion length scales due to computational limits – the effective temperature grid must be fine enough to resolve the shear band, and the narrower shear bands reduce the slip scale over which the stress weakens. This rapid stress drop requires a smaller grid spacing along strike to produce well resolved simulations.

Laboratory experiments on simulated fault gouge indicate that strain localization, dilation, and frictional rate dependence are interrelated [32, 34]. Fault gouge tends to produce rate strengthening behavior when significant layer dilation occurs for small strains, and rate weakening behavior at larger strains once strain localizes. Effective temperature is a generalization of free volume [29], and so we expect regions of high effective temperature to have a higher free volume and porosity. Because of this, STZ Theory predicts that a homogeneously deforming layer dilates more than a layer with a localized shear band, which is what is observed experimentally. The effective temperature for homogeneous deformation is spatially uniform, while the effective temperature for deformation with a shear band is locally higher in the narrow shear band, and lower everywhere else. The average effective temperature is larger for the spatially uniform effective temperature, and therefore the free volume and porosity are larger, but the average strain rate is the same due to the nonlinear relationship between effective temper-

## CHAPTER 5. STRAIN LOCALIZATION IN DYNAMIC RUPTURE

ature and the plastic strain rate (Equation (2.1)). The experiments also indicate a transition from rate strengthening to rate weakening as localization occurs. In the STZ model as presented in this study, the rate dependence of friction is independent of the degree of localization. However, the transition from rate strengthening for homogeneous deformation to rate weakening for localized deformation can be incorporated by modifying the strain rate dependence of the maximum effective temperature (Equation (2.12)) to the form used in Manning *et al.* [66].

Core samples from the creeping section of the San Andreas Fault Observatory at Depth (SAFOD) indicate that slip occurs throughout the entire gouge width of about 2-3 m (i.e. not localized within the layer) [41]. Laboratory experiments with gouge from the creeping section indicate rate strengthening friction parameters [131]. These results are consistent with STZ Theory, which predicts that rate strengthening materials form shear bands only as transient phenomena [66]. When a rate strengthening material is loaded at a relatively constant rate, STZ Theory predicts that steady sliding is stable and deformation is accommodated over the entire width of the fault gouge, in agreement with the SAFOD experiment.

Slip surfaces are often observed at the boundary between gouge and the host rock in both exhumed faults [37] and laboratory experiments [32]. In STZ Theory, the position where the shear band forms depends on where the initial effective temperature is largest. If there are two or more positions with an equally large initial effective temperature, strain localizes to one. If one of the possible locations is at the boundary, the shear band prefers to form at the boundary rather than in the interior of the gouge layer. Boundary conditions on the effective temperature may also play a role. Our simulations use no conduction boundary conditions, but other boundary conditions, such as fixed effective temperature at the boundary, may yield different results for the preferred shear band location.

STZ Theory provides a microscopic physical basis for plastic deformation in fault gouge. There are also many other processes that are important during seismic slip which are likely to couple to the STZ dynamics, and are not yet incorporated into STZ Theory. Brittle fracture, wear, and comminution create the finely grained gouge in the fault zone [129]. Fracturing rock dissipates energy and creates smaller grains, which might change parameters such as the effective temperature diffusion length scale or the STZ reversal time scale. Thermal heating and weakening, melting, and pressurization of fluids are also believed to be important during fault slip [123, 21, 22, 132, 113]. These processes likely influence the rate at which STZs reverse and how the effective temperature evolves. Determining how these additional processes couple to the STZ friction law may provide further constraints on the physics of the earthquake source.

# Chapter 6

## Localization in Rate Strengthening Materials

In this chapter, we study strain localization in rate strengthening materials, including glasses and fault gouge at high temperatures and pressures. In rate strengthening materials, the shear stress increases as the material is sheared at a faster rate. Because glasses are studied at the laboratory scale, while earthquake rupture occurs at the fault scale, this chapter spans many scales and does not fit easily into the organization of the dissertation by increasing scale. Because this research builds upon both interface scale and fault scale results, we present it here.

The results for glassy materials in this chapter are based upon simulations by Lisa Manning and appear in work published by Manning, Daub, Langer, and Carlson in Physical Review E [66].

### 6.1 Rate Strengthening Friction

Many amorphous materials, such as glasses and fault gouge under high temperature and pressure conditions that occur below the seismogenic zone, do not show rate weakening behavior. Instead, the shear stress increases as the material is sheared at a faster rate.

In the STZ equations, the constitutive parameter that determines the frictional rate dependence is the effective temperature activation barrier,  $\chi_w$ . The value of this parameter relative to unity determines whether the shear stress increases or decreases as the material is sheared at a faster rate. This parameter also plays an important role when analyzing the stability of steady sliding with a spatially

uniform effective temperature. If  $\chi_w < 1$ , steady sliding is linearly unstable – any spatial perturbation to the effective temperature spontaneously grows into a shear band as the material is deformed. If  $\chi_w > 1$ , steady sliding is linearly stable, and the effective temperature remains homogeneous in the material.

However, shear bands are observed to form in rate strengthening materials. Metallic glasses fail along narrow shear bands [31], and localized deformation is observed in rocks below the seismogenic zone [39]. Why does localization happen if steady sliding is linearly stable?

Shear bands form in the STZ model due to a *transient* instability, rather than a linear instability [80, 66]. Shear bands form because the system is driven away from steady-state, and the shear bands persist for large strains. A metallic glass is cooled to form a glassy state before it is sheared and driven away from steady-state, and rapid coseismic slip due to an earthquake nucleating in the seismogenic zone drives the fault at depth away from its slowly creeping steady-state. In this chapter, we investigate the dynamics of localization in these rate strengthening materials to determine the large scale implications.

## 6.2 Deformation of Glassy Materials

Glasses are a class of materials that interest a wide range of scientists, including physicists, materials scientists, and engineers. Like granular fault gouge, a glass does not form a regular crystal structure, and laboratory experiments show that glassy materials form shear bands when they are deformed [31]. Experiments and simulations indicate that glasses exhibit rate strengthening frictional behavior [31, 28], which means that there are some important differences between the deformation of glasses and slip on earthquake faults. In this section, we discuss simulations that examine deformation and failure in an STZ model for glassy materials.

As in our studies of friction in Chapters 2 and 3, we study a material under simple shear (Figure 6.1). The important time scales in the problem are the STZ rearrangement time scale, the stress equilibration time scale, and the inverse plastic strain rate. Because the materials are sheared slowly, the stress equilibration time scale is much faster than the inverse plastic strain rate. Therefore, we assume the stress is constant across the width of the material, and the stress  $\tau$  evolves according to:

$$\frac{d\tau}{dt} = \frac{\mu}{w} \left( V_0 - \int_{-w}^w \dot{\gamma} dy \right). \quad (6.1)$$

The boundaries are driven at a constant rate  $V_0$ , and  $\mu$  is the shear modulus for

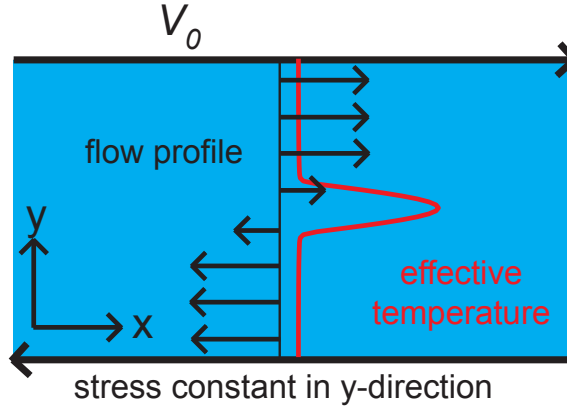


Figure 6.1: Diagram of a glassy material under simple shear. The boundaries are driven at a fixed rate  $V_0$ . We assume that the stress is constant, as its equilibration time scale is much faster than the strain rates we consider in this problem. The effective temperature evolves dynamically to determine the plastic strain rate in the material.

elastic deformations in the material.

The plastic strain in the material is determined by STZ Theory. The strain rate, shear stress, and effective temperature are related via the STZ equation,

$$\dot{\gamma} = f(\tau) \exp(-1/\chi). \quad (6.2)$$

The strain rate in the material is dictated by the evolution of the effective temperature in the material,

$$\frac{\partial \chi}{\partial t} = \frac{\dot{\gamma} \tau}{c_0 \tau_y} \left( 1 - \frac{\chi}{\hat{\chi}(\dot{\gamma})} \right) + \frac{\partial}{\partial y} \left( \dot{\gamma} D \frac{\partial \chi}{\partial y} \right). \quad (6.3)$$

Equations (6.1) and (6.3) are integrated with zero effective temperature flux boundary conditions at  $y = \pm w$ .

For glassy materials, we utilize simulation data to constrain the stress dependence  $f(\tau)$  and the maximum effective temperature  $\hat{\chi}(\dot{\gamma})$  [28]. The rate switching function  $R(\tau)$  that we use in this study is a combination of an exponential stress dependence at low stress, and a square root power law stress dependence at large stresses. The simulations tend to be in the large stress limit, so the stress dependence in the STZ equation is approximately

$$f(\tau) \approx \frac{2\epsilon}{t_0} \left( \frac{\tau}{\tau_1} \right)^{1/2} \left( 1 - \frac{\tau_y}{\tau} \right). \quad (6.4)$$

CHAPTER 6. LOCALIZATION IN RATE STRENGTHENING MATERIALS

The parameter  $\tau_1$  sets the stress scale for STZ reversals.

The effective temperature depends on the strain rate in the material. A plot of the negative logarithm of the strain rate versus the inverse steady-state effective temperature is shown in Figure 6.2 [61]. The curve shows a linear regime at high strain rates, which we use for earthquake rupture because earthquake slip generally occurs at high strain rates. We are interested in the deformation of glassy materials at low and high strain rates, so we include the portion of the curve where the effective temperature is independent of the strain rate. Our equation for the maximum effective temperature  $\hat{\chi}$  is [61]

$$\log\left(\frac{q_0}{t_0\dot{\gamma}}\right) = \frac{\chi_w}{\hat{\chi}} + \left(\frac{\chi_1}{\hat{\chi} - \chi_0}\right) \exp\left(-b\frac{\hat{\chi} - \chi_0}{\chi_A - \chi_0}\right). \quad (6.5)$$

The first term on the right hand side accounts for the linear dependence at high strain rates, and the second term produces a constant effective temperature  $\chi_0$  at low strain rates.

We start from zero shear stress and a constant effective temperature with a perturbation of the form  $\delta\chi \operatorname{sech}(z/\delta z)$  added at the center of the material. We then shear the material at a constant driving rate. We vary two parameters: the initial effective temperature, and the driving rate. We vary the constant starting effective temperature to simulate variability in the cooling of the glassy material before it is sheared. We also vary the driving rate to determine how the material deforms over a range of strain rates.

Deformation in the STZ model occurs in four different ways: homogeneous deformation, “disorder limited” shear bands, “diffusion limited” shear bands, and material failure. Each of these types of deformation occur for different sets of the initial effective temperature and the plastic strain rate.

Homogeneous deformation occurs for all strain rates for large values of the initial effective temperature. Homogeneous deformation occurs because the material is too close to steady-state for the transient instability to occur. An example of the plastic strain rate as a function of position for several different values of the shear strain is shown in Figure 6.3. For the smallest values of the strain, the plastic strain rate is zero throughout the material. This is because plastic deformation occurs only after the shear stress builds up elastically from zero to the yield stress. Once the material yields, the strain rate is roughly constant throughout the material. The strain rate is slightly elevated in the center due to the perturbation to the initial effective temperature, but this is a small difference.

For lower values of the initial effective temperature, strain localizes into a shear band. The material is farther from steady-state if the effective temperature is lower, and leads to a transient instability. One example of localized strain is a

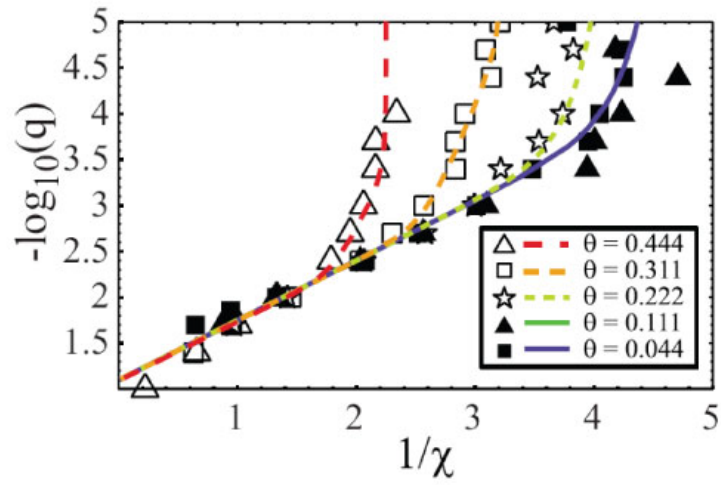


Figure 6.2: Plot of the negative logarithm of the non-dimensional strain rate  $q = t_0 \dot{\gamma}$  versus the inverse effective temperature. The different colored curves correspond to varying thermal temperature in the simulation data. There are two important regimes: the linear rate-dependent portion of the curve, which occurs at high strain rates, and the glassy portion of the curve, where the effective temperature is independent of the strain rate. Deformation of glassy materials occurs at both low and high strain rates, and so the maximum effective temperature  $\hat{\chi}(\dot{\gamma})$  must account for both regimes for this study. Figure taken from Langer and Manning [61].

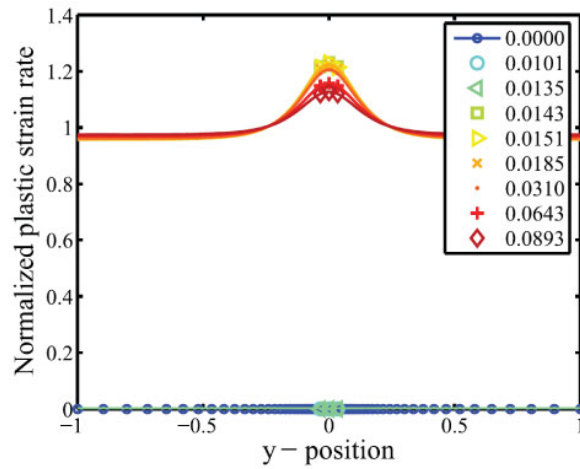


Figure 6.3: Snapshots of plastic strain rate as a function of  $y$ -position in the material for varying shear strains for an example of homogeneous deformation. The strain rate is zero for small strains until the stress reaches the yield stress, and then the strain rate is roughly constant throughout the material. Homogeneous deformation occurs if the initial effective temperature is larger, as the transient instability relies on the material being driven away from steady-state.

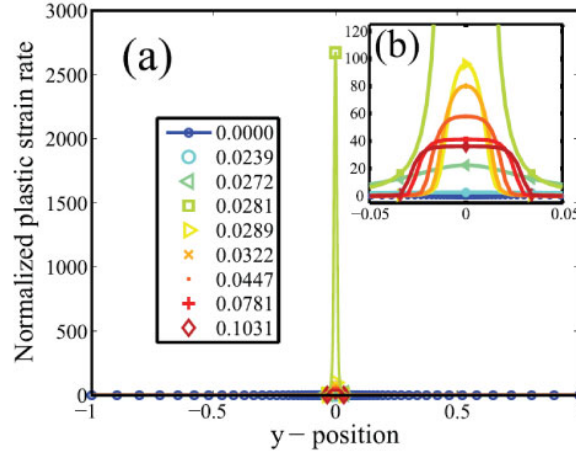


Figure 6.4: Plastic strain rate as a function of position for a “diffusion limited” shear band. The various curves show the strain rate at several values of the strain. (a) Deformation is localized to a sharply peaked shear band, the thickness of which is set by the diffusion length scale. (b) As the material deforms further, the strain rate decreases and the shear band thickness increases, but deformation remains highly localized.

“diffusion limited” shear band. Figure 6.4 plots the plastic strain rate as a function of position for a “diffusion limited” shear band. In this type of deformation, a very narrow shear band forms that accommodates all of the deformation in the material. Diffusion and energy dissipation are balanced in the effective temperature evolution equation, and the diffusion length scale determines the shear band thickness.

Another variety of localized deformation that occurs is “disorder limited” shear bands, shown in Figure 6.5. The plots show snapshots of the plastic strain rate as a function of position at various strains. In this case, the plastic strain rate is much larger in the center of the material. This shear band is called a “disorder limited” shear band because the shear band thickness is much larger than the length scale in the diffusion term. The effective temperature in the shear band grows more quickly than in the rest of the material until it is equal to the maximum effective temperature. The effective temperature cannot become any larger in the center, but the strain rate in the material does not match the imposed strain at the boundaries. In order to accommodate additional deformation, the shear band instead spreads out until the strain rate matches the applied rate at the boundaries.

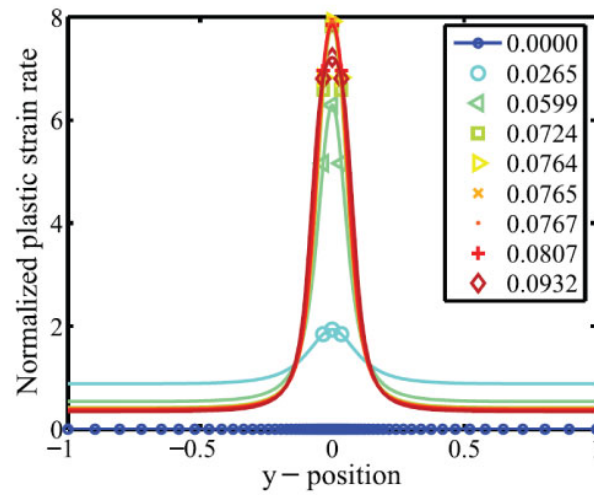


Figure 6.5: Plots of plastic strain rate as a function of  $y$ -position in the material for several values of the shear strain for a “disorder limited” shear band. The strain rate is much larger in the center of the material, indicating that the deformation occurs in a localized shear band. The thickness of the shear band is much larger than the diffusion length scale, which distinguishes this from the “diffusion limited” shear band shown in Figure 6.4.

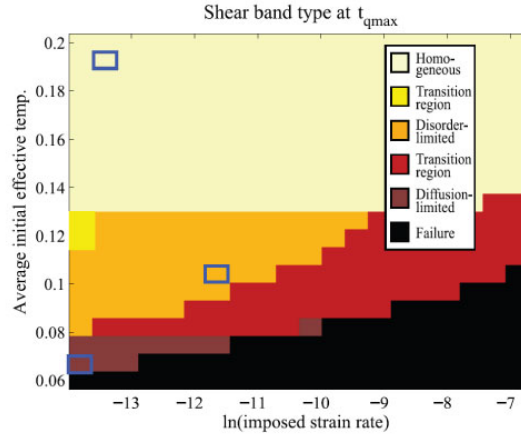


Figure 6.6: Deformation map for glassy materials as a function of the initial effective temperature and the applied strain rate. The different colors show when homogeneous deformation, “disorder limited” shear bands, “diffusion limited” shear bands, and material failure occur. The map also shows where transition regions lie between the different types of deformation.

The final type of localized deformation that occurs is material failure. In this case, the strain rate is so highly localized that the strain rate exceeds the strain rate where STZ Theory breaks down ( $q_0/t_0$ ). At strain rates this large, deformation no longer occurs as isolated STZs, and the constitutive equations are not valid. This type of deformation occurs at the lowest initial effective temperature. At very low initial effective temperature, there are very few STZs and therefore to drive the material at a high plastic strain rate, the stress must be very large. The effective temperature grows more quickly than the stress relaxes, and the strain rate becomes so large that the effective temperature diverges. When STZ Theory breaks down, the material behaves more like a fluid, and a constitutive relation for amorphous flow is required to describe subsequent deformation of the material.

We can construct a deformation map for glassy materials as a function of the applied strain rate and the initial effective temperature to determine when homogeneous deformation, “diffusion limited” shear bands, “disorder limited” shear bands, and material failure occur. Figure 6.6 shows this deformation map. The boundaries between the different types of deformation are not sharp, and a shear band that is initially “diffusion limited” can become a “disorder limited” shear band at large strains. Therefore, there are transition regions on the deformation map between the various regimes.

Our numerical studies illustrate that rate strengthening materials can deform

in many different ways than rate weakening materials – rate weakening materials either form “diffusion limited” shear bands or fail. Rocks can also exhibit rate strengthening friction parameters, and we discuss the deformation of these materials in the following section.

### 6.3 Localization in Coseismic Slip Below the Seismogenic Zone

When under the high temperature and pressure conditions deep in the earth’s crust, rocks deform in a ductile manner [15, 16, 17], and the frictional behavior is rate strengthening. This is observed in the field in rocks known as S-C mylonites [39]. These rocks are sheared in a ductile manner due to the slow creep of interseismic loading. The deformation occurs broadly throughout the rocks. This deformation is illustrated in Figure 6.7. On the left, in Figure 6.7(a), the broad ductile deformation is the roughly diagonal lines running from the lower left to the upper right. On the right, in Figure 6.7(b), the blue lines indicate the shear fabric that is observed in the rocks in the field.

This broad deformation is superimposed with narrow localized deformation that is distinct from the ductile deformation. The localized deformation occurs when an earthquake propagates down into the ductily deforming layer, shearing the material much faster than the slow creep of interseismic loading. The localized deformation is illustrated by horizontal lines in Figure 6.7(a), and the red lines in Figure 6.7(b).

The deformation observed in these rocks is consistent with the predictions of STZ Theory. During the interseismic period, because the parameters are rate strengthening, the equations reach their stable steady-state solution. Deformation occurs broadly over the entire fault zone, and produces the ductile strain observed in the field. Localized coseismic slip occurs because the material is driven away from steady state. The transient instability occurs because of the huge change in driving rate – the long-term creeping rate of faults is of the order centimeters/year, while coseismic slip rates are of order meters/second. This is a change of about  $10^9$  in the slip rate, and a change this large drives the gouge away from steady-state.

To explore the fault scale consequences of strain localization below the seismogenic zone, we study a dynamic rupture model with the fault zone governed by STZ Theory. Figure 6.8 illustrates the fault in our model. This dynamic rupture model is very similar to the model discussed in Chapter 5, so we only briefly discuss the differences. In this dynamic rupture model, the first important difference is that the STZ friction parameters vary with depth, while the STZ parameters

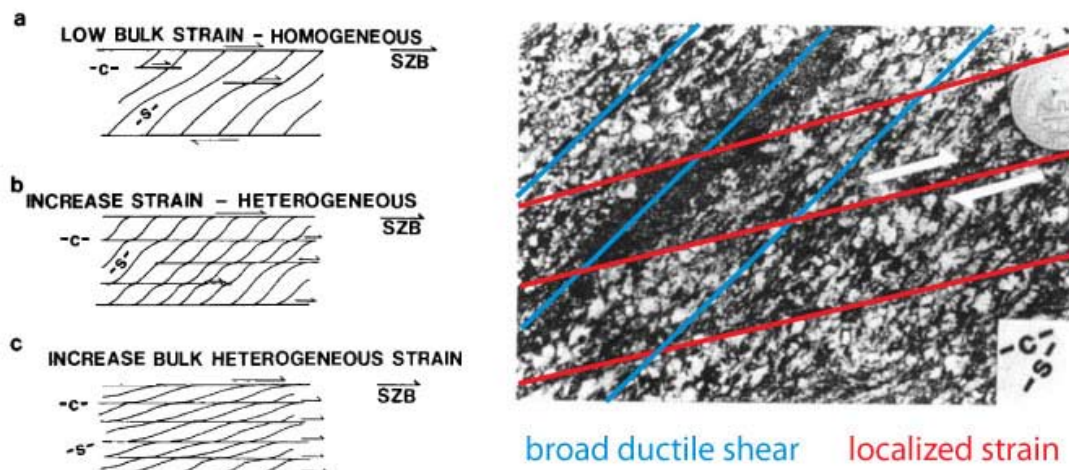


Figure 6.7: Rocks deformed below the seismogenic zone, known as S-C mylonites. At the large temperatures and pressures deep in the earth, the rock deforms in a ductile manner. (a) The fabric in the rocks is due to a combination of broad, ductile shear, and localized strain from earthquakes that originate in the seismogenic zone and propagate to depth. The broad shear is indicated by the diagonal lines, and the localized coseismic slip produces the horizontal lines. (b) Field observations of this deformation. The blue lines indicate the ductile shear, and the red lines show the location of localized shear. Figure adapted from Simpson [39].

## CHAPTER 6. LOCALIZATION IN RATE STRENGTHENING MATERIALS

in Chapter 5 did not vary spatially. The other important difference is that we assume that the slip is only in the  $x$ -direction, and that the fault is translationally invariant in the  $x$ -direction. This simplifies the dynamic rupture equations to 2D anti-plane rupture propagation. Chapter 5 assumed 2D in-plane rupture propagation. This model allows us to investigate if localized slip at depth alters fault scale rupture propagation. The elastodynamics of the fault are modeled using the boundary integral method discussed in Chapter 4.

In the dynamic rupture model, frictional quantities vary with depth. In particular, we vary the normal stress and the frictional rate dependence with depth, consistent with the varying frictional parameters in the earth. The normal stress increases linearly with depth, and the yield stress is always proportional to the normal stress. The shear stress increases with depth. The normal stress and initial shear stress are shown as a function of depth in Figure 6.9(a). The initial shear stress is perturbed over a small region at 11 km depth to initiate rupture. The rate dependence of friction is based on laboratory studies of rock friction at high temperatures and pressures [17]. We adopt a depth-dependent profile for the STZ activation stress  $\sigma_d$  and the frictional rate dependence  $\chi_w$  based on these experiments. The dependence of the activation stress  $\sigma_d$  on depth is plotted in Figure 6.9(b), and the rate dependence of friction is shown in Figure 6.9(c). The rate dependence plot shows that friction is rate strengthening at shallow depths, rate weakening in the seismogenic zone, and rate strengthening below 14.5 km depth. The initial effective temperature varies with depth, as Figure 6.9(d) illustrates. The initial effective temperature is small in the seismogenic zone, as that region has few STZs and behaves more like a solid. Deeper in the crust, the initial effective temperature increases, as there is plastic deformation occurring at depth due to ductile creep.

Our goal is to test if strain localization below the seismogenic zone alters rupture propagation relative to homogeneous shear at depth. If strain localization is important, then two ruptures with identical slip in the seismogenic zone should propagate differently upon encountering the rate strengthening region. In the seismogenic zone, it is most important that the rupture in the localized and homogeneous models are identical and propagate all the way to depth. Because of this, we use a homogeneous rupture in the seismogenic zone for simplicity. Although we showed in Chapter 5 that localization in earthquake ruptures results in dynamic weakening and large peak slip rates, the model requires a fine grid spacing along the spatial extent of the fault to resolve these features. We are more interested in resolving what occurs below the seismogenic zone in this study, which requires a that the fault have a large spatial extent.

We consider two different models with these depth dependent friction param-

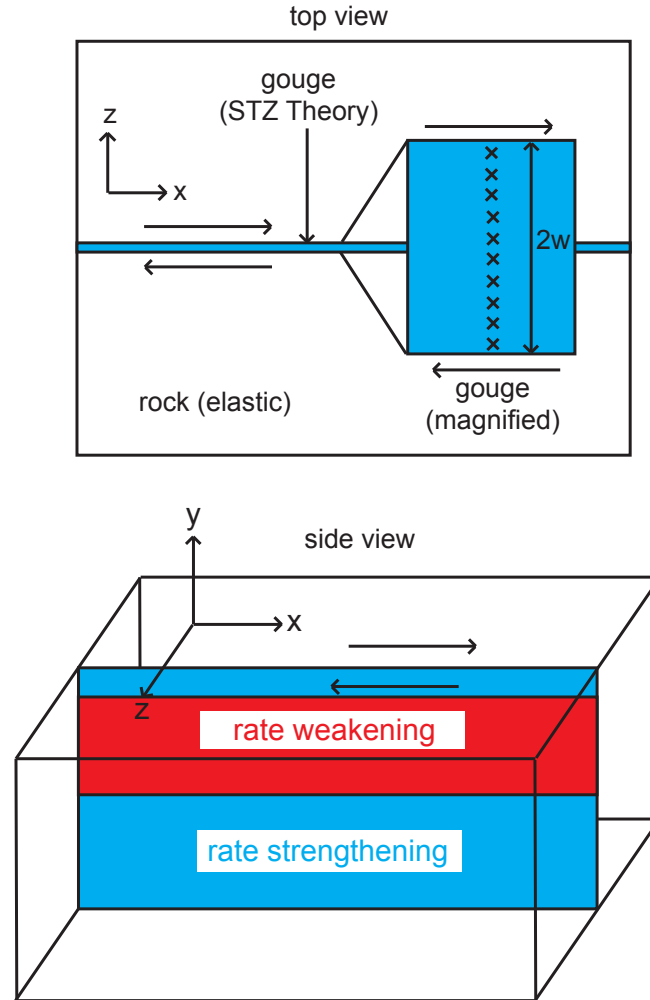


Figure 6.8: Schematic of the fault for modeling rupture propagation below seismogenic depth. A layer of fault gouge governed by STZ Theory is sheared between elastic rocks. Within the gouge, we resolve the dynamic evolution of the effective temperature, which dictates how strain localizes during dynamic fault slip. Slip is assumed to be purely in the  $x$ -direction, and the system is symmetric in the  $x$ -direction. Fault parameters vary with depth (see Figure 6.9). In particular, the fault has rate strengthening properties at shallow depths, rate weakening properties in the seismogenic zone, and rate strengthening parameters below 14.3 km depth. This captures the dynamic propagation of slip from the seismogenic zone to the creeping zone below.

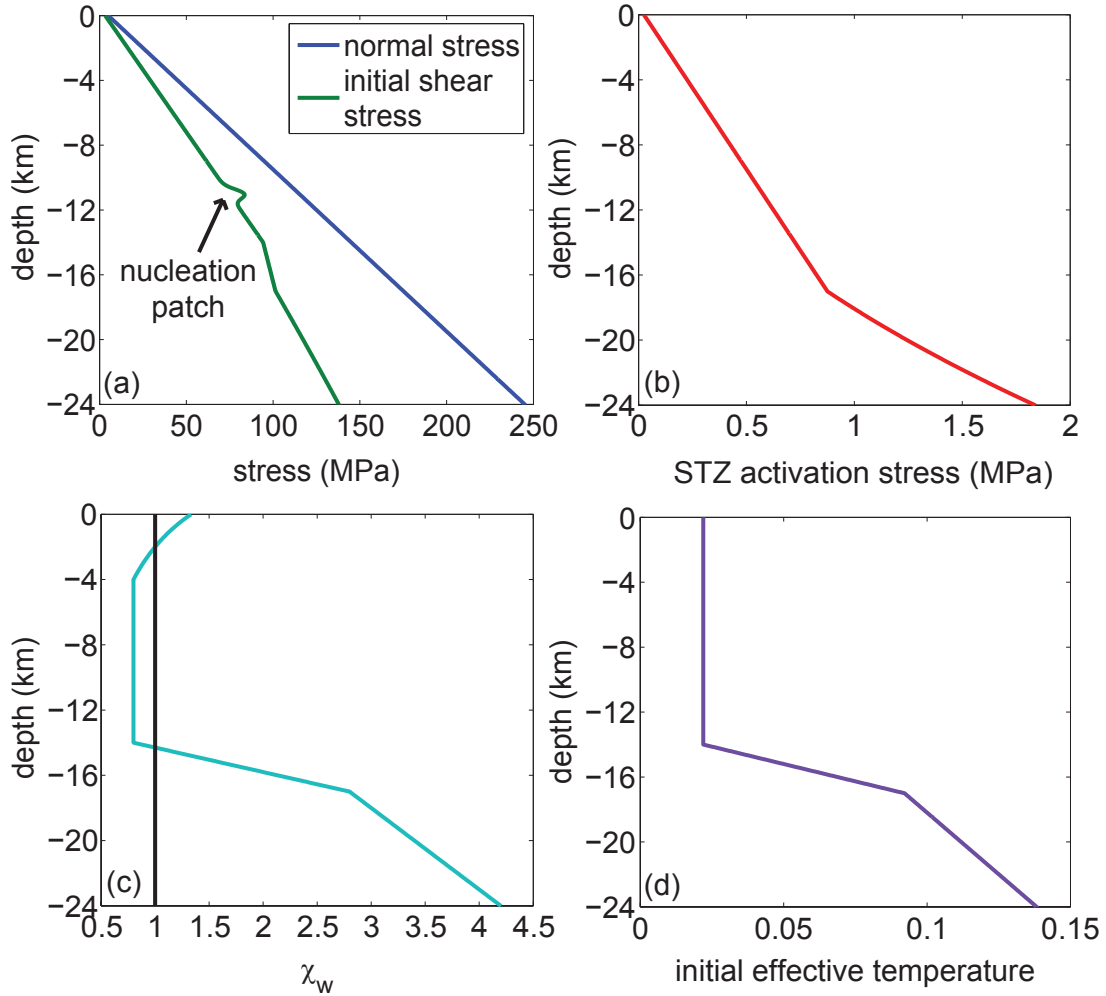


Figure 6.9: Depth-dependent frictional parameters in dynamic rupture simulations. (a) Normal stress and shear stress increase with depth. The shear stress is increased over a small region at 11 km depth to nucleate rupture. (b) STZ activation stress as a function of depth. Up to 17 km depth, the STZ activation stress is proportional to the normal stress, and is a larger fraction of the normal stress at greater depth, consistent with rock friction experiments at high temperature and pressure. (c) The rate dependence of friction varies with depth, consistent with laboratory experiments. Friction transitions from rate strengthening ( $\chi_w > 1$ ) to rate weakening ( $\chi_w < 1$ ) at 2 km depth, and from rate weakening to rate strengthening at 14.3 km depth. (d) Depth dependence of the initial effective temperature. Below the seismogenic zone, the material is ductile and undergoes more plastic deformation, and thus has a larger effective temperature and more STZs.

eters. In the first model, which we refer to as Model H, the effective temperature is spatially uniform everywhere. Because homogeneous strain produces fault behavior that is very similar to Dieterich-Ruina friction, a model where slip does not localize indicates what a laboratory based friction law would predict for rupture propagation. In the second model, which we refer to as Model L, a small perturbation of the form  $\delta\chi/\cosh(z/\delta z)$  is added to the effective temperature in the rate strengthening region below 14.5 km depth. In Model H, due to symmetry, the plastic strain rate is always uniform across the fault zone. However, the effective temperature varies with depth, and is time dependent. In Model L, strain spontaneously localizes at depth as the fault slips due to the transient instability in the STZ equations. The effective temperature also varies with depth and with time in Model L.

First, we examine the dynamics of strain localization in Model L. Figure 6.10 shows the shear stress as a function of slip at a depth of 15.75 km, which is over a kilometer below the transition to rate strengthening. The shear stress increases before slip initiates, and then gradually decreases before reaching a steady shear stress. Note that the final sliding shear stress is greater than the initial stress. This occurs for two reasons. First, the stress increases because the slip rate increases, as the friction parameters are rate strengthening. Because the fault is rate strengthening at depth, there is also greater slip in the seismogenic zone than at depth. Due to the elasticity of the rock, this slip deficit increases the shear stress at depth. These two factors combine to produce a negative stress drop below the seismogenic zone.

Figure 6.11 illustrates the plastic strain rate profile for several representative points shown on the stress versus slip plot (Figure 6.10). For small slips, the effective temperature is approximately spatially uniform across the fault zone. This is because the perturbation to the effective temperature is still growing, and the shear band has not formed. Once the stress weakens, the plastic strain rate forms a sharp and narrow peak. This peak decreases in size as the fault slips further, but the deformation remains localized for the duration of coseismic slip. This shows that nearly all of the coseismic slip at depth in a dynamic rupture is accommodated in a narrow shear band.

At the fault scale, we compare the slip propagation below the seismogenic zone to assess the impact of localization on rupture dynamics. Figure 6.12 shows three snapshots of the slip rate as a function of depth. The left plot Figure 6.12 demonstrates that rupture propagates unstably through the seismogenic zone, and that the rupture is identical for both models as desired. The slip rate is larger in the down dip direction because the increasing normal stress also increases the stress drop. The plot in the center shows the slip rate shortly after the

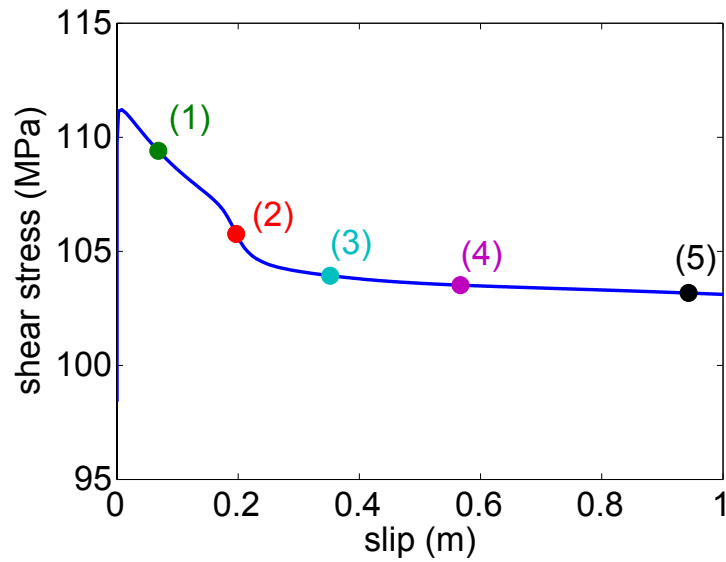


Figure 6.10: Shear stress as a function of slip for a point below the seismogenic zone (15.75 km depth) for Model L. Stress increases to a peak value as slip initiates, and then drops as the fault slips. The stress drops off more quickly once the shear band forms, and reaches a steady sliding stress above the initial value due to the rate strengthening nature of the material. The colored points indicate times when the plastic strain rate is plotted as a function of position in the fault zone (Figure 6.11).

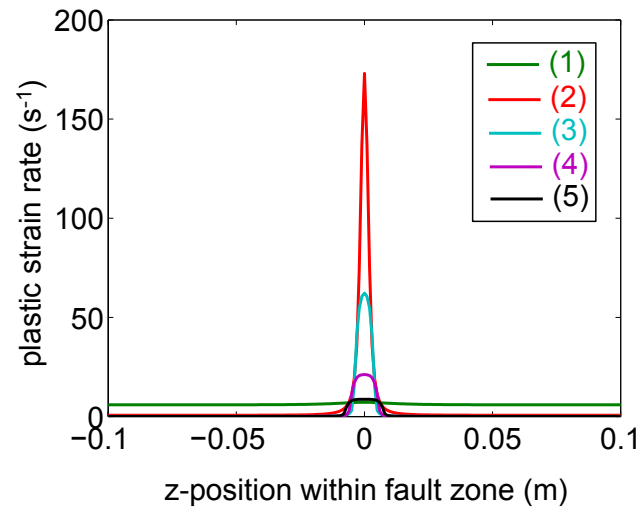


Figure 6.11: Snapshots of the plastic strain rate as a function of position in the fault zone for various times shown in Figure 6.10. The curves are for Model L, and are at a depth of 15.75 km, which is below the seismogenic zone in the rate strengthening region. For small values of the slip, the strain rate is uniform throughout the fault zone. When the shear stress begins to drop more rapidly, the strain rate becomes very large and sharply peaked. The peak strain rate drops as the fault continues to slip, and strain remains localized for the duration of seismic slip.

ruptures encounter the rate strengthening region. The slip rate at the rupture front decreases dramatically for slip below the seismogenic zone. The inset shows that there is a small difference in the slip rate in the rate strengthening region. Due to localization, the slip rate is larger, though this is a small effect – both Model H and Model L are arresting in the rate strengthening region. The rightmost plot shows that rupture arrests after reaching about 17 km depth. The slip rate also decreases when it reaches the rate strengthening region at the surface, but the rupture is able to slip all the way to zero depth.

There is only a small difference between the two models because regions with rate strengthening parameters have negative stress drops, and therefore are energy sinks. Shear stress must drop to release stored elastic strain energy from the bulk. If the stress increases, slip stores additional strain energy in the elastic bulk, and ruptures that encounter rate strengthening regions quickly arrest. Therefore, by examining how the shear stress evolves with slip for Model H and Model L, we can determine how localization changes the energy balance of slip at depth.

Localization changes two aspects of the shear stress during slip: the final shear stress, and the rate at which stress drops from its peak value to reach the final shear stress. For rate weakening parameters, both of these changes encourage rupture propagation. The final sliding stress is lower, because the elevated strain rate in the shear band leads to dynamic weakening, and the increase in the rate at which stress drops reduces frictional dissipation.

For rate strengthening friction, however, these two effects are competing. The shear stress as a function of slip is shown for Model H and Model L at 15.75 km depth in Figure 6.13. The shear stress drops more quickly in Model L, which reduces energy dissipation on the fault. This makes the rate strengthening region less of an energy sink, and because of this the slip rate in the strengthening region in Figure 6.12 (center) is slightly larger. However, the final sliding stress is higher for Model L when compared to Model H. This is because for rate strengthening parameters, an elevated strain rate inside the shear band increases the final sliding friction. Therefore, the increase in the shear stress competes with the reduction in frictional dissipation, and the end result is a rupture that arrests quickly for both Model H and Model L.

An important question that arises from this is how much seismic radiation comes from slip at depth, and if this radiation could be detected by seismometers at the surface. Because Models H and L produce nearly identical slip at depth, seismograms almost certainly cannot distinguish between them at the surface. Additionally, because the slip rate at depth is less than the slip rate in the seismogenic zone, less radiation occurs from the deep slip. However, more quantitative investigation of the effect of this slip on ground motion is needed.

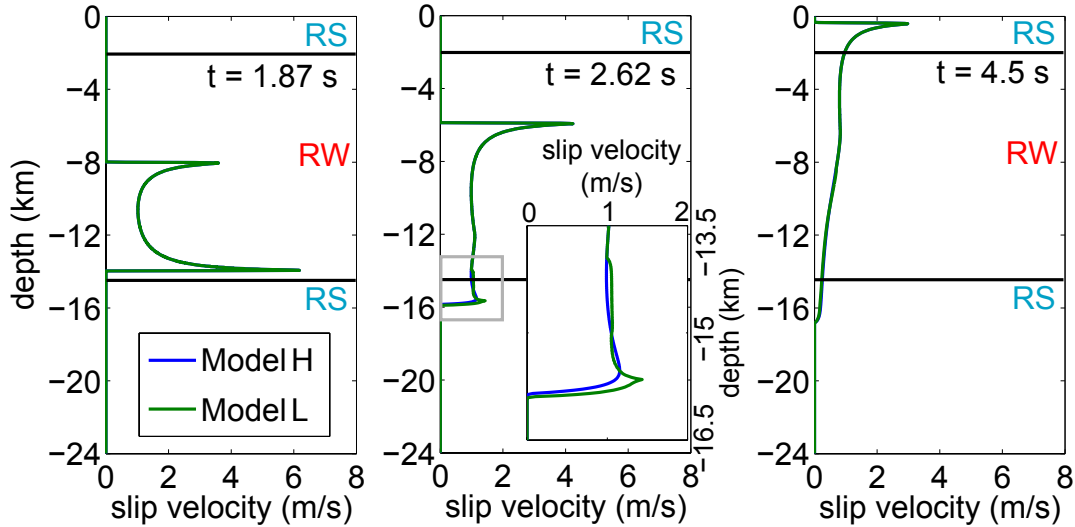


Figure 6.12: Slip rate as a function of depth at three different times during dynamic rupture for Model H and Model L. “RS” and “RW” designate the depths that have rate strengthening and rate weakening parameters, respectively. (left) Rupture propagates unstably through the seismogenic zone due to its rate weakening parameters. The slip rate is larger in the downdip direction because the increasing normal stress leads to a larger stress drop. The slip rate is identical for both models, as we do not model localization in the seismogenic zone. (center) Upon encountering the rate strengthening region, the slip rate decreases. The inset shows that localization slightly alters the slip rate in the strengthening region. The slip rate is slightly larger in the rate strengthening region in Model L. (right) The rupture arrests at the base of the seismogenic zone after propagating to about 17 km depth. Rupture reaches the surface, though the rate strengthening region decreases the slip rate. The slip rate is nearly identical for Model H and Model L.

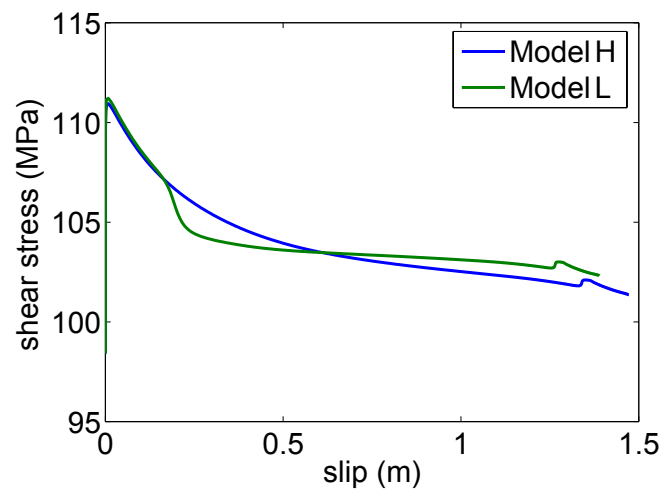


Figure 6.13: Shear stress as a function of slip for a point below the seismogenic zone (15.75 km depth) for Models H and L. The curves show the two competing effects due to localization – Model L drops off more quickly with slip once the shear band forms, but Model H reaches a lower shear stress. Model L remains at a larger shear stress because the strain rate is elevated in the shear band and the friction parameters are rate strengthening at this depth. The effects roughly cancel each other, and rupture propagation is nearly identical between the models.

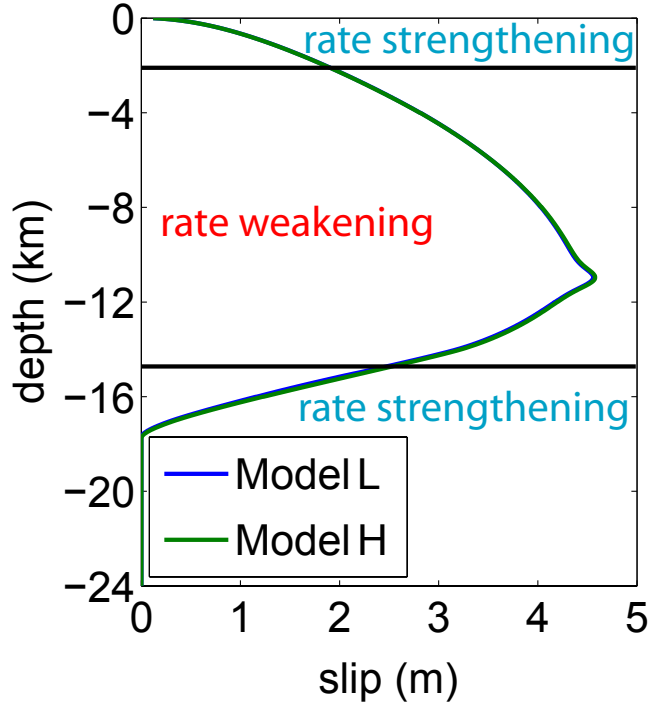


Figure 6.14: Final slip as a function of depth for Model H and Model L. In both models, 5% of the seismic moment occurs below the transition to rate strengthening. The slip propagates to 17 km depth in both models.

The final slip as a function of depth is also nearly identical between Model H and Model L, as Figure 6.14 illustrates. In both models, about 5% of the seismic moment occurs below the seismogenic zone, and there is no slip below 17.5 km. Because this model is fairly simple and does not include along strike variations in rupture propagation, it is unclear how the percentage of slip at depth might vary with the size of the earthquake. This question arises in earthquake scaling relations, which we now discuss.

Seismologists are interested in determining the depth of rupture propagation on faults for several reasons. When performing seismic inversions, modelers often arbitrarily cut slip off at 15 km depth [134]. However, if slip routinely occurs at larger depths in earthquakes, then it is important to allow for slip at those depths when inverting for source parameters.

Additionally, earthquake scaling relations suggest a constant stress drop and that seismic moment should scale with the length of the rupture squared [135, 136].

However, if slip cannot occur below seismogenic depths, then this scaling breaks down for large earthquakes that propagate for distances longer than  $\sim 15$  km. If slip does not occur below 15 km depth, then the stress drop must scale with the seismic moment, and the scaling with the length of the rupture squared no longer holds. The scaling of seismic moment with rupture length is observed even for large events, which indicates that slip can propagate deeper than 15 km. King and Wesnousky [137] measured slip in crustal earthquakes that broke the surface, and found that the scaling relations from their data suggest that larger earthquakes propagate below the seismogenic zone.

Hillers and Wesnousky [138] and Shaw and Wesnousky [139] investigated these scaling relations through numerical models of many earthquake sequences. Their results show that slip can propagate further below the seismogenic zone, though the results depend on the parameters chosen. Hillers and Wesnousky found that if the transition from rate strengthening to rate weakening was more gradual than the transition predicted by rock mechanics experiments, then their calculations produced scaling relations consistent with observations. Shaw and Wesnousky determined that a rate strengthening region with parameters that do not vary with depth allowed for deeper penetration of coseismic slip.

Fully dynamic rupture simulations with similar depth dependent properties found that dynamic rupture propagates to a depth similar to the lowest depth of slip in our model with STZ Theory [100]. However, our model captures the localization of strain at depth, and better matches field observations of rock deformation. It is still unclear as to what the correct depth dependent frictional parameters are to capture the correct physics at the base of the seismogenic zone. The rock friction experiments that our depth dependent friction parameters are based on use thin layers of fault gouge in the experiments, but S-C mylonites show that the deformation over fault zones that are many orders of magnitude thicker (on the order of a kilometer) Therefore, it is possible that the friction experiments do not capture the correct frictional behavior of much thicker fault zones, and the thicker fault zones exhibit frictional properties similar to the Hillers and Wesnousky or Shaw and Wesnousky. More research is needed to understand the role of frictional parameters, strain localization, and elastodynamics to determine the depths to which coseismic slip occurs.

## 6.4 Discussion

Our results for rate strengthening materials show that strain localization is an important physical process in their deformation. We find that glassy materials

## CHAPTER 6. LOCALIZATION IN RATE STRENGTHENING MATERIALS

show rate strengthening behavior, and glasses can deform in several different ways. This includes homogeneous deformation, broad “disorder limited” shear bands, narrow “diffusion limited” shear bands, and material failure. This contrasts with the results for rate weakening materials, which only form “diffusion-limited” shear bands or fail in the same manner as rate strengthening materials. The formation of “disorder limited” shear bands requires rate strengthening parameters, and are interesting because the shear band width is a length scale other than the diffusion length scale. The shear bands in rate strengthening materials persist for large strains – steady sliding is linear stable, but long-lived transients can prevent materials from ever reaching steady state.

In our models, shear bands occur due to a transient instability in the effective temperature dynamics. However, it is also possible for shear bands to form due to stress effects. In the simple shear geometry that we study, the static solution to the stress equations is a spatially homogeneous stress, which indicates that stress effects are not particularly important. Instead, the structure of the material, which is captured by the effective temperature, is what drives strain localization. Stress effects may be important for localization in earthquake slip below the seismogenic zone, as the localization of slip in the seismogenic zone produces stress effects that lead to localized slip at depth. However, because field observations indicate a single slip surface at seismogenic depths [37], stress effects cannot explain the multiple shear bands in Figure 6.7. Further research is needed to assess the relative contributions of stress and effective temperature in localized slip below the seismogenic zone.

For earthquake ruptures, strain localization in rate strengthening materials is important for slip below the seismogenic zone. Broad and localized deformation is observed in rocks that were below the seismogenic zone. The STZ model predicts that slow creep produces broad ductile strain, while coseismic slip generates localized slip. We examine the fault scale consequences of localization below the seismogenic zone, and find that the effects of localization compete – the shear stress drops more quickly, reducing dissipation, but the sliding stress increases, roughly canceling any benefits of reduced dissipation. Therefore, the fault scale rupture propagation is nearly identical with and without localization.

# Chapter 7

## Conclusions

### 7.1 Synopsis

The earthquake problem is challenging due to its multi-scale nature, with large uncertainties at every scale. Our approach captures basic observations of grain scale material deformation through the STZ constitutive law, and studies its implications at larger scales in the dynamics of friction and earthquake rupture. We find that the small scale physics has large scale implications for frictional instabilities and dynamic rupture propagation.

The STZ model captures features of simulations of a wide range of amorphous materials, including glasses, granular materials, thin film lubricants, and earthquake faults. Plastic deformation occurs in localized regions, and the total number of STZs is governed by an effective disorder temperature. The effective temperature quantifies the disorder in the packing of the material, and serves as a macroscopic quantity that determines the internal state of the material. The STZ model resolves the dynamic evolution of the strain rate in the material, which is a unique feature of the STZ model compared to other constitutive descriptions. Strain localization leads to dynamic weakening for rate weakening frictional parameters – the strain rate is elevated in the shear band, which reduces the sliding friction.

Our study of stick-slip instabilities shows that laboratory scale friction dynamics are affected by strain localization. We find that localization increases the critical spring stiffness where steady sliding becomes unstable, and our linear stability analysis is in agreement with numerical integration. Our simulations also produce irregular stick-slip dynamics due to the small scale physics of localization.

At the fault scale, STZ Theory impacts earthquake rupture propagation. Our results show that the differences between the FV law to the Dieterich-Ruina and

## CHAPTER 7. CONCLUSIONS

Slip Weakening laws have fault scale implications. We find that for equal energy dissipation on the fault, the FV law exhibits lower peak slip rates, smaller nucleation lengths, and larger amounts of slip for friction to weaken to its minimum value. The difference in the nucleation lengths alters the shear stress at which rupture transitions to supershear for the laws. The rapid weakening versions of the friction laws show that rupture can propagate at low initial shear stress as a self-healing slip pulse, and the due to differences in small scale physics, the FV and DR laws with rapid weakening transition to pulse-like rupture at a different value of the shear stress.

We also compare ruptures that dynamically form a shear band to ruptures where strain remains homogeneous at the fault scale. The dynamic weakening of localization increases both the stress drop and the peak slip rate, and a homogeneous rupture of a narrower width cannot capture all features of rupture propagation with localization. We also vary the diffusion length scale to assess the role of this length scale in dynamic rupture. The diffusion length scale controls the shear band width, and our simulations show that as the diffusion length scale decreases, fault slip dissipates less energy and the fault slides at a lower shear stress. Localization plays an important role in how slip propagates in space and time at the fault scale, including lowering the shear stress at which supershear rupture nucleates and allowing for pulse-like rupture propagation at low shear stress. The results indicate that the dynamic weakening of localization can have a significant impact on rupture propagation at the fault scale.

Strain localization is also important for rate strengthening materials, which form shear bands due to a transient instability. We investigate this phenomenon in glassy materials, and find that several types of deformation occur, including homogeneous strain, localized strain in a “disorder limited” shear band, localized strain in a “diffusion limited” shear band, and material failure. We investigate when these types of deformation occur as a function of the initial effective temperature and the average strain rate to create a deformation map for glassy materials.

Rate strengthening friction also occurs in the earth’s crust at depths below the seismogenic zone. These rocks deform in a ductile manner during the interseismic period, but form shear bands when coseismic slip propagating down dip from the seismogenic zone deforms the rock. We find that strain spontaneously localizes at creeping depths due to coseismic slip in a dynamic rupture model, and nearly all the coseismic slip is accommodated through a narrow shear band. This shows that the transient instability in STZ Theory can produce localized slip at depth consistent with field observations.

In this work, we find that STZ Theory can be used to model deformation and localization in a wide range of amorphous materials. Because the model is

a continuum approximation, it is tractable for use in fault scale rupture models. This approach captures the physics at each scale, and improves the predictions of multi-scale models of deformation in a wide range of systems.

## 7.2 Future Directions

STZ Theory provides a microscopic physical basis for deformation in amorphous materials, and because it is a continuum approach it remains tractable for modeling dynamics at the fault scale. This “vertical” approach to the multi-scale earthquake problem reveals the fault scale consequences of grain scale strain localization. However, the STZ model neglects many physical processes that seismologists believe are important at each different scale. Future work with STZ Theory to develop efficient ways to incorporate these additional processes into rupture models can determine the fault scale implications.

Many of the important physical processes that are neglected in the STZ model occur at the grain scale. These processes contribute to the dynamics of friction, and therefore could have fault scale consequences. For example, the finely granulated nature of fault gouge indicates that brittle fracture and grain comminution are important processes during earthquake slip [129]. A version of STZ theory could be developed that include the effects of grain wear and fracture, which might alter the STZ equations and change the energy budget. Another important factor at the grain scale is heating and weakening due to seismic slip [21, 22, 132]. Pore fluid pressurization at high slip rates and weakening of contacts could change the rate at which STZs rearrange, and dramatically change the shear stress during seismic slip.

Laboratory observations indicate that the rate dependence of rock friction is logarithmic for small slip rates up to 0.1-1 m/s, after which thermal weakening mechanisms become important [21]. This crossover behavior can be naturally incorporated into STZ Theory through the parameter  $q_0$ , which determines the strain rate at which STZ Theory breaks down. While our simulations here assume that  $q_0$  is large enough that STZ Theory is valid even at seismic slip rates, it is possible that at large slip rates when contacts between grains are heated, deformation is no longer accommodated by local STZs. A new constitutive model that describes the deformation at these large strain rates could account for the physics that operates at large strain rates. Current models for thermal weakening are often phenomenological, so incorporating the ideas into STZ Theory puts these physical mechanisms onto a stronger theoretical footing.

Many of the additional mechanisms that can be incorporated into STZ The-

## CHAPTER 7. CONCLUSIONS

ory are important because they alter the energy balance of faulting. Even in the absence of these mechanisms, STZ Theory can be used to investigate energy dissipation during seismic slip. Because STZ Theory provides a microscopic physical basis for deformation in amorphous materials, we can quantitatively determine the energy balance of slip in the STZ model. In particular, energy dissipation in the STZ model increases the configurational entropy of the gouge packing, which is energy that is not dissipated as thermal heat. The traditional picture of energy dissipation during faulting divides energy between fracture energy, which is energy that goes into breaking rock and creating new surfaces, and energy that is dissipated as thermal heat [117]. STZ Theory improves upon this description by providing microscopic physical basis for energy dissipation.

In all of our models, we assume that the time scale for stress equilibration is much faster than the inverse plastic strain rate. This assumption simplifies the dynamic equations for the stress in the fault gouge (Equation (3.1)). Also, it highlights that in our model, the disorder in the material is responsible for shear bands and not variations in the stress. However, these stress effects could be important for localization in some cases. Stress effects are necessary to form a shear band that extends in space (such as the fracture surface in Figure 1.8) from a random initial effective temperature. Earthquakes that deform the fault gouge in the seismogenic zone in a localized manner may produce localized deformation below the seismogenic zone through this mechanism. Research that adds in stress effects is needed to better understand the effects of shear bands in situations where spatial variations in the shear stress are important.

All of these exciting avenues for future work show that we are just scratching the surface of incorporating small scale physics into fault scale dynamic earthquake models. By combining exciting recent developments in theory, laboratory experiments, numerical simulations, field observations, and earthquake modeling, seismologists can improve constraints on the complex dynamics occurring in the earth at each scale and improve estimates of seismic hazard.

# Bibliography

- [1] Ida, Y. (1972), Cohesive force across the tip of a longitudinal-shear crack and Griffith's specific surface energy, *J. Geophys. Res.*, *77*(20), 3796-3805.
- [2] Andrews, D. J. (1976a), Rupture propagation with finite stress in antiplane strain, *J. Geophys. Res.*, *81*, 3575-3582.
- [3] Andrews, D. J. (1976b), Rupture velocity of plane strain shear cracks, *J. Geophys. Res.*, *81*, 5679-5687.
- [4] Day, S. M. (1982), Three-dimensional simulation of spontaneous rupture: the effect of non-uniform prestress, *Bull. Seismol. Soc. Am.*, *72*, 1881-1902.
- [5] Harris, R. A., and S. M. Day (1993), Dynamics of fault interaction: parallel strike-slip faults, *J. Geophys. Res.*, *98*, 4461-4472.
- [6] Madariaga, R., K. B. Olsen, and R. J. Archuleta (1998), Modeling dynamic rupture in a 3D earthquake fault model, *Bull. Seismol. Soc. Am.*, *88*, 1182-1197.
- [7] Ohnaka, M. (2003), A constitutive scaling law and a unified comprehension for frictional slip failure, shear fracture of intact rock, and earthquake rupture, *J. Geophys. Res.*, *108*(B2), 2080, doi:10.1029/2000JB000123.
- [8] Palmer, A. C., and J. R. Rice (1973), The growth of slip surfaces in the progressive failure of overconsolidated clay, *Proc. R. Soc. London, Ser. A*, *332*, 527-548.
- [9] Blau, P. J. (1989), in *Friction and Wear Transitions of Materials: Break-in, Run-in, Wear-in*, Noyes, Park Ridge, NJ, 312-317.
- [10] Dieterich, J. H. (1979), Modeling of rock friction 1. Experimental results and constitutive equations, *J. Geophys. Res.*, *84*(NB5), 2161-2168.

## BIBLIOGRAPHY

- [11] Ruina, A. L. (1980), Friction laws and instabilities: A quasistatic analysis of some dry frictional behavior, Ph.D. Thesis, Brown University, Providence, R.I.
- [12] Ruina, A. L. (1983), Slip instability and state variable friction laws, *J. Geophys. Res.*, *88*, 10359-10370.
- [13] Dieterich, J. H., and B. D. Kilgore (1994), Direct observation of frictional contacts – new insights for state dependent properties, *Pure Appl. Geophys.*, *143*(1-3), 283-302.
- [14] Kato, N., and T. E. Tullis (2001), A composite rate- and state-dependent law for rock friction, *Geophys. Res. Lett.*, *28*(6), 1103-1106.
- [15] Stesky, R. M., W. F. Brace, D. K. Riley, and P.-Y. F. Robin (1974), Friction in faulted rock at high temperature and pressure, *Tectonophysics*, *23*(1-2), 177-203.
- [16] Blanpied, M. L., D. A. Lockner, and J. D. Byerlee (1991), Fault stability inferred from granite sliding experiments at hydrothermal conditions, *Geophys. Res. Lett.*, *18*(4), 609-612.
- [17] Blanpied, M. L., D. A. Lockner, and J. D. Byerlee (1995), Frictional slip of granite at hydrothermal conditions, *J. Geophys. Res.*, *100*(B7), 13,045-13,064.
- [18] Scholz, C. H. (1998), Earthquakes and friction laws, *Nature*, *391*, 37-42.
- [19] Zheng, G., and J. R. Rice (1998), Conditions under which velocity-weakening friction allows a self-healing versus a crack-like mode of rupture, *Bull. Seismol. Soc. Am.*, *88*, 1466-1483.
- [20] Rice, J. R., N. Lapusta, and K. Ranjith (2001), Rate and state dependent friction and the stability of sliding between elastically deformable solids, *J. Mech. Phys. Solids*, *49*, 1865-1898.
- [21] Tullis, T. E., and D. L. Goldsby (2003), Flash melting of crustal rocks at almost seismic slip rates, *Eos Trans. AGU*, *84*(46), Fall Meet. Suppl., Abstract S51B-05.
- [22] Di Toro, G., D. L. Goldsby, and T. E. Tullis (2004), Friction falls towards zero in quartz rock as slip velocity approaches seismic rates, *Nature*, *427*, 436-439.
- [23] Lapusta, N., and J. R. Rice (2003b), Low-heat and low-stress operation in earthquake models of statically strong but dynamically weak faults, *Eos Trans. AGU*, *84*(46), Fall Meet. Suppl., Abstract S51B-02.

## BIBLIOGRAPHY

- [24] Falk, M. L., and J. S. Langer (1998), Dynamics of viscoplastic deformation in amorphous solids, *Phys. Rev. E*, *57*(6), 7192-7205.
- [25] Falk, M. L., and J. S. Langer (2000), From simulation to theory in the physics of deformation and fracture, *MRS Bull.*, *25*(5), 40-45.
- [26] Falk, M. L., and Y. Shi (2002), Strain localization in a molecular-dynamics model of a metallic glass, in *Supercooled Liquids, Glass Transition, and Bulk Metallic Glasses*, *Mat. Res. Soc. Symp. Proc.*, *754*, vol. 754, edited by T. Egami et al., p. 257, Warrendale, Pa.
- [27] Lois, G., A. Lemaitre, and J. M. Carlson (2005), Numerical tests of constitutive laws for dense granular flows, *Phys. Rev. E*, *72*, 051303.
- [28] Haxton, T. K., and A. J. Liu (2007), Activated dynamics and effective temperature in a steady state sheared glass, *Phys. Rev. Lett.*, *99*, 195701.
- [29] Langer, J. S. (2008), Shear-transformation-zone theory of plastic deformation near the glass transition, *Phys. Rev. E*, *77*, 021502.
- [30] Morgan, J. K., and M. S. Boettcher (1999), Numerical simulations of granular shear zones using the distinct element method - 1. Shear zone kinematics and the micromechanics of localization, *J. Geophys. Res.*, *104*(B2), 2703-2720, doi:10.1029/1998JB900056.
- [31] Lu, J., G. Ravichandran, and W. L. Johnson (2003), Deformation behavior of the  $Zr_{41.2}Ti_{13.8}Cu_{12.5}Ni_{10}Be_{22.5}$  bulk metallic glass over a wide range of strain-rates and temperatures, *Acta Mater.*, *51*(12), 3429-3443, doi:10.1016/S1359-6454(03)00164-2.
- [32] Beeler, N. M., T. E. Tullis, M. L. Blanpied, and J. D. Weeks (1996), Frictional behavior of large displacement faults, *J. Geophys. Res.*, *101*(B4), 8697-8715.
- [33] Marone, C. (1998), Laboratory-derived friction laws and their application to seismic faulting, *Ann. Rev. Earth Planet. Sci.*, *26*, 643-696.
- [34] Mair, K., and C. Marone (1999), Friction of simulated fault gouge for a wide range of velocities and normal stresses, *J. Geophys. Res.*, *104*(B12), 28899-28914 doi:10.1029/1999JB900279.
- [35] Chambon, G., J. Schmittbuhl, and A. Corfdir (2006), Frictional response of a thick gouge sample: 1. Mechanical measurements and microstructures, *J. Geophys. Res.*, *111*, B09308, doi:10.1029/2003JB002731.

## BIBLIOGRAPHY

- [36] Chester, F. M., J. P. Evans, and R. L. Biegel (1993), Internal structure and weakening mechanisms of the San Andreas Fault, *J. Geophys. Res.*, *98*(B1), 771-786.
- [37] Chester, F. M., and J. S. Chester (1998), Ultracataclasite structure and friction processes of the Punchbowl fault, San Andreas system, California, *Tectonophysics*, *295*, 199-221.
- [38] Wibberley, C. A. J., and T. Shimamoto (2003), Internal structure and permeability of major strike-slip fault zones: The Median Tectonic Line in Mie Prefecture, southwest Japan, *J. Struct. Geol.*, *25*(1), 59-78, doi:10.1016/S0191-8141(02)00014-7.
- [39] Simpson, C. (1984), Borrego Springs-Santa Rosa mylonite zone: A late Cretaceous west-directed thrust in southern California, *Geology*, *12*(1), 8-11.
- [40] Zoback, M. D. (2006), SAFOD penetrates the San Andreas Fault, *Scientific Drilling*, *2*(2006), 32-33.
- [41] Hickman, S. H., M. D. Zoback, W. L. Ellsworth, D. Kirschner, and J. Solum (2007), Structure and composition of the San Andreas Fault at seismogenic depths: recent results from the SAFOD experiment, *Eos Trans. AGU*, *88*(52), Fall Meet. Suppl., Abstract T44B-01.
- [42] Page, M. T., E. M. Dunham, and J. M. Carlson (2005), Distinguishing barriers and asperities in near-source ground motion, *J. Geophys. Res.*, *110*, B11302, doi:10.1029/2005JB003736.
- [43] Beroza, G., and T. Mikumo (1996), Short slip duration in dynamic rupture in the presence of heterogeneous fault properties, *J. Geophys. Res.*, *101*, 22449-22460.
- [44] Harris, R. A. (2004), Numerical simulations of large earthquakes: Dynamic rupture propagation on heterogeneous faults, *Pure Appl. Geophys.*, *161*, 11-12, 2171-2181.
- [45] Olsen, K. B., R. Madariaga, and K. B. Olsen (1997), Three dimensional dynamic simulation of the 1992 Landers earthquake, *Science*, *278*, 834-838.
- [46] Dunham, E. M. (2007), Conditions governing the occurrence of supershear ruptures under slip-weakening friction, *J. Geophys. Res.*, *112*, B07302, doi:10.1029/2006JB004717.

## BIBLIOGRAPHY

- [47] Das, S., and B. V. Kostrov (1983), Breaking of a single asperity: Rupture process and seismic radiation, *J. Geophys. Res.*, *88*, 4277-4288.
- [48] Schmedes, J., R. J. Archuleta, and D. Lavallée, Correlation of earthquake source parameters inferred from dynamic rupture simulations, submitted to *J. Geophys. Res.*
- [49] Dunham, E. M., and R. J. Archuleta (2005), Near-source ground motion from steady state dynamic rupture pulses, *Geophys. Res. Lett.*, *32*(3), L03302, doi:10.1029/2004GL021793.
- [50] Dunham, E. M., P. Favreau, and J. M. Carlson (2003), A supershear transition mechanism for cracks, *Science*, *299*, 1557.
- [51] Schmedes, J., R. J. Archuleta, and D. Lavallée (2009), Dependency of supershear transition in dynamic rupture simulations on the autocorrelation of initial stress, *Seismol. Res. Lett.* *80*(2), 301.
- [52] Kosrov, B. (1964), Self-similar problems of propagation of shear cracks, *J. Appl. Math. Mech.*, *28*, 1077-1087.
- [53] Heaton, T. H. (1990), Evidence for and implications of self-healing pulses of slip in earthquake rupture, *Phys. Earth Planet. Int.*, *64*(1), 1-20.
- [54] Day, S. M. (1982), Three-dimensional finite difference simulation of fault dynamics: rectangular faults with fixed rupture velocity, *Bull Seismol. Soc. Am.*, *72*, 705-727.
- [55] Ide, S., and M. Takeo (1997), Determination of constitutive relations of fault slip based on seismic wave analysis, *J. Geophys. Res.*, *102*(B12), 27379-27391, doi:10.1029/97JB02675.
- [56] Daub, E. G., and J. M. Carlson (2008), A constitutive model for fault gouge deformation in dynamic rupture simulations, *J. Geophys. Res.*, *113*, B12309, doi:10.1029/2007JB005377.
- [57] Daub, E. G., M. L. Manning, J. M. Carlson (2008), Shear strain localization in elastodynamic rupture simulations, *Geophys. Res. Lett.*, *35*, L12310, doi:10.1029/2008GL033835.
- [58] Lemaitre, A., and J. M. Carlson (2004), Boundary lubrication with a glassy interface, *Phys. Rev. E*, *69*(6), 061611.

## BIBLIOGRAPHY

- [59] Lemaitre, A. (2002), Rearrangements and dilatancy for sheared dense materials, *Phys. Rev. Lett.*, *89*(19), 195503.
- [60] Eyring, H. J. (1936), Viscosity, plasticity, and diffusion as examples of absolute reaction rates, *J. Chem. Phys.*, *4*, 283.
- [61] Langer, J. S., and M. L. Manning (2008), Steady-state, effective-temperature dynamics in a glassy material, *Phys. Rev. E*, *76*, 056107.
- [62] Shi, Y., M. B. Katz, H. Li, and M. L. Falk (2007), Evaluation of the disorder temperature and free-volume formalisms via simulations of shear banding in amorphous solids, *Phys. Rev. Lett.*, *98*, 185505.
- [63] Dieterich, J. H. (1972), Time dependent friction in rocks, *J. Geophys. Res.*, *77*(20), 3690.
- [64] Scott, G. D., and D. M. Kilgour (1969), The density of random close packing of spheres, *J. Phys. D: Appl. Phys.*, *2*, 863-866, doi:10.1088/0022-3727/2/6/311.
- [65] Segall, P., and J. R. Rice (1995), Dilatancy, compaction, and slip instability of a fluid-infiltrated fault, *J. Geophys. Res.*, *100*(B11), 22155-22171, doi:10.1029/95JB02403.
- [66] Manning, M. L., E. G. Daub, J. S. Langer, and J. M. Carlson (2009), Rate-dependent shear bands in a shear-transformation-zone model of amorphous solids, *Phys. Rev. E*, *79*, 016110.
- [67] Daniels, K. E., and N. W. Hayman (2008), Force chains in seismogenic faults visualized with photoelastic granular shear experiments, *J. Geophys. Res.*, *113*, B11411, doi:10.1029/2008JB005781.
- [68] Brace, W. F., and J. D. Byerlee (1966), Stick slip as a mechanism for earthquakes, *Science* *153*, 990-992.
- [69] Brace, W. F. (1972), Laboratory studies of stick-slip and their application to earthquakes, *Tectonophys.*, *14*, 189-200.
- [70] Anthony, J. L., and C. J. Marone (2005), Influence of particle characteristics on granular friction, *J. Geophys. Res.*, *100*, B08409, doi:10.1029/2004JB003399.
- [71] Yoshizawa, H., and J. N. Israelachvili (1993), Fundamental mechanisms of interfacial friction. 2. Stick-slip friction of spherical and chain molecules, *J. Phys. Chem.*, *97*(43), 11300-11313.

## BIBLIOGRAPHY

- [72] Drummond, C., and J. Israelachvili (2001), Dynamic phase transitions in confined lubricant fluids under shear, *Phys. Rev. E*, *63*(4), 041506.
- [73] Gourdon, D., and J. N. Israelachvili (2003), Transitions between smooth and complex stick-slip sliding of surfaces, *Phys. Rev. E*, *68*(2), 021602.
- [74] Zeng, H., M. Tirrell, and J. Israelachvili (2006), Limit cycles in dynamic adhesion and friction processes: A discussion, *J. Adhesion*, *82*, 933-943, doi:10.1080/00218460600875979.
- [75] Rice, J. R., and A. L. Ruina (1983), Stability of steady frictional slipping, *J. Appl. Mech.*, *50*, 343-349.
- [76] Gu., J. C., J. R. Rice, A. L. Ruina, and S. T. Tse (1984), Slip motion and stability of a single degree of freedom elastic system with rate and state dependent friction, *J. Mech. Phys. Sol.*, *32*, 167-196.
- [77] Batista, A. A., and J. M. Carlson (1998), Bifurcations from steady sliding to stick slip in boundary lubrication, *Phys. Rev. E*, *57* 4986-4996.
- [78] Thompson, P. A., and M. O. Robbins (1990), Origin of stick-slip motion in boundary lubrication, *Science*, *250*, 792-794.
- [79] Luan, B., and M. O. Robbins (2004), Effect of inertia and elasticity on stick-slip motion, *Phys. Rev. Lett.*, *93*(3), 036105.
- [80] Manning, M. L., J. S. Langer, and J. M. Carlson (2007), Strain localization in a shear transformation zone model for amorphous solids, *Phys. Rev. E*, *76*(5), 056106.
- [81] Tsai, J.-C., and J. P. Gollub (2005), Granular packings sheared in an annular channel: Flow localization and grain size dependence, *Phys. Rev. E*, *72*, 051304.
- [82] Lauridsen, J., M. Twardos and M. Dennin (2002), Shear-Induced Stress Relaxation in a Two-Dimensional Wet Foam, *Phys. Rev. Lett.*, *89*, 098303.
- [83] Carlson, J. M., and A. A. Batista (1996), Constitutive relation for the friction between lubricated surfaces, *Phys. Rev. E*, *53*, 4153-4165.
- [84] Baumberger, T., F. Heslot, and B. Perrin (1994), Crossover from creep to inertial motion in friction dynamics, *Nature*, *367*, 544-546.

## BIBLIOGRAPHY

- [85] Drummond, C., and J. Israelachvili (2000), Dynamic behavior of confined branched hydrocarbon lubricant fluids under shear, *Macromolecules*, *33*, 4910-4920.
- [86] Majumdar, T. S., and R. P. Behringer (2005), Contact force measurements and stress-induced anisotropy in granular materials, *Nature*, *435*, 1079-1082.
- [87] Erickson, B., B. Birnir, and D. Lavallee (2008), A model for aperiodicity in earthquakes, *Nonlin. Proc. Geophys.*, *15*(1), 1-12.
- [88] Perrin, G., J. R. Rice, and G. Zheng (1995), Self-healing slip pulse on a frictional surface, *J. Mech. Phys. Solids*, *43*, 1461-1495.
- [89] Nielsen, S. B., J. M. Carlson, and K. B. Olsen (2000), Influence of friction and fault geometry on earthquake rupture, *J. Geophys. Res.*, *105*(B3), 6069-6088, doi:10.1029/1999JB900350.
- [90] Nielsen, S. B., and J. M. Carlson (2000), Rupture pulse characterization: Self-healing, self-similar, expanding solutions in a continuum model of fault dynamics, *Bull. Seismol. Soc. Am.*, *90*, 1480-1497, doi:10.1785/0120000021.
- [91] Bizzarri, A., and M. Cocco (2005), 3D dynamic simulations of spontaneous rupture propagation governed by different constitutive laws with rake rotation allowed, *Annals of Geophys.*, *48*(2), 279-299.
- [92] Carlson, J. M., and J. S. Langer (1989), Mechanical model of an earthquake fault, *Phys. Rev. A*, *40*, 6470.
- [93] Cochard, A., and R. Madariaga (1996), Complexity of seismicity due to highly rate-dependent friction, *J. Geophys. Res.*, *101*, 25321-25336, doi:10.1029/96JB02095.
- [94] Shaw, B. E., and J. R. Rice (2000), Existence of continuum complexity in the elastodynamics of repeated fault ruptures, *J. Geophys. Res.*, *105*(B10), 23791-23810, doi:10.1029/2000JB900203.
- [95] Rice, J. R. (1983), Constitutive relations for fault slip and earthquake instabilities, *Pure Appl. Geophys.*, *121*, 443-475.
- [96] Marone, C., and B. Kilgore (1993), Scaling of the critical slip distance for seismic faulting with shear strain in fault zones, *Nature*, *362*(6421), 618-621.

## BIBLIOGRAPHY

- [97] Bizzarri, A., M. Cocco, D. J. Andrews, and E. Boschi (2001), Solving the dynamic rupture problem with different numerical approaches and constitutive laws, *Geophys. J. Int.*, *143*(3), 656-678, doi:10.1046/j.1365-246x.2001.01363.x.
- [98] Cochard, A., and R. Madariaga (1994), Dynamic faulting under rate-dependent friction, *Pure Appl. Geophys.*, *142*(3-4), 419-445.
- [99] Geubelle, P. H., and J. R. Rice (1995), A spectral method for 3-dimensional elastodynamic fracture problems, *J. Mech. Phys. Solids*, *43*(11), 1791-1824.
- [100] Lapusta, N., J. R. Rice, Y. Ben-Zion, and G. Zheng (2000), Elastodynamic analysis for slow tectonic loading with spontaneous rupture episodes on faults with rate- and state-dependent friction, *J. Geophys. Res.*, *105*(B10), 23765-23789, doi:10.1029/2000JB900250.
- [101] Okubo, P. (1989), Dynamic rupture modeling with laboratory-derived constitutive relations, *J. Geophys. Res.*, *94*(B9), 12321-12335.
- [102] Bizzarri, A., and M. Cocco (2003), Slip-weakening behavior during the propagation of dynamic ruptures obeying rate- and state-dependent friction laws, *J. Geophys. Res.*, *108*(B8), 2373, doi:10.1029/2002JB002198.
- [103] Cocco, M., and A. Bizzarri (2002), On the slip-weakening behavior of rate-and-state dependent constitutive laws, *Geophys. Res. Lett.*, *29*(11), 1516, doi:10.1029/2001GL013999.
- [104] Lapusta, N., and J. R. Rice (2003), Nucleation and early seismic propagation of small and large events in a crustal earthquake model, *J. Geophys. Res.*, *108*(B4), 2205, doi:10.1029/2001JB000793.
- [105] Guatteri, M., and P. Spudich (2000), What can strong-motion data tell us about slip-weakening fault-friction laws?, *Bull. Seism. Soc. Am.*, *90*, 98-116, doi:10.1785/0119990053.
- [106] Rosakis, A. J., O. Samudrala, and D. Coker (1999), Cracks faster than the shear wave speed, *Science*, *284*, 1337-1340.
- [107] Archuleta, R. J. (1984), A faulting model for the 1979 Imperial Valley earthquake, *J. Geophys. Res.*, *89*, 4559-4585.
- [108] Bouchon, M., M. P. Bouin, H. Karabulut, M. N. Toksöz, M. Dietrich, and A. Rosakis (2001), How fast is rupture during an earthquake? New insights

## BIBLIOGRAPHY

- from the 1999 Turkey earthquakes, *Geophys. Res. Lett.*, *28*(14), 2723-2726, doi:10.1029/2001GL013112.
- [109] Dunham, E. M., and R. J. Archuleta (2004), Evidence for a supershear transient during the 2002 Denali fault earthquake, *Bull. Seismol. Soc. Am.*, *94*(6), 256-268, doi:10.1785/0120040616.
- [110] Tsutsumi, A., and T. Shimamoto (1997), High-velocity frictional properties of gabbro, *Geophys. Res. Lett.*, *24*(6), 699-702, doi:10.1029/97GL00503.
- [111] Hirose, T., and T. Shimamoto (2005), Growth of molten zone as a mechanism of slip weakening of simulated faults in gabbro during frictional melting, *J. Geophys. Res.*, *110*(B5), B05202, doi:10.1029/2004JB003207.
- [112] O'Hara, K., K. Mizoguchi, T. Shimamoto, and J. C. Hower (2006), Experimental frictional heating of coal gouge at seismic slip rates: Evidence for devolatilization and thermal pressurization of gouge fluids, *Tectonophysics*, *424*, 109-118.
- [113] Rice, J. R. (2006), Heating and weakening of faults during earthquake slip, *J. Geophys. Res.*, *111*, B05311, doi:10.1029/2005JB004006.
- [114] Hickman, S. H. (1991), Stress in the lithosphere and the strength of active faults, *Rev. Geophys.*, *29*, 759-775.
- [115] Sibson, R. H. (1994), An assessment of field evidence for "Byerlee" friction, in *Faulting, Friction and Earthquake Mechanics*, Part 1, pp. 645-662, Birkhaeuser Verlag, Basel, Switzerland.
- [116] Abercrombie, R. E., and J. R. Rice (2005), Can observations of earthquake scaling constrain slip weakening?, *Geophys. J. Int.*, *162*, 406-424, doi:10.1111/j.1365-246X.2005.02579.x.
- [117] Kanamori, H., and T. H. Heaton (2000), Microscopic and macroscopic physics of earthquakes, in *Geocomplexity and the Physics of Earthquakes*, American Geophysical Union Geophysical Monograph 120, pp. 147-163, AGU, Washington, DC.
- [118] Guatteri, M., P. Spudich, and G. C. Beroza (2001), Inferring rate and state friction parameters from rupture models of the 1995 Hyogoken Nambu (Kobe) earthquake, *J. Geophys. Res.*, *106*(B11), 26511-26521, doi:10.1029/2001JB000294.

## BIBLIOGRAPHY

- [119] Aagaard, B. T., J. F. Hall, and T. H. Heaton (2001), Characterization of near-source ground motions with earthquake simulations, *Earthquake Spectra*, *17*, 177-207.
- [120] Blanpied, M. L., T. E. Tullis, and J. D. Weeks (1998), Effects of slip, slip rate, and shear heating on the friction of granite, *J. Geophys. Res.*, *103*(B1), 489-512, doi:10.1029/97JB02480.
- [121] Sleep, N. H. (1995), Ductile creep, compaction, and rate and state dependent friction within major fault zones, *J. Geophys. Res.*, *100*(B7), 13065-13080, doi:10.1029/94JB03340.
- [122] Frye, K. M., and C. Marone (2002), The effect of humidity on granular friction at room temperature, *J. Geophys. Res.*, *107*(11), 2309, doi:10.1029/2001JB000654.
- [123] Lachenbruch, A. H., (1980), Frictional heating, fluid pressure, and the resistance to fault motion, *J. Geophys. Res.*, *85*(NB11), 6097-6112.
- [124] Marone, C., J. E. Vidale, and W. Ellsworth (1995), Fault healing inferred from time dependent variations in source properties of repeating earthquakes, *Geophys. Res. Lett.*, *22*(22), 3095-3098, doi:10.1029/95GL03076.
- [125] Li, Y.-G., J. E. Vidale, S. M. Day, D. D. Oglesby, and E. Cochran (2003), Postseismic fault healing on the rupture zone of the 1999 *M* 7.1 Hector Mine, California, earthquake, *Bull. Seismol. Soc. Am.*, *93*, 854-869, doi:10.1785/0120020131.
- [126] Noda, H, E. M. Dunham, and J. R. Rice, Earthquake ruptures with thermal weakening and the operation of major faults at low overall stress levels, *J. Geophys. Res.*, doi:10.1029/2008JB006143, in press.
- [127] Bouchon, M., and M. Vallée, (2003), Observation of long supershear rupture during the magnitude 8.1 Kunlunshan Earthquake, *Science*, *301*, 824-826, doi:10.1126/science.1086832.
- [128] Ellsworth, W. L., M. Celebi, J. R. Evans, E. G. Jensen, R. Kayen, M. C. Metz, J. D. Nyman, J. W. Roddick, P. Spudich, and C. D. Stevens, (2004), Near-field ground motion of the 2002 Denali Fault, Alaska, earthquake recorded at pump station 10, *Earthquake Spectra*, *20*(3), 597-615.

## BIBLIOGRAPHY

- [129] Chester, J. S., F. M. Chester, and A. K. Kronenberg (2005), Fracture surface energy of the Punchbowl fault, San Andreas system, *Nature*, *437*, 133-136, doi:10.1038/nature03942.
- [130] Tordesillas, A., J. F. Peters, and B. S. Gardiner (2004), Shear band evolution and accumulated microstructural development in Cosserat media, *Int. J. Numer. Anal. Methods Geomech.*, *28*, 981-1010, doi:10.1002/nag.343.
- [131] Carpenter, B. M., C. J. Marone, and D. M. Saffer (2007), Frictional behavior of materials in the 3D SAFOD volume, *Eos Trans. AGU*, *88*(52), Fall Meet. Suppl., Abstract T41B-0580.
- [132] Di Toro, G., T. Hirose, S. Nielsen, G. Pennacchioni, and T. Shimamoto (2006), Natural and experimental evidence of melt lubrication of faults during earthquakes, *Science*, *311*, 647-649.
- [133] Favreau, P., I.R. Ionescu, and M. Campillo (1999), On dynamic sliding with rate- and state-dependent friction laws, *Geophys. J. Int.*, *139*(3), 671-678, doi:10.1046/j.1365-246x.1999.00970.x.
- [134] Beresnev, I. A. (2003), Uncertainties in finite-fault slip inversions: To what extent to believe? (A critical review), *Bull. Seismol. Soc. Am.*, *93*(6), 2445-2458, doi:10.1785/0120020225.
- [135] Kanamori, H., and D. L. Anderson (1975), Theoretical basis of some empirical relations in seismology, *Bull. Seismol. Soc. Am.*, *65*, 1073-1096.
- [136] Scholz, C. H. (1982), Scaling laws for large earthquakes: consequences for physical models, *Bull. Seismol. Soc. Am.*, *72*(1), 1-14.
- [137] King, G. C. P., and S. G. Wesnousky (2007), Scaling of fault parameters for continental strike-slip earthquakes, *Bull. Seismol. Soc. Am.*, *97*(6), 1833-1840, doi:10.1785/0120070048.
- [138] Hillers, G., and S. G. Wesnousky (2008), Scaling relations of strike-slip earthquakes with different slip-rate-dependent properties at depth, *Bull. Seismol. Soc. Am.*, *98*(3), 1085-1101, doi:10.1785/0120070200.
- [139] Shaw, B. E., and S. G. Wesnousky (2008), Slip-length scaling in large earthquakes: The role of deep-penetrating slip below the seismogenic layer, *Bull. Seismol. Soc. Am.*, *98*(4), 1633-1641, doi:10.1075/0120070191.